Active Control of Propeller Aircraft Run-up Noise

by

Ann Marie Nakashima

B.Sc.(Hons. Physics), The University of British Columbia, 2001

A THESIS SUBMITTED IN PARTIAL FULFILMENT OF
THE REQUIREMENTS FOR THE DEGREE OF

MASTER OF APPLIED SCIENCE

in

The Faculty of Graduate Studies

(Department of Mechanical Engineering)

We accept this thesis as conforming
to the required standard

THE UNIVERSITY OF BRITISH COLUMBIA

November 27, 2003

Library Authorization

In presenting this thesis in partial fulfillment of the requirements for an advanced degree at the University of British Columbia, I agree that the Library shall make it freely available for reference and study. I further agree that permission for extensive copying of this thesis for scholarly purposes may be granted by the head of my department or by his or her representatives. It is understood that copying or publication of this thesis for financial gain shall not be allowed without my written permission.

Ann Nakashima — Name of Author *(please print)*

Dec 19, 2003 — Date

Title of Thesis: Active Control of Propeller Aircraft Run-up Noise

Degree: M.A.Sc. Year: 2003

Abstract

In 2000, the first phase of research on the feasibility of using active noise control (ANC) to control the noise from propeller aircraft run-up tests was completed by Germain. ANC is a noise cancellation technique that has been the focus of much research in recent years. It was of interest to extend the work by Germain, concentrating on the effects that phenomena such as atmospheric refraction and the ground impedance have on the performance of an ANC system. Furthermore, since propeller aircraft were found to have directional noise radiation, the studies must consider the effectiveness of an ANC system on complex noise sources.

The effectiveness of an ANC system on a dipole noise source was investigated in a free-field environment through simulations and experiments. It was found that the performance of an ANC system depends on the orientation of the dipole noise source, and that the system is most effective when used to control noise in the direction of the strongest radiation of the source. Measurements of run-up noise from a Dash-8 were taken and analyzed to gain a better understanding of how it acts as a noise source. It was found that the full-power engine noise is strongly tonal, making it a possible candidate for ANC. The noise was also found to be strongly directional.

The Green's function parabolic equation (GFPE) method for outdoor sound propagation was modified to include a single active control channel, and ANC predictions were performed in the case of reflective and soft grounds for different atmospheric conditions. The preliminary results show that atmospheric refraction causes fluctuations in the noise attenuation achieved by a single-channel control system, and has the overall effect of decreasing its performance. It is evident that

multiple control channels must be used in order to achieve significant attenuation for realistic outdoor conditions. Further research is required to determine if multi-channel ANC is a realistic method for the control of propeller aircraft run-up noise in realistic situations.

Contents

List of Tables

List of Figures

Acknowledgements

This work would not have been possible without the enormous amount of support that I have received from colleagues, family and friends. I have been blessed to have been surrounded by exceptional people my entire life.

First on my list is Professor Murray Hodgson, who has supervised me since my final year of undergraduate studies. Murray took a chance on me and agreed to supervise me at a time when I did not have confidence in myself as a researcher. His knowledge and experience in acoustics is invaluable, and I have learned much under his guidance. That coupled with the fact that we share a fondness of coffee and sushi (though perhaps not at the same time), we have maintained an amiable bond over the past few years.

A word of gratitude goes to the Vancouver International Airport Authority (VAA) and NSERC for funding support. Mark Cheng and Fred Tewfik of the VAA have provided excellent support over the past two years. They were also fundamental in the organization of the Dash-8 measurements. Thank you to Air Canada Jazz for providing the aircraft for the measurements. Thank you also to my Dash-8 measurement crew members: Desheng Li, Galen Wong, Isaac Leung, Robert Ma and Murray Hodgson. I hope those chocolate bars made up for dragging you out to the airport on a Saturday night! Thanks also to Perry Wong for helping with the dipole source.

Through Murray's connections, I was fortunate to be in contact with a number of world experts on ANC and outdoor sound propagation. Thank you to Dr. Jingnan Guo for sharing his expertise on ANC. Thank you to Dr. Xiao Di for providing the GFPE code. Thank you to Dr. Mike Stinson, Dr. Keith Attenborough and

Dr. Sharam Taherzadeh for their advice on using the GFPE and FFP models.

Thank you to the National Association of Japanese Canadians (NAJC) for the endowment fund grant that allowed me to travel to Korea to attend the Inter-Noise 2003 conference.

Mom and Dad, I'm sorry that I have been in school so long. But thank you for your patience in supporting me throughout my university career, and throughout my whole life. I promise that I'll go out and find a job now! I love you.

Although he will probably never read this, I have to thank my junior high school English teacher, Bill Taylor, who would be horrified to know that I am an engineer now. Thank you for giving me confidence in my writing skills. It sure helped a lot in writing this thesis!

To Galen Wong, my best acoustics buddy, thank you for putting up with all of my tantrums over the past year. I could not have survived without all of the Starbucks runs and "Scrabble nights." And don't worry, I will return the favour when you go through this next year!

Ann Nakashima, November 2003.

Chapter 1

Introduction

1.1 Airport Noise

Airport noise is a constant source of annoyance to people residing in nearby communities. The operations pertaining to the most complaints from the community are aircraft take-offs, landings, fly-overs, and engine run-ups. Airport management controls in-flight noise as much as possible by directing flight paths away from communities and limiting the number of night-time flights. Further in-flight noise attenuation can normally only be achieved by improving the acoustical design of the aircraft. However, today it is possible for airports to consider novel methods such as active noise control to control aircraft run-up noise, because the aircraft are stationary. Engine run-ups are part of normal aircraft maintenance, and are usually performed at night as the aircraft are in use during the day. Run-ups involve running the engines at idle, above idle, and full-power settings in order to ensure proper operation. The noise that is radiated into adjacent communities is mainly low-frequency noise caused by the blade-passing frequency (BPF), which is typically about 100Hz, and its harmonics.

The Vancouver International Airport (YVR) is one of the largest airports in Canada, and is the premier gateway between Asia-Pacific and North America. Airport noise issues are addressed by the Vancouver International Airport Authority (Airport Authority), and summarized annually in noise management publications. One of the noise management plan initiatives is aimed at engine run-ups. Initially, work on this initiative was focused on investigating the feasibility of building a ground run-up enclosure (GRE). However, several operational and noise issues

were identified, and it was decided that other solutions would be investigated [1]. One possible solution that was identified was active noise control, which involves the use of destructive interference of sound waves to cancel the radiated acoustic power.

In 2000, the first phase of research on investigating the use of an active noise control (ANC) system at the run-up site was completed [2]. While this research produced some interesting results, they were limited by 1). oversimplification of the noise source, and 2). the lack of consideration of realistic meteorological and ground conditions in the computer simulations done to evaluate and optimize active control systems. Propeller aircraft are complex noise sources that cannot be adequately represented by omnidirectional monopoles. Noise source directivities will be discussed in the next section. Furthermore, in an outdoor environment, factors such as wind-speed and temperature gradients, ground composition, irregular terrain and turbulence affect the propagation of sound waves. In particular, the atmospheric conditions and ground surface will change the amplitude and phase of the sound waves arriving at a receiver position along various propagation paths. Since active noise control requires that the system produces a signal that has the same amplitude and opposite phase as the noise signal, it is essential to account for the environmental conditions in the design of the control system. For these reasons, a second stage of research that would address these issues was proposed. This thesis, which was funded by the Airport Authority and the Natural Sciences and Engineering Research Council (NSERC), is the result of that research.

A literature review of ANC and outdoor sound propagation was performed in order to gain a better understanding of the issues mentioned above. This information is required in order to consider how outdoor environmental conditions would affect the performance of an active control system on propeller aircraft run-up noise.

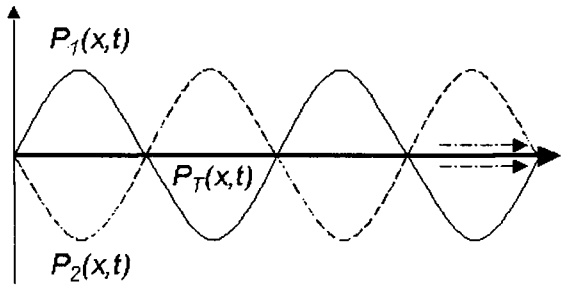

Figure 1.1: Young's Principle of interference.

1.2 Active Noise Control

The basic principle of superposition states that when two or more waves are traveling in the same medium, the net displacement of the medium at any point is the sum of all the displacements caused by the individual waves. If the waves are in phase, the displacements that they cause will add constructively, resulting in maximal medium displacement. Conversely, if the waves are exactly opposite in phase, the displacements will add destructively, resulting in zero medium displacement (no wave), as shown in Fig. 1.1. This principle of destructive interference, known as Young's Principle, is the fundamental idea behind active noise control.

Active control of sound and vibration has been in use since the 1930s. However, until the emergence of powerful, low-cost digital signal processor (DSP) chips in the 1980s, ANC was considered to have limitations in its use due to its lack of stability and high cost [3]. Now that the required technology is available, ANC has evolved from simple analog filters to adaptive digital multiple-input, multiple-output (MIMO) systems.

There are two basic structures that ANC systems are based on: feedback and feedforward. In a feedback setup, a high-gain negative feedback loop is used to produce zero acoustic pressure at the microphone; detection and attenuation oc-

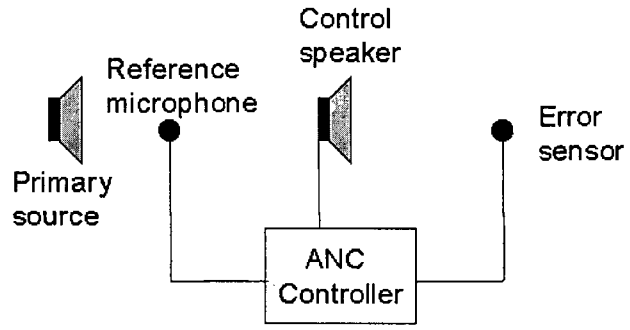

Figure 1.2: Basic setup of a feedforward ANC system.

cur in the same region [3, 4]. The disadvantage of this arrangement is that the secondary source must be placed close to the microphone for the system to be stable; this may be undesirable in some applications [3]. The basic setup of a feedforward ANC system is shown in Fig. 1.2. A reference sensor (microphone) detects the signal from the noise source (primary source). The signal is passed on to the ANC controller, which sends a signal of appropriate amplitude and phase to the control speaker (secondary source) such that a minimum signal is detected at the microphone (error sensor). The combined signal is detected at the microphone (error sensor). The error signal is fed back to the ANC controller, which works to minimize the error signal. An area of sound reduction is thus produced around the error microphones. Since it is not necessary to place the error sensor close to the secondary speakers, feedforward control is generally more stable than feedback control; however, it relies on having a good reference signal.

There are two major strategies of ANC: global and local control. The global control strategy aims to attenuate the total sound power of the noise source, resulting in noise attenuation everywhere. It is possible to have global control if the control sources can be placed within a half-wavelength from the primary source in the case of a monopole [5]. Thus, the feasibility of using global control is limited by the frequency of interest and the range of distances from the primary source at

which the control sources can be placed. In many cases, it is not possible to achieve global control, so the local control strategy is used. Local control reduces noise in desired areas by creating a quiet zone. The size of the quiet zone in a given environment depends on the relative positions of the primary source, secondary sources and error microphones, and the number of control channels used.

The global control strategy is not feasible in the case of propeller aircraft noise because it is not possible to place the speakers close to the engines. However, it should be possible to use local control to create quiet zones in the direction of the residential areas neighbouring the airport.

1.3 Noise Source Directivity

Noise sources can be represented in an way analogous to electrical charges in physics. Like a point charge, a point sound source is a monopole that radiates energy equally in all directions. Such a source is said to be omnidirectional, and radiates spherical wavefronts. The radiation of some real noise sources can be approximated as monopoles at low frequency. However, other noise sources are strongly directional. In particular, rotating noise sources such as propellers or fans may have a directivity that is monopole, dipole, quadrupole or a combination of the three [2]. The directivities of monopole, dipole and quadrupole sources are shown in Fig. 1.3.

For directional noise sources, the performance of an ANC system will depend on the orientation of the source relative to the control system. It is thus essential to understand how the noise source radiates sound before active control techniques are applied.

1.4 Sound Propagation Outdoors

In a homogeneous, stationary atmosphere there are no temperature gradients and the wind speed is constant throughout. In such an atmosphere, propagating

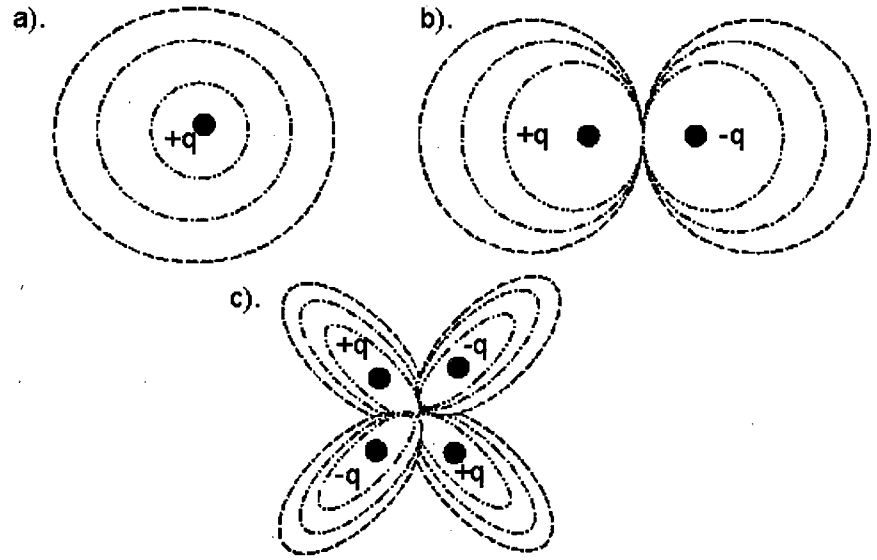

Figure 1.3: Directivity of a a). monopole b). dipole and c). quadrupole noise source.

sound waves are not refracted and the sound speed is adiabatic, and a function of the atmospheric temperature. These conditions were assumed in the first phase of this research. In reality, when studying outdoor noise problems, complications arise due to refraction of sound waves by wind and/or temperature gradients, due to absorption by the atmosphere, and fluctuations in phase and amplitude due to turbulence. In addition, different types of ground and terrain will influence the reflected sound path in different ways, giving rise to complex interference patterns that affect the amplitude and phase of the sound waves arriving at the receiver. This section gives an overview of the physics of these phenomena.

1.4.1 The Basic Problem

As an introduction to sound propagation outdoors, consider a single source and receiver in the presence of a single flat, smooth surface, which represents the ground. Sound waves arrive at the receiver by two propagation paths: the direct path and the reflected path. These paths are labelled in Fig. 1.4 by the associated

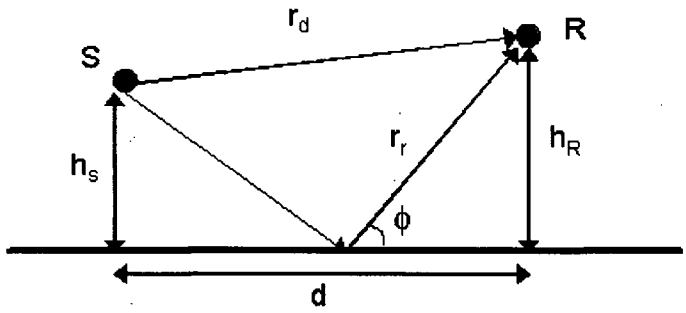

Figure 1.4: Direct and reflected waves from a source to a receiver.

source and receiver distances, r_d and r_r, respectively [6]. The sound field at the receiver is comprised of the contributions from the two sound paths. Except in the case when the source is on the ground (such that $r_d = r_r$), destructive interference minima will occur at frequencies for which the path-length difference $(r_r - r_d)$ is $\frac{\lambda}{2}$. This corresponds to a phase difference of 180° between the two propagation paths.

For smooth ground, and assuming that the horizontal distance between the source and receiver is large compared to their elevations (so that wave sphericity can be ignored), it is easy to calculate the sound pressure level at the receiver. In this case, the waves can be assumed to be planar. The sound reflecting from the ground is described by the planar reflection coefficient, R_p, given by

$$R_p = \frac{\sin\phi - \frac{Z_1}{Z_2}}{\sin\phi + \frac{Z_1}{Z_2}} \tag{1.1}$$

where ϕ is the angle of incidence (measured from the ground), and Z_1 and Z_2 are the impedances of the air and ground, respectively [6]. Fig. 1.5 shows the measured sound pressure levels for various source heights over asphalt, an acoustically hard surface. Note that if the ground is of infinite impedance, $R_p \rightarrow 1$ and the sound waves do not suffer any attenuation on reflection. Also, if the ground impedance Z_2 is complex, there will be a phase change on reflection.

This solution is simple, but not realistic. If one wishes to predict the sound field

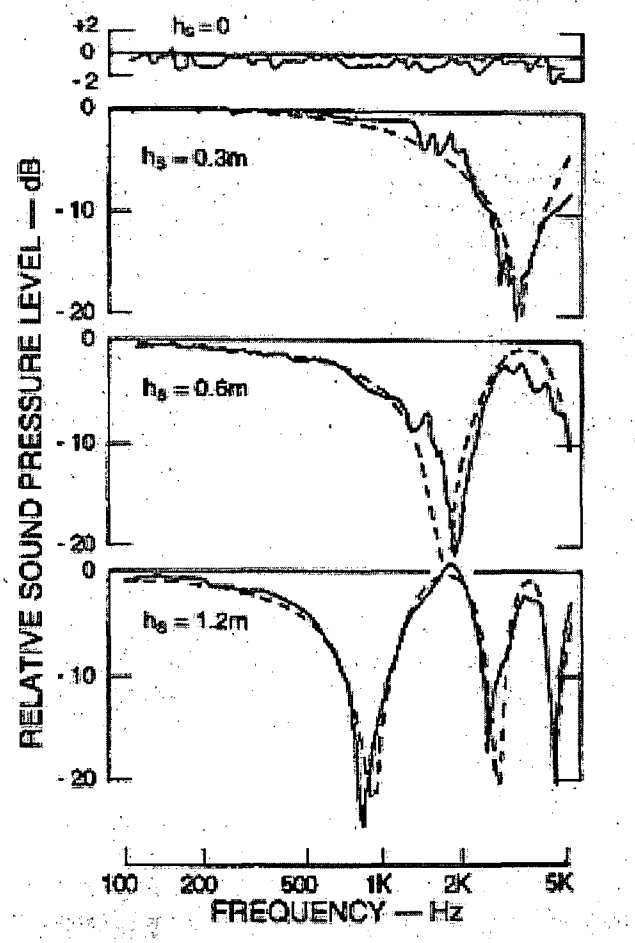

Figure 1.5: Measured relative sound pressure levels from a point source for $d = 15.2$ m and $h_R = 1.2$ m (solid lines) above an asphalt surface for different source heights, h_s. The dashed lines are predictions for a surface of infinite impedance [7].

at a receiver point for low frequencies, or for short source-to-receiver distances, the plane-wave assumption is no longer correct, and the equation for the spherical-wave reflection coefficient must be used in lieu of Eq. 1.1. The spherical-wave reflection coefficient includes the contribution of the ground wave, which will be discussed in Section 1.4.3. Atmospheric effects, rough ground or uneven terrain, and turbulence, further complicate the problem. These issues will be discussed in the following sections.

1.4.2 Atmospheric Effects

Molecular Absorption

As sound waves propagate in the atmosphere, some of the sound energy is absorbed and converted into vibrational energy of the oxygen and nitrogen molecules [7]. The amount of energy that is absorbed depends on the temperature, humidity, and frequency. Table 1.1 lists the attenuation by octave band for various relative-humidity (RH) and temperature conditions. It is apparent that atmospheric absorption is relatively insignificant at low frequencies, which explains why the noise problem due to aircraft engine run-ups exists for low frequencies only. The low-frequency sound absorption is also little affected by humidity and temperature.

Temperature Gradients

One of the principal meteorological variables is the vertical temperature gradient. A temperature inversion describes the condition when the temperature increases with height above the ground (positive gradient) and a temperature lapse is when the temperature decreases with height (negative gradient). Temperature inversions generally occur at night. In the daytime, there is usually a temperature lapse, because the ground is heated by solar radiation [7].

During a temperature lapse, the sound waves emitted from the source are re-

Table 1.1: Attenuation due to atmospheric absorption in dB/1000 m, given by relative humidity (RH), temperature, and octave band [8].

RH(%)	T(°C)	63Hz	125Hz	250Hz	500Hz	1kHz	2kHz	4kHz	8kHz
25	15	0.2	0.6	1.3	2.4	5.9	19.3	66.9	198.0
	20	0.2	0.6	1.5	2.6	5.4	15.5	53.7	180.5
	25	0.2	0.6	1.6	3.1	5.6	13.5	43.6	153.4
	30	0.1	0.5	1.7	3.7	6.5	13.0	37.0	128.2
50	15	0.1	0.4	1.2	2.4	4.3	10.3	33.2	118.4
	20	0.1	0.4	1.2	2.8	5.0	10.0	28.1	97.4
	25	0.1	0.3	1.2	3.2	6.2	10.8	25.6	82.2
	30	0.1	0.3	1.1	3.4	7.4	12.8	25.4	72.4
75	15	0.1	0.3	1.0	2.4	4.5	8.7	23.7	81.6
	20	0.1	0.3	0,9	2,7	5,5	9,6	22.0	69.1
	25	0.1	0.2	0.9	2.8	6.5	11.5	22.4	61.5
	30	0.1	0.2	0.8	2.7	7.4	14.2	24.0	58.4

fracted upwards. Since the temperature decreases with height, and the sound speed increases proportionally with temperature, the sound waves bend towards the normal centered on the source as shown in Fig. 1.6a. This is analogous to Snell's Law in optics, which dictates that when light enters a medium of a lower refractive index, it will bend towards the normal. As a result, there is an area of low sound pressure level near the ground surrounding the source, called the shadow region [7].

During a temperature inversion, sound waves radiating upward from the source will be refracted downwards toward the ground, as pictured in Fig. 1.6b. This results in increased sound levels near the ground [7]. Since engine run-ups are performed at night when a temperature inversion exists, this suggests that the noise levels heard by neighbouring communities are louder than those produced by daytime run-ups.

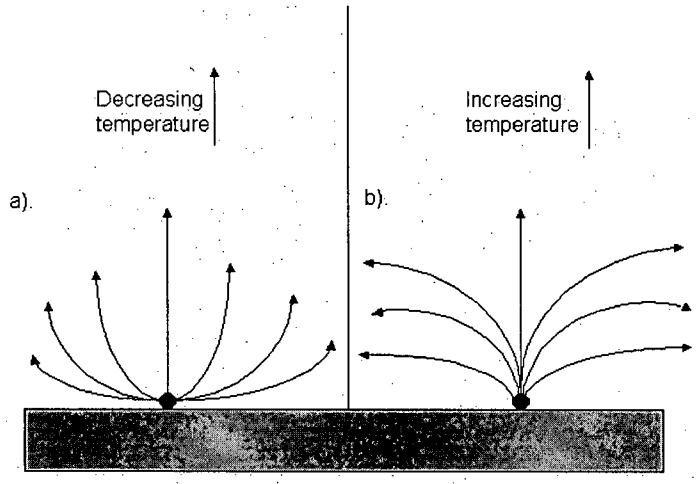

Figure 1.6: Refraction of sound in air due to a). temperature lapse and b). temperature inversion [7].

Wind-Speed Gradients

Vertical wind-speed gradients also cause the sound waves to be refracted. Normally, the wind speed increases with altitude. During a temperature inversion, this increase tends to be more rapid than during a temperature lapse [7]. Sound that propagates against the wind, or upwind, is refracted downwards, resulting in a shadow region, as shown on the right side of Fig. 1.7 [8]. Sound that propagates with the wind, or downwind, is refracted downwards, producing increased sound levels near the ground. The refraction pattern is asymmetric about the center of the source, unlike in the case of temperature gradients, where the refraction pattern is symmetric.

1.4.3 Ground Effects

To extend the outdoor sound propagation theory to more realistic conditions, one must consider real ground surfaces. The analysis in Section 1.4.1 assumed a smooth, flat ground surface. This section describes different types of ground, and

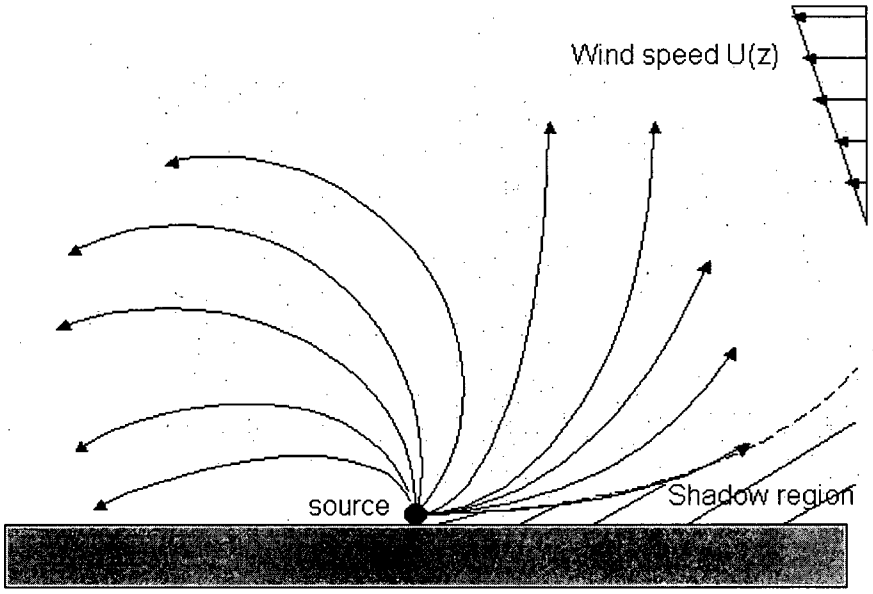

Figure 1.7: Refraction of sound in air with wind speed increasing with altitude [8].

what happens when the plane wave assumption is invalid.

Types of Ground

Ground surfaces can be classified loosely into four categories, based on their acoustical properties for sound-wave reflection angles of less than 20% [9]:

- Hard: low porosity surfaces such as asphalt or concrete pavement, water;
- Soft: ground covered by grass, trees, or other vegetation, farming land;
- Very soft: highly porous surfaces, such as ground covered with snow, pine needles, or other loose material;
- Mixed: ground with both hard and soft areas;

As mentioned in Section 1.2.1, sound waves reflecting from ground of infinite impedance will suffer no attenuation upon contact with the surface. Thus, hard ground such as non-porous concrete will absorb very little of the sound energy. Soft and very soft grounds will absorb some sound energy. Absorption implies a complex reflection coefficient. The reflected part of the sound field suffers a phase upon reflection from the absorptive ground. As an example of the effect of soft

Table 1.2: Characterization of various ground surfaces over the frequency range 300 Hz to 30 kHz. The values of effective flow resistivity were obtained by matching transmission spectra measured in situ with spectra predicted theoretically (cited in [7]).

Description of Surface	Effective Flow Resistivity (kPa s/m^2)
0.1 m new fallen snow, over older snow	10-30
Sugar snow	25-50
Floor of evergreen forest	20-80
Airport grass or old pasture	150-300
Roadside dirt, ill-defined, small rocks up to 0.01 m mesh	300-800
Sandy silt, hard packed by vehicles	800-2500
Thick layer of clean limestone chips, 0.01-0.025 m mesh	1500-4000
Old dirt roadway, small stones with interstices filled by dust	2000-4000
Earth, exposed and rain-packed	4000-8000
Very fine quarry dust, hard packed by vehicles	5000-20 000
Asphalt, sealed by dust and use	~30 000
Upper limit, set by thermal conduction and viscosity	2×10^5 to 1×10^6

ground, consider the apparent quietness of the outdoors when there is a blanket of snow on the ground. Snow-covered ground is a very soft surface that absorbs more sound energy than a grassy or concrete surface, resulting in a quieter environment.

Delany and Bazley first developed a theory for calculating the flow resistivity of surfaces from measurements of interference between direct and ground-reflected sound fields [7]. Attenborough later combined this property with porosity, tortuosity, steady-flow shape factor and dynamic shape factor to more accurate describe ground surfaces [7]. The most important of these properties are flow resistivity and porosity, which are now described by the single term "effective flow resistivity." This term allows surfaces to be classified much more specifically than the general categories listed above; for example, differences between loose dirt and hard packed dirt can be made. Table 1.2 lists effective flow resistivities for various surfaces [7].

Wave Propagation Near the Ground

Ground surfaces with complex impedances give rise to reflected sound waves that travel nearly horizontally close to the surface. The sound field near the ground is composed of three components [7]:

- Creeping wave: a wave that conducts sound energy close to the ground along the minimum-time path between the source and the receiver. Creeping waves occur when the atmosphere causes upward refraction of sound waves. They are the waves that comprise the attenuated sound field in the shadow zone. As the wave propagates, energy is radiated away from the surface in the sound field above the ground;
- Ground wave: the part of the reflected field that is not accounted for by the plane wave reflection coefficient (Eq. 1.1). Ground waves occur when the sound field spreads spherically from the source, resulting in waves that hit the ground with different angles of incidence. The reflection coefficient thus varies with horizontal position along the ground;
- Surface wave: a concentration of sound energy above the surface. Surface waves occur when the imaginary part of the ground impedance exceeds the real part. These waves are trapped along the surface, resulting in a waveguide that forces two-dimensional propagation and losses due to the ground resistance.

Ground waves occur whenever the incident waves are not planar. As an example, consider Fig. 1.8, which shows the relative sound pressure levels measured 5m away from a point source on a grassy surface for various receiver heights [7]. For a source close to the ground, $\sin\phi \to 0$. From Eq. 1.1, it can be seen that $R_p \to -1$. This suggests that there should be lower sound levels at all frequencies, but Fig. 1.8 shows a loss only at high frequencies. This proves the existence of a part of the sound field that is not accounted for by the plane-wave reflection coefficient; it is an illustration of the ground-wave contribution. Since the ground wave appears to have a strong effect at low frequencies, it is important that it be included in a

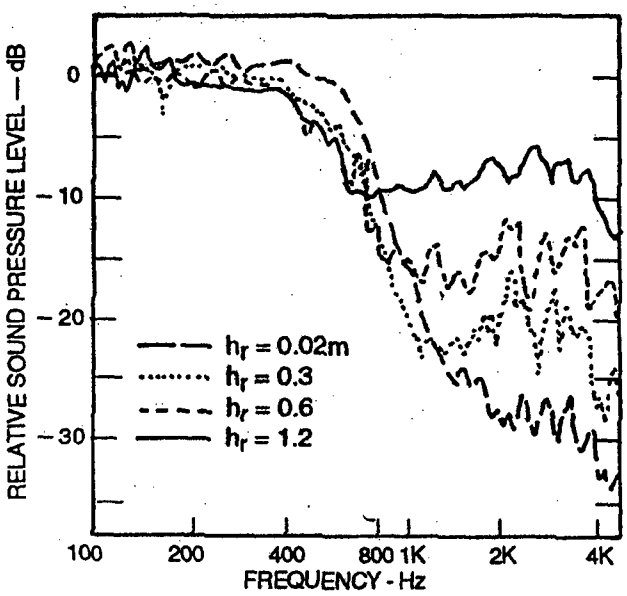

Figure 1.8: Relative sound pressure levels measured 5m from a point source located in the plane of a grass-covered surface [7].

prediction model for run-up noise.

Turbulence

Atmospheric turbulence always exists, even when there are no strong wind or temperature gradients. In the context of this research, there will also be turbulence due to the rotation of the aircraft propeller. To implement active noise control, it is essential that the ANC system produce a signal that is equal in amplitude and opposite in phase to the noise signal. Since turbulence causes random fluctuations in the amplitude and phase of the direct and reflected sound waves, it is a factor that can greatly affect the noise cancellation achieved by the ANC system.

Turbulence is known to cause near-instantaneous changes in temperature and wind speed. Through the use of thermocouples and anemometers, acousticians have measured these changes. It has been found that the temperature may fluctuate by 5°C within seconds [7]. Daigle *et al.* (cited in [7]) determined that the disturbance in the amplitude and phase of the sound field caused by turbulence is

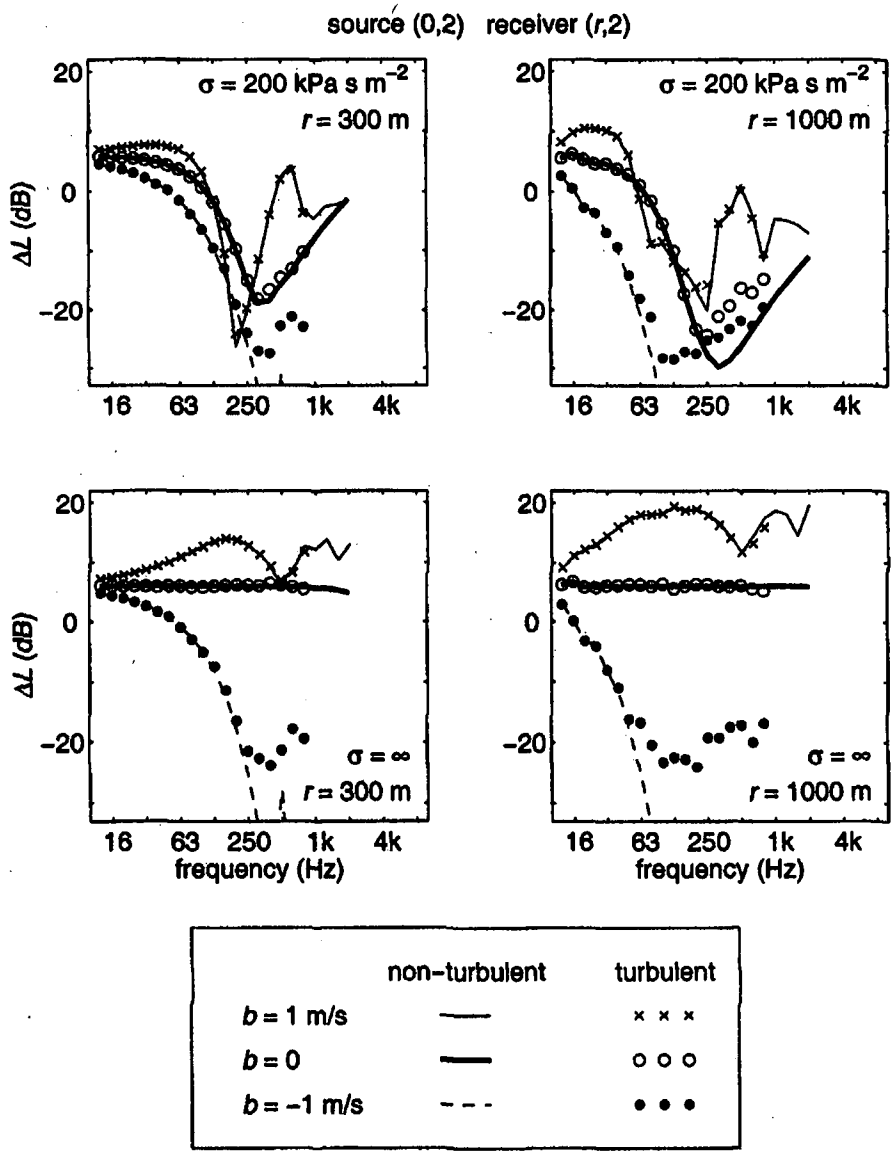

Figure 1.9: One-third octave band spectra of relative sound pressure levels for various source-receiver distances r calculated with the Crank-Nicholson Parabolic Equation method. The parameter b is 1 for a downwardly refracting atmosphere, 0 for a non-refracting atmosphere and -1 for an upwardly refracting atmosphere [10].

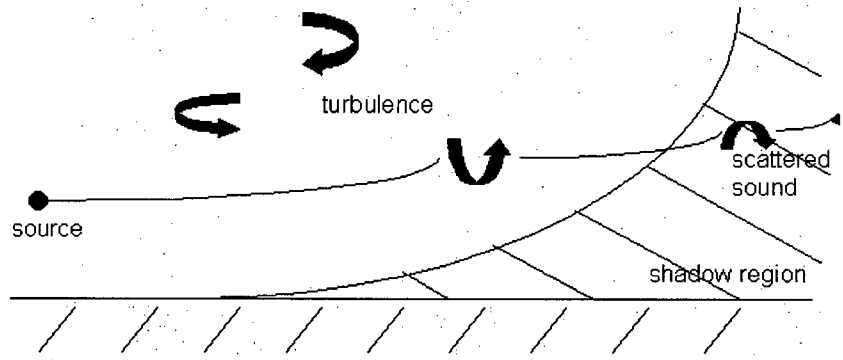

Figure 1.10: Scattering of sound into a refractive shadow region [10].

frequency dependent, and increases with distance from the source. They predicted that the sound amplitude increases as $d^{\frac{11}{12}}$ up to 6 dB, and $f^{\frac{7}{12}}$, where d is the distance and f is the frequency. The phase fluctuations were predicted to increase linearly with distance. Fig. 1.9 shows the relative sound pressure levels for various source-receiver distances as predicted by the Crank-Nicholson Parabolic Equation method, which is discussed in Chapter 5. It appears that turbulence causes an increase in sound pressure levels at 100Hz as the distance increases. This suggests that turbulence by itself may actually help to lower the sound pressure levels heard at communities neighbouring the airport, and that accurate prediction of turbulence may not be a priority in this application. However, it is still a factor that causes fluctuations in the sound field, and should best be taken into account in some way, if not to high accuracy.

In a non-refracting atmosphere, there are interference minima in the sound field due to destructive interference between the direct and reflected sound waves. Addition of turbulence causes fluctuations in the sound speed in the atmosphere. This affects the amplitude and phase of the sound waves, and the fluctuations in phase cause reductions in the depth of the interference minima. A similar effect occurs in a downwardly refracting atmosphere. In an upwardly refracting atmo-

sphere, there is a shadow region where the sound pressure level is low, as mentioned in Section 1.2.2. The relative sound pressure levels in this region can be more than 30dB lower than outside the shadow zone. Atmospheric turbulence causes the levels in the shadow region to increase by about 10dB, due to scattering by turbulent inhomogeneities in the atmosphere (see Fig. 1.10) [10]. The random changes in propagation direction cause sound energy to be scattered into the shadow region.

1.5 Summary

It has been shown in this chapter that describing outdoor sound propagation with high accuracy is a difficult problem, particularly at low frequencies. The noise problem caused by engine run-up tests is largely due to the fact that low frequencies are scarcely absorbed by the atmosphere, causing them to radiate strongly into neighbouring communities and disturbing the residents. In addition, the tests are usually run at night-time, when temperature inversions normally occur. This condition leads to downward refraction of sound waves, resulting in increased sound levels near the ground. Clearly, atmospheric and ground effects must be accounted for when considering the use of ANC for engine run-up noise.

1.6 Outline of Thesis

The theory of ANC will be discussed in Chapter 2. The limitations of global control will be discussed briefly. Equations for single- and multiple-channel local control in the free-field and in a half-space will be shown.

In Chapter 3, the creation of a noise source with dipole directivity will be described. The results of 3-channel ANC experiments on the dipole source, performed in an anechoic chamber, will be shown and compared to simulation results. The effectiveness of the ANC system for different orientations of the dipole will be

discussed.

Measurements of run-up noise from a Dash-8 aircraft, performed at the Vancouver International Airport in August 2002, will be discussed in Chapter 4. The analysis of the narrow-band and 1/3 octave band spectra for three different engine power settings will be presented. Directivity patterns will be shown for each of the engine power settings. Estimates of the noise levels in the far field using the Dash-8 data and the Beechcraft 1900D data measured by Germain [2] will be shown, as well as estimates of the Dash-8 noise radiation from a single propeller. Active noise control strategies based on the Dash-8 measurement results will be discussed.

In Chapter 5, prediction models for outdoor sound are discussed. A overview of four different prediction models is presented. The models are evaluated qualitatively in terms of accuracy and the complexity of the phenomena that can be modeled.

In Chapter 6, validation work of the Green's function parabolic equation (GFPE) model for outdoor sound propagation will be shown for four benchmark cases. A modified GFPE program that includes a single control channel will be validated by comparing the results with a theoretical ANC model for the case of a half-space. Single-channel control results using the modified GFPE program will be shown for various outdoor conditions, including the effects of temperature gradients, wind-speed gradients and finite-impedance ground. Finally, the limitations of using the GFPE for ANC predictions will be discussed.

Conclusions of this research and recommendations for future work will be discussed in Chapter 7.

Chapter 2

Active Noise Control Theory

2.1 Introduction

As discussed in Chapter 1, the best method of active noise control involves 'global' control, which reduces noise everywhere. In most practical cases, it is not possible to achieve global control. The limitations of the use of global control for propeller aircraft noise are discussed briefly in this chapter. A local control system generally creates quiet zones at the cost of increasing the total sound-power output. Thus, the total power-output increase is used as the cost function (function to be minimized) for local control. Another measure of the effectiveness of a local control system is the size of the quiet zone that it creates. Equations for the total power-output increase will be derived for the free-field case and the half-space case. In the free-field case, no reflective surfaces are present or, equivalently, all of the surfaces are completely absorptive. In the half-space case, the control system is assumed to be placed above a totally reflective surface.

Most studies of ANC have concentrated on reducing the primary field generated by a monopole sound source. Although the directivity of many practical noise sources is approximately monopole at low frequencies, more complex noise sources, such as aircraft propellers, are better represented by multipole sources (e.g. dipole, quadrupole, etc.). For example, it has been shown that the noise radiated by a fan at low frequencies can be represented by a dipole [11]. Unlike the sound field produced by a monopole source, multipole sound fields are orientation dependent and do not display cylindrical symmetry [12]. It is thus of interest to investigate the effectiveness of an active control system on multipole sources. Active control of directional sources will be introduced briefly in this chapter.

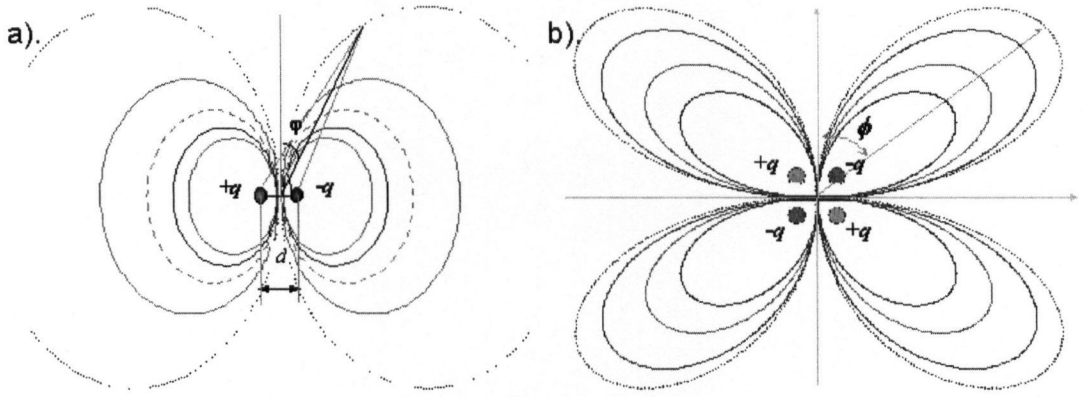

Figure 2.1: Radiation patterns of a). a dipole source and b). a quadrupole source [13].

2.2 Limitations of Global Control

It is often not possible to achieve global control (noise attenuation in all areas) because the control sources cannot be placed very close to the primary source. In the case of propeller aircraft noise, it is not possible to place the control speakers very close to the engines for safety reasons. Furthermore, Germain showed that the noise directivity of the Beechcraft 1900D is directional, although no clear dipole or quadrupole pattern was identified [2]. For directional primary sources, the performance of the control system will depend on the orientation of the primary source with respect to the position of the control system. The orientation of dipole and quadrupole sources is defined by the placement of the control system with respect to the y-axis, as shown in Fig. 2.1. For example, when a dipole source is oriented at 90° or 270°, the control system is placed in the direction of the maximum radiation of the source. The global control efficiency of a single-channel control system is shown in Fig 2.2 for monopole, dipole and quadrupole primary

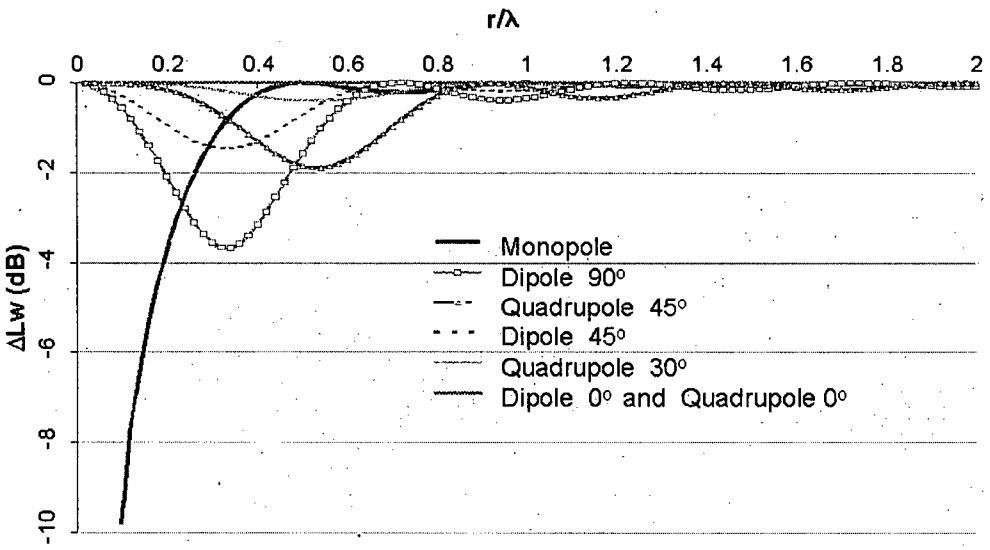

Figure 2.2: Global noise reduction as a function of the separation between the control and primary sources [13].

sources [13]. In the case of a monopole primary source, the control source must be placed within 0.5λ of the primary source. With the control source placed very close to the primary source, more than 10dB of attenuation can be achieved. For a dipole source oriented at 90°, a maximum of 4dB of attenuation can be achieved by a single control channel, while for a quadrupole source oriented at 45° the maximum attenuation is only 2dB.

Even if it was possible to place the control speakers close to the aircraft engines, little noise attenuation can be achieved for dipole and quadrupole noise sources using the global control strategy. Since it is desirable to achieve a large amount of noise attenuation in (localized) noise-sensitive areas near the airport (residential communities), the local control strategy is a feasible option, and will be studied in this chapter.

2.3 Free-field Local Active Control

2.3.1 Single-source, Single-channel Control

A single-channel local ANC system setup in the free field is shown in Fig. 2.3. The system has a single secondary source of strength q_s, placed a distance r_{ps} away from the primary source, which has strength q_p. The error sensor is placed a distance r_{pe} away from the primary source, and a distance r_{se} away from the secondary source. Since the system is arranged in a line, $r_{pe} = r_{ps} + r_{se}$. It has been shown that this linear arrangement provides optimal noise attenuation, as opposed to a triangular arrangement in which the error sensor is placed at an angle to the primary-secondary source line [14]. The sound power outputs of the primary and secondary sources are, respectively [14]

$$W_p = \frac{1}{2}Z_o|q_p|^2 + \frac{1}{2}\mathrm{Re}\left(q_p Z_{ps}^* q_s^*\right), \tag{2.1}$$

$$W_s = \frac{1}{2}Z_o|q_s|^2 + \frac{1}{2}\mathrm{Re}\left(q_s Z_{sp}^* q_p^*\right), \tag{2.2}$$

and the total power of the system is

$$W_T = W_p + W_s = \frac{1}{2}Z_o\left(|q_p|^2 + |q_s|^2\right) + \frac{1}{2}\mathrm{Re}\left(q_p Z_{ps}^* q_s^* + q_s Z_{sp}^* q_p^*\right), \tag{2.3}$$

where $Z_o = \omega^2\rho_o/4\pi c_o$ is the characteristic impedance of air, $Z_{ps} = Z_{sp} = Z_o\left[\sin kr_{ps}/kr_{ps} + i\cos kr_{ps}/kr_{ps}\right]$ is the acoustic transfer impedance between the primary and the secondary source, and $k = 2\pi/\lambda$ is the wavenumber.

Since the minimum total sound power output is desired, the cost function is the total power output of the system, W_T. The strength of the control source that is required to minimize the cost function is [14]

$$q_s = -q_p \mathrm{sinc} kr_{ps}, \tag{2.4}$$

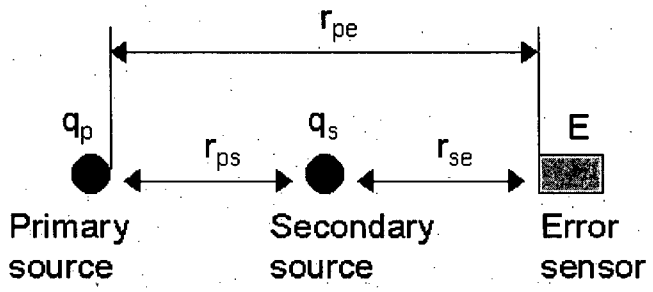

Figure 2.3: Single-channel local ANC setup in the free field.

and the minimum total power output of the single-channel control system is

$$W_T = \frac{1}{2}|q_p|^2 Z_o \left(1 - \text{sinc}^2 kr_{ps}\right) = W_o \left(1 - \text{sinc}^2 kr_{ps}\right). \tag{2.5}$$

If the system achieves more than 10dB of attenuation in a given area, it is said to have created a quiet zone [2]. The size of the quiet zone depends on the relative positions of the primary source, the secondary source and the error sensor. In order to create a quiet zone, the control system must be configured such that the wavefronts of the primary and secondary signals are equal in amplitude and opposite in phase at the error sensor, so that cancellation occurs. This is known as wavefront matching [2].

2.3.2 Multiple-source, Muliple-channel Control

The equations shown in the previous section can be generalized to the case of multiple primary sources and multiple control channels. For M primary sources and N secondary sources in free space, the corresponding source strengths can be represented as

$$\mathbf{q}_p = [q_{p1}, q_{p2}, ..., q_{pM}]^T, \tag{2.6}$$

$$\mathbf{q}_s = [q_{s1}, q_{s2}, ..., q_{sN}]^T. \tag{2.7}$$

The complex pressures at the L error microphones are

$$\mathbf{P} = \mathbf{Z}_{pe}\mathbf{q}_p + \mathbf{Z}_{se}\mathbf{q}_s, \tag{2.8}$$

and the cost function, J, is the sum of the squared pressures at the error microphones, given by

$$J = \mathbf{P}^H\mathbf{P} = (\mathbf{Z}_{pe}\mathbf{q}_p + \mathbf{Z}_{se}\mathbf{q}_s)^H(\mathbf{Z}_{pe}\mathbf{q}_p + \mathbf{Z}_{se}\mathbf{q}_s), \tag{2.9}$$

where $\mathbf{Z}_{pe}$ is an $L \times M$ matrix of the acoustic transfer impedances from the primary sources to the error sensors, and $\mathbf{Z}_{se}$ is an $L \times N$ matrix of the transfer impedances from the secondary sources to the error sensors [14]. The strengths of the secondary sources can be optimized to minimize the magnitude of the cost function. If $L = N$, then the optimal secondary source strengths are given by [14]

$$\mathbf{q}_{sO} = -\mathbf{Z}_{se}^{-1}\mathbf{Z}_{pe}\mathbf{q}_p. \tag{2.10}$$

For a line of primary sources and a line of secondary sources and control channels, such that $L = N$, the acoustic power outputs are [14]

$$W_p = \frac{1}{2}\left[\mathbf{q}_p^H \mathrm{Re}(\mathbf{Z}_{pp})\mathbf{q}_p + \mathbf{q}_p^H \mathrm{Re}(\mathbf{Z}_{ps}^T)\mathbf{q}_s\right] \tag{2.11}$$

$$W_s = \frac{1}{2}\left[\mathbf{q}_s^H \mathrm{Re}(\mathbf{Z}_{ss})\mathbf{q}_s + \mathbf{q}_s^H \mathrm{Re}(\mathbf{Z}_{ps}^T)\mathbf{q}_s\right] \tag{2.12}$$

and the total power output of the system is

$$W_T = \frac{1}{2}\left[\mathbf{q}_p^H \mathrm{Re}(\mathbf{Z}_{pp})\mathbf{q}_p + \mathbf{q}_s^H \mathrm{Re}(\mathbf{Z}_{ss})\mathbf{q}_s + \mathbf{q}_p^H \mathrm{Re}(\mathbf{Z}_{ps}^T)\mathbf{q}_s + \mathbf{q}_s^H \mathrm{Re}(\mathbf{Z}_{ps}^T)\mathbf{q}_p\right] \tag{2.13}$$

where $\mathbf{Z}_{pp}$ is an $M \times M$ matrix of the transfer impedances between the primary sources, $\mathbf{Z}_{ss}$ is an $N \times N$ matrix of the transfer impedances between the secondary sources and $\mathbf{Z}_{ps}$ is an $M \times N$ matrix of the transfer impedances between the primary and secondary sources [14].

For multiple control sources spaced evenly in a line, it has been shown that

there is an optimal range for the spacing of the secondary sources. The upper limit is given by [14, 15]

$$r_{ss-max} = \frac{\lambda}{2}\sqrt{1+\frac{4r_{se}}{N\lambda}} \quad N \text{ even}, \tag{2.14}$$

$$r_{ss-max} = \frac{\lambda}{2}\sqrt{1+\frac{N+1}{N-1}\frac{4r_{se}}{N\lambda}} \quad N \text{ odd}, \tag{2.15}$$

$$\tag{2.16}$$

and the lower limit is

$$r_{ss-min} = \sqrt{1+\frac{4}{N}}\exp\left(-\left[\frac{2\lambda}{r_{se}}+\sqrt{\frac{\lambda}{r_{ps}}}\right]\right) \quad N \text{ even}, \tag{2.17}$$

$$r_{ss-min} = \sqrt{1+\frac{6(N+1)}{N(N-1)}}\exp\left(-\left[\frac{2\lambda}{r_{se}}+\sqrt{\frac{\lambda}{r_{ps}}}\right]\right) \quad N \text{ odd}. \tag{2.18}$$

The optimal spacing is defined as the value of r_{ss} that gives the least total power output increase and the largest quiet zone. In the case of multiple channel control with equally-spaced secondary sources and error sensors placed in two parallel lines, as shown in Fig. 2.4, the quiet zone in the horizontal plane is triangular [14].

The vector $\mathbf{q}_p$ in Eq. 2.13 is used to express the strengths of the primary sources. A dipole primary source can be modeled with two monopoles that are opposite in phase, separated by a distance d. Then the vector $\mathbf{q}_p$ is given by

$$\mathbf{q}_p = \begin{bmatrix} q_s \\ -q_s \end{bmatrix}, \tag{2.19}$$

the transfer impedances among the primary sources are a 2×2 matrix as

$$\mathbf{Z}_{pp} = iZ_0 \begin{bmatrix} 1 & \exp(-ikd)/kd \\ \exp(-ikd)/kd & 1 \end{bmatrix}, \tag{2.20}$$

and the transfer impedances between the dipole primary source and the N control sources are a $2 \times N$ matrix given by

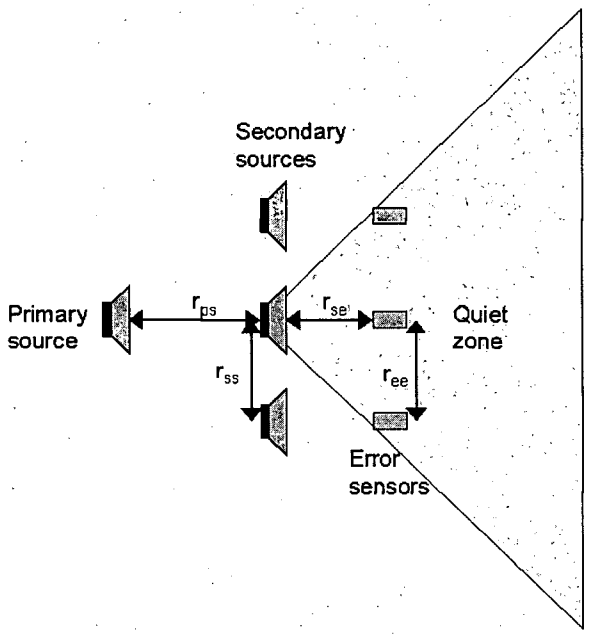

Figure 2.4: The shape of the quiet zone produced by a multichannel ANC system, in the horizontal plane.

$$\mathbf{Z}_{ps} = iZ_0 \begin{bmatrix} \frac{\exp(-ikr_{p1s1})}{kr_{p1s1}} & \frac{\exp(-ikr_{p1s2})}{kr_{p1s2}} & \cdots & \frac{\exp(-ikr_{p1si})}{kr_{p1si}} & \cdots & \frac{\exp(-ikr_{p1sN})}{kr_{p1sN}} \\ \frac{\exp(-ikr_{p2s1})}{kr_{p2s1}} & \frac{\exp(-ikr_{p2s2})}{kr_{p2s2}} & \cdots & \frac{\exp(-ikr_{p2si})}{kr_{p2si}} & \cdots & \frac{\exp(-ikr_{p2sN})}{kr_{p2sN}} \end{bmatrix}, \tag{2.21}$$

where r_{p1si} and r_{p2si} are the distances from one of the two monopoles of the primary dipole to the ith secondary source, respectively [14]. A quadrupole primary source can be defined in an analogous way, using a four-element vector with two positive q_s values and two negative q_s values, a 4×4 matrix for $\mathbf{Z}_{pp}$, and a $4 \times N$ matrix for $\mathbf{Z}_{ps}$.

2.4 Half-space Local Active Control

There are few real situations in which the free-field approach can be used. The half-space condition is more practical from an engineering perspective. In a half-space, the control system is assumed to be placed above a totally reflective surface. The presence of a reflective surface will have an effect on the performance of the control system.

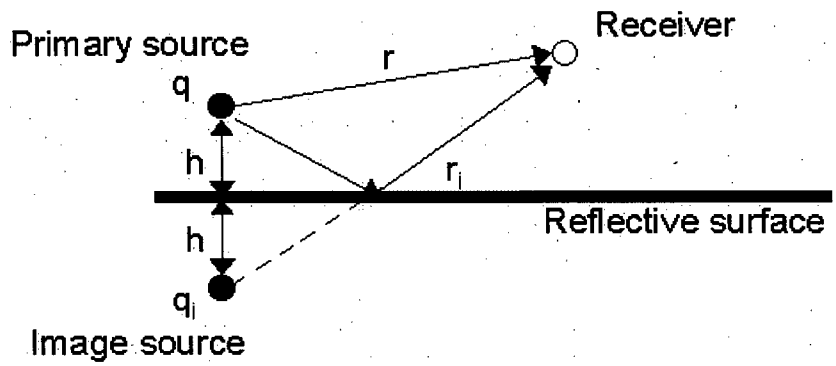

Figure 2.5: A point source above a reflective surface.

2.4.1 Image-source Analysis

In the theoretical analysis of a point source radiating above a reflective plane, the plane can be thought of as creating an image source. In Fig. 2.5, the strength of the point source located at a height h above the plane is given by q and the strength of the image source is given by $q_i = C_r q$ where C_r is the reflection coefficient of the plane [16]. The complex sound pressure at the receiver is

$$P = iZ_0 q \left[\frac{\exp^{-ikr}}{kr} + \frac{C_r \exp^{-ikr_i}}{kr_i} \right] \tag{2.22}$$

where r is the distance from the point source to the receiver and r_i is the distance from the image source to the receiver. The sound power output of the point source above the reflective plane is given by

$$W_h = W_0(1 + R_{p'p}) \tag{2.23}$$

where $W_0 = \frac{1}{2} Z_0 |q|^2$ is the power output of the point source in the absence of the plane, $Z_0 = \omega^2 \rho / 4\pi c_0$ and $R_{p'p} = \mathrm{Re}(iC_r \exp^{i2kh} / 2kh)$ [16].

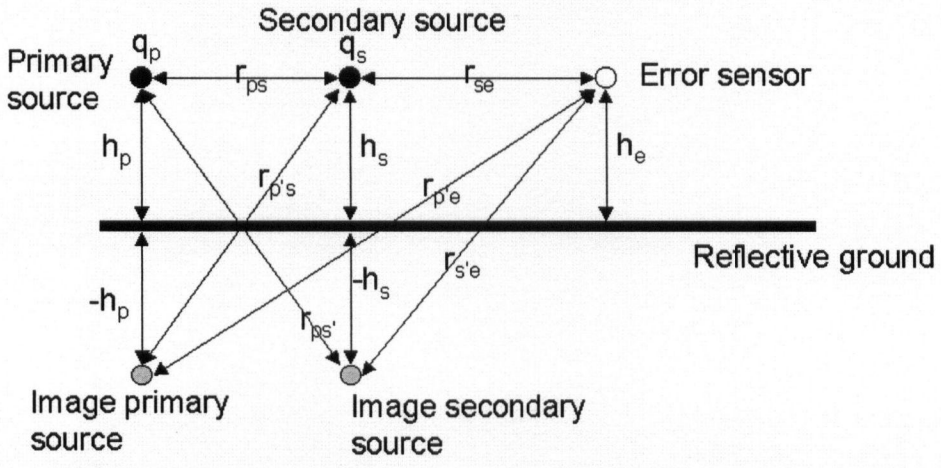

Figure 2.6: Single-channel ANC system in a half-space.

2.4.2 Local Control System in a Half-Space

An active control system above a reflective plane in shown in Fig. 2.6. As before, q_p and q_s are the strengths of the primary and secondary sources, E is the position of the error sensor and r_{ps}, r_{pe} and r_{se} are the distances between the primary and secondary source, the primary source and error sensor, and the secondary source and error sensor, respectively. The contribution of the reflective plane to the sound field is accounted for by the image primary and secondary sources. $r_{p's}$, $r_{s'p}$, $r_{p'e}$ and $r_{s'e}$ are respectively the distances from the primary image source to the secondary source, the secondary image source to the primary source, the primary image source to the error sensor and the secondary image source to the error sensor. The height of the primary source, secondary source and error sensor above the plane are equal, such that $h_p = h_s = h_e$.

The acoustic transfer impedances between the primary source and error sensor, and between the secondary source and error sensor are [14, 16]

$$Z_{pe} = iZ_0 \left(\frac{\exp(-ikr_{pe})}{kr_{pe}} + C_r \frac{\exp(-ikr_{p'e})}{kr_{p'e}} \right) \tag{2.24}$$

$$Z_{se} = iZ_0 \left(\frac{\exp(-ikr_{se})}{kr_{se}} + C_r \frac{\exp(-ikr_{s'e})}{kr_{s'e}} \right). \tag{2.25}$$

To minimize the sound pressure at the error microphone, the required strength of the control source is

$$q_s = Aq_p \tag{2.26}$$

where $A = -Z_{pe}/Z_{se}$. The total sound power of the system is given by

$$W_{Th} = W_0 \left[1 + R_{p'p} + 2 \left(\mathrm{sinc}(kr_{ps}) + \mathrm{Re} \left(iC_r \frac{\exp(-i2kh_s)}{kr_{p's}} \right) \right) \mathrm{Re}(A) + |A|^2 (1 + R_{s's}) \right] \tag{2.27}$$

where $R_{p'p}$ is as defined in Eq. 2.16 and $R_{s's} = \mathrm{Re}(iC_r \exp(-i2kh_s)/2kh_s)$ [14, 16]. The total sound pressure at any point above the reflective plane is

$$P = Z_{pl}q_p + Z_{sl}q_s \tag{2.28}$$

where

$$Z_{pl} = iZ_0 \left(\frac{\exp(-ikr_{pl})}{kr_{pl}} + C_r \frac{\exp(-ikr_{p'l})}{kr_{p'l}} \right), \tag{2.29}$$

$$Z_{sl} = iZ_0 \left(\frac{\exp(-ikr_{sl})}{kr_{sl}} + C_r \frac{\exp(-ikr_{s'l})}{kr_{sl}} \right). \tag{2.30}$$

In Eqs. 2.21 to 2.23, the subscript l denotes the position of the observation point in the half-space. r_{pl}, $r_{p'l}$, r_{sl} and $r_{s'l}$ are the distances from the observation point to the primary source, the primary image source, the secondary source, and the secondary image source, respectively [14, 16].

Although the half-space condition is more practical from an engineering perspective, it is very difficult to achieve in an experimental setting. A half-space can be approximated in an outdoor, open space environment, but the far-field results will be affected by constantly changing environmental conditions. A hemi-anechoic chamber, which is an anechoic chamber with a reflective floor, may be a good approximation of a half-space if the dimensions of the floor are large with respect to

the wavelength of sound. However, since the frequencies of interest for ANC ($\sim$ 100Hz) have wavelengths of several meters long, the anechoic chamber would have to be very large to approximate half-space conditions.

It is still of interest to study the free-field condition, particularly for directional sources. Theoretical and experimental studies of a dipole source in the free-field will be discussed in the next chapter.

Chapter 3

Active Control of Dipole Noise – Experiments

3.1 Introduction

Although ANC has been studied extensively in recent years, most of the research has concentrated on simple monopole point sources. In practice, many real noise sources are directional and cannot be approximated by a monopole source. In particular, moving noise sources tend to have multipole directivity. Lighthill's acoustic analogy, which states that unsteady aerodynamic fluid flow can be replaced by a volume distribution of equivalent acoustic sources throughout the flow field, establishes that jet noise can be modeled by quadrupole sources [17].

For propeller noise, there are three general mechanisms by which noise is generated: steady sources, unsteady sources and random sources. Unsteady and random sources will be described in the next chapter. Steady sources include thickness and loading noise, which can be represented as a monopole at low rotational speeds. At high rotational speeds, when the flow over the blades is transonic, nonlinear effects become significant. The flow can be modeled with quadrupole sources in the volume surrounding the blades [17]. Since propeller noise becomes increasingly directional at higher rotational speeds, it is important to study the effectiveness of an ANC system on directional sources.

The effectiveness of an active control system on a dipole primary source was investigated in a free-field environment. The control efficiency was considered in terms of the total power output increase and the size of the quiet zone. Since the performance of the control system will depend on the orientation of the dipole source, three different orientation angles θ were studied: 0°, 45° and 90°. The

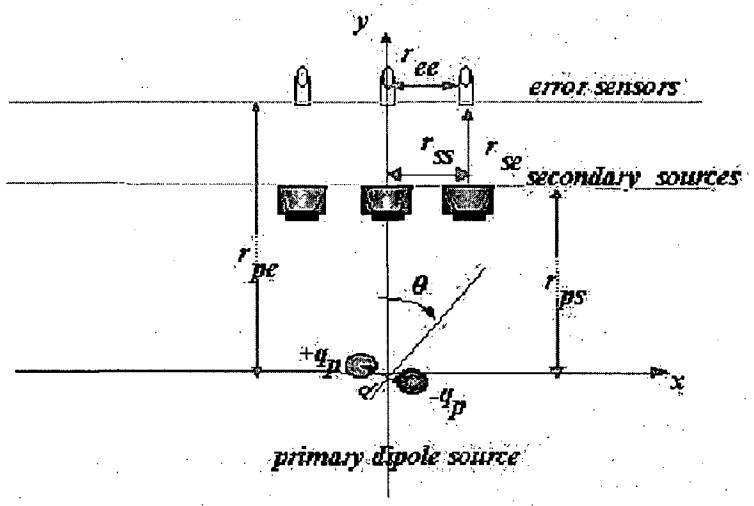

Figure 3.1: Multichannel local ANC system for a dipole primary source.

angles are defined as shown in Fig. 3.1. The simulation and experimental results are compared and discussed in this chapter.

3.2 Creating a source with dipole radiation

Previous ANC experiments at the University of British Columbia were done using identical enclosed loudspeakers as the primary source and the secondary sources [2]. The radiation of an enclosed loudspeaker is approximately omnidirectional at low frequencies. For the current research, a dipole primary source was needed. It has been shown that an unenclosed loudspeaker has approximately dipole directivity [18]; this was the starting point for the design of a dipole source in this study.

As a first attempt to create a source with dipole radiation, the back of a $0.28 \times 0.28 \times 0.24\text{m}^3$ enclosure containing an 8" (0.20m) speaker was removed. The 250Hz octave band directivity of the source at a distance of 0.5m is shown in Fig. 3.2. The directivity is asymmetrical, as the radiation to the front is about 5dB stronger than to the back. The levels directly in front of and behind the speaker were between 8 and 14dB higher than those measured directly to each side.

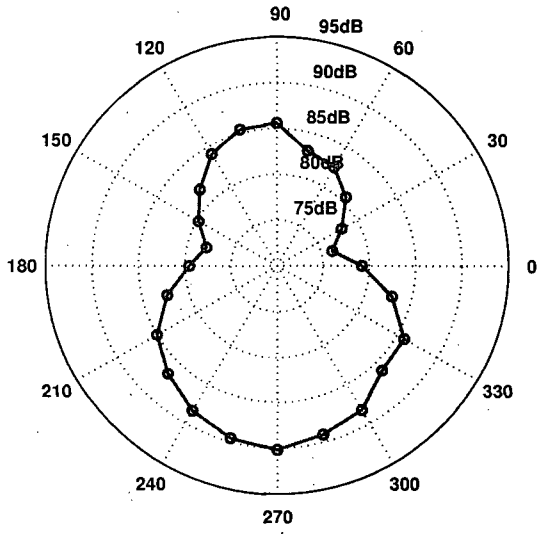

Figure 3.2: Measured 250Hz octave band directivity of an 8" (0.20m) speaker in a $0.28 \times 0.28 \times 0.24\text{m}^3$ *enclosure with the back removed.*

In attempt to improve the symmetry of the dipole radiation, a $0.30 \times 0.28 \times 0.30\text{m}^3$ enclosure with no front and back was built such that the speaker position could be adjusted. The symmetry of the directivity could be improved by moving the speaker towards the center of the enclosure. The best directivity that was achieved in the 250Hz octave band is shown in Fig 3.3. The radiation is now symmetric, with nulls of about 25dB to the sides. The improved dipole source was used in the active control experiments.

3.3 Control System Configuration

As discussed in Chapter 2, two measures of the effectiveness of a local control system are the total power output and the size of the quiet zone. For a multiple channel control system, the total power output and the size of the quiet zone will depend on the spacing of the control channels. Using Eqns. 2.13 and 2.19 to 2.21, the total power output was calculated for a 3-channel local control system with $r_{ps} = r_{se} = 1.0\text{m}$, for three orientations of a dipole source: 0°, 45° and 90°. The

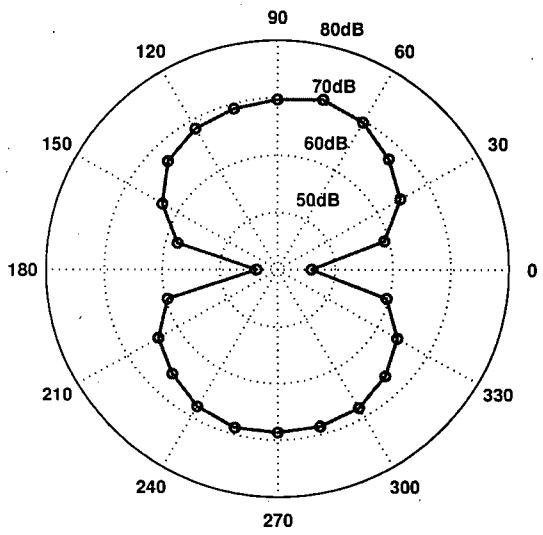

Figure 3.3: Measured 250Hz octave band directivity of an 8" (0.20m) speaker placed in the center of a $0.30 \times 0.28 \times 0.30\text{m}^3$ *enclosure with the back removed.*

results are shown in Fig. 3.4 for normalized secondary speaker separations r_{ss}/λ in terms of the total power output increase, ΔW, which is

$$\Delta W = \frac{W_T}{W_p} \tag{3.1}$$

where W_T is as defined in Eq. 2.13 and W_p is the power of the primary source. In Fig. 3.4, the results for W_T have been presented on a dB scale. The results for a monopole source are also shown for reference. In the case of a monopole, the range of optimal separation is large. The total power output increase is less than 1dB for separations smaller than about $0.73 r_{ss}/\lambda$. For a dipole primary source, there is still an optimal range for r_{ss}, but it is smaller than in the case of a monopole. When the dipole is oriented at $\theta = 0°$ (null of the dipole radiation facing the control system) the control channels must be placed close together. When $\theta = 45°$, the optimal range increases, but the ΔW_T also increases by a few dB. When $\theta = 90°$ the optimal range and ΔW_T increase further. The results shown in Fig. 3.4 will be used to choose r_{ss} for the dipole experiments.

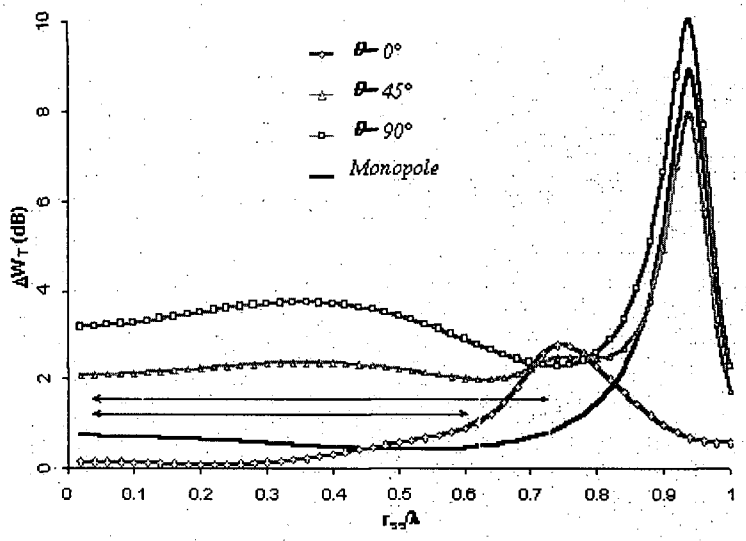

Figure 3.4: Total power output increase for a 3-channel ANC system as a function of the normalized secondary speaker spacing, r_{ss}/λ, for $r_{ps} = r_{se} = 1.0m$ [19].

3.4 Dipole Local Control Experiments

The experiments were conducted in an anechoic chamber at the University of British Columbia. The dimensions of the chamber are $4.7 \times 4.2 \times 2.2\text{m}^3$. The configuration of the control system is shown in Fig. 3.5. The dipole primary source was placed 0.5m from the back wall of the chamber and 1.25m above the floor. The control speaker array consisted of three enclosed loudspeakers (monopoles), spaced at equal distances from each other. The error-sensor array of three equally-spaced microphones was placed in front of the control speakers. The distance between the primary source and the control speaker array, r_{ps}, and the distance from the secondary speaker array to the error microphone array, r_{se}, were set equal at 1.0m. The separation of the control sources, r_{ss}, and the separation of the error microphones, r_{ee}, were equal, and varied with the dipole orientation according to its optimal range, as shown in Fig. 3.4. Both the control-source array and the error-microphone array were placed at the same height as the dipole source.

A commercially available multi-channel EZ-ANC system was used as the ANC

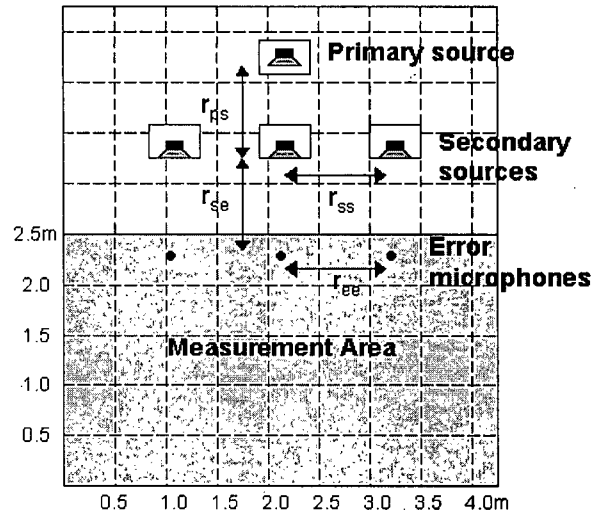

Figure 3.5: Set-up of the 3-channel ANC experiment in the anechoic chamber.

controller. Germain showed that the fundamental frequency of the Beechcraft 1900D was 112.5Hz, and it is expected that the Dash-8 will also have a low fundamental frequency. It is thus of interest to perform the experiments using a low frequency pure tone ($\sim$ 100Hz). However, because of its dimensions, the chamber is not fully anechoic at low frequencies. Thus, the test signal was chosen to be 200Hz, which is above the cut-off frequency of the anechoic chamber. The primary source was driven by a signal generator, which also provided a reference signal to the controller. The noise measurements were carried out in a plane at the same height as the control system. The measurement grid had a 0.5m resolution, which yielded 45 measurements in the measurement plane.

The performance of a three-channel active control system for the dipole primary source was tested for three different orientations: $\theta = 0°, 45°$ and $90°$. Both the primary and controlled sound fields were measured for each dipole orientation over the same measurement grid. The difference between the two fields was calculated to obtain the amount of attenuation achieved by the control system. Using the results shown in Fig. 3.4, r_{ss} values of $r_{ss} = 0.4\lambda$ for $0°$, $r_{ss} = 0.64\lambda$ for $45°$ and $r_{ss} = 0.75\lambda$ for $90°$ were chosen. These values correspond to $r_{ss} = 0.67$m for

0°, r_{ss} = 1.07m for 45° and r_{ss} = 1.25m for 90° at 200Hz.

3.4.1 Dipole at 0°

The simulation and experimental results in the plane of the control system for the dipole oriented at 0° are shown in Fig. 3.6. The total power output increase, ΔW, has been expressed in dB and is denoted by ΔP. The predicted results assume a perfect dipole, in which the sound radiation at 0° and 180° is zero. As a result, it cannot predict any noise attenuation down the center of the dipole where x = 2.0m. The predicted power output increase is symmetric, with very small quiet zones (> 10dB of attenuation) to the sides. Note that the vertical scale has been set such that the minimum is -10dB. The experimental results show that very small quiet zones were produced in the corners (far from the control system). In agreement with the simulation results, the sound level increase in other areas is small. Discrepancies in the shape of the ΔP field can be attributed to the fact that the simulations predict for a perfect dipole source, while the dipole source used in the experiments did not have perfect nulls at 0° and 180°.

3.4.2 Dipole at 45°

Fig. 3.7 shows the simulation and experimental results for the dipole oriented at 45°. The primary sound field in the measurement plane is now asymmetric, and the control results are also asymmetric. The simulation results show that a quiet zone is achieved over much of the measurement plane. Towards the edge of the plane where x = 4m, the dipole radiation is theoretically zero, and the total power output of the system is increased. In the experimental results, a small quiet zone was achieved far from the primary source, between x = 0.5m and x = 2.5m. In other areas of the strong primary soruce directivity, an average of about 5dB of attenuation was achieved. Close to the "null" of the primary source, the total power output of the system was increased, as was the case of the simulation results.

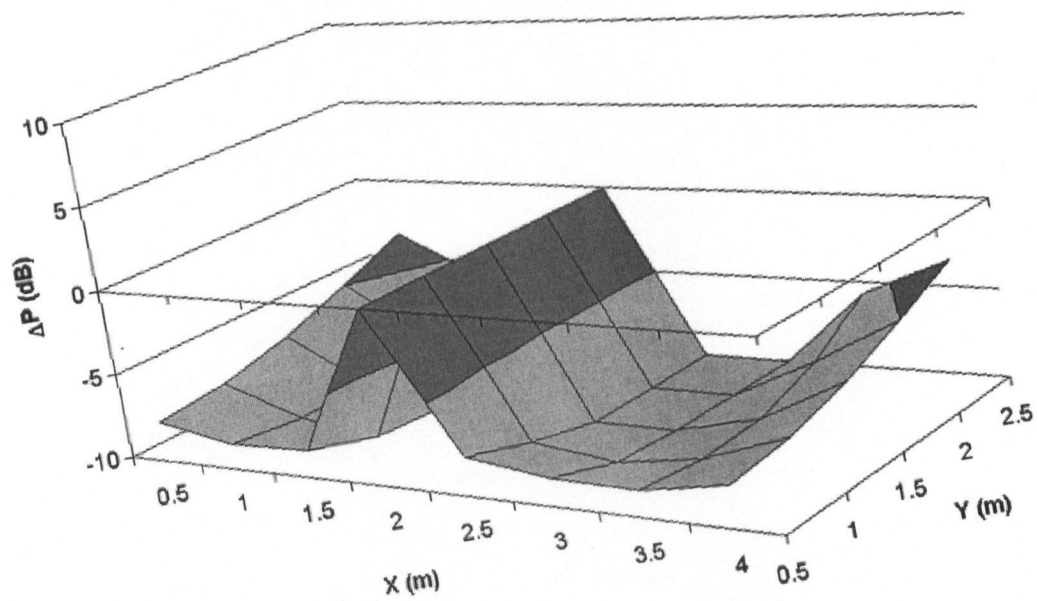

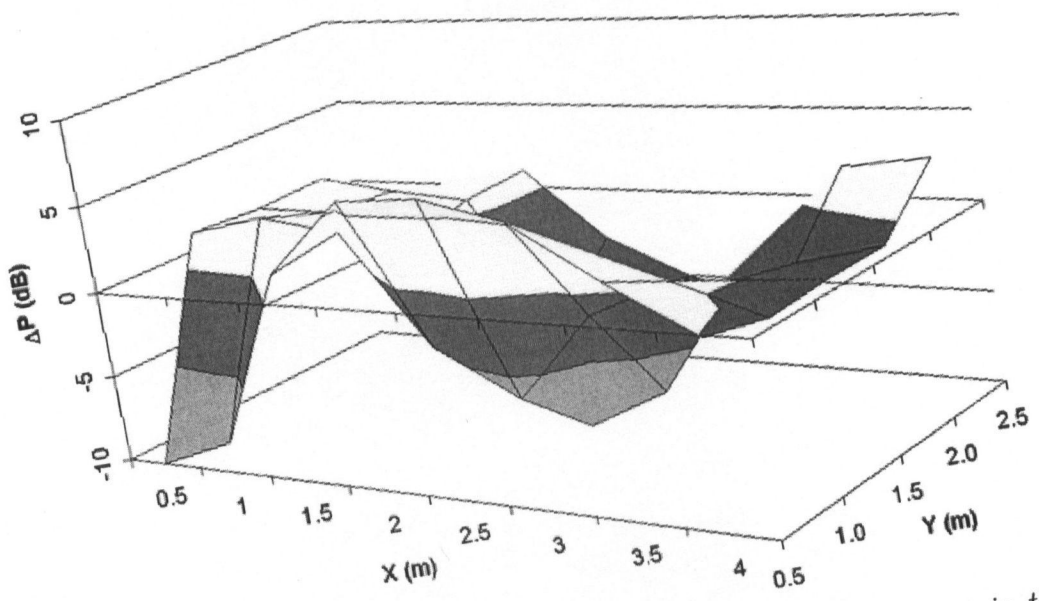

Figure 3.6: Predicted (top) and measured (bottom) noise attenuation in the plane of the ANC system for a dipole primary source oriented at 0° with $r_{ss} = 0.67m$.

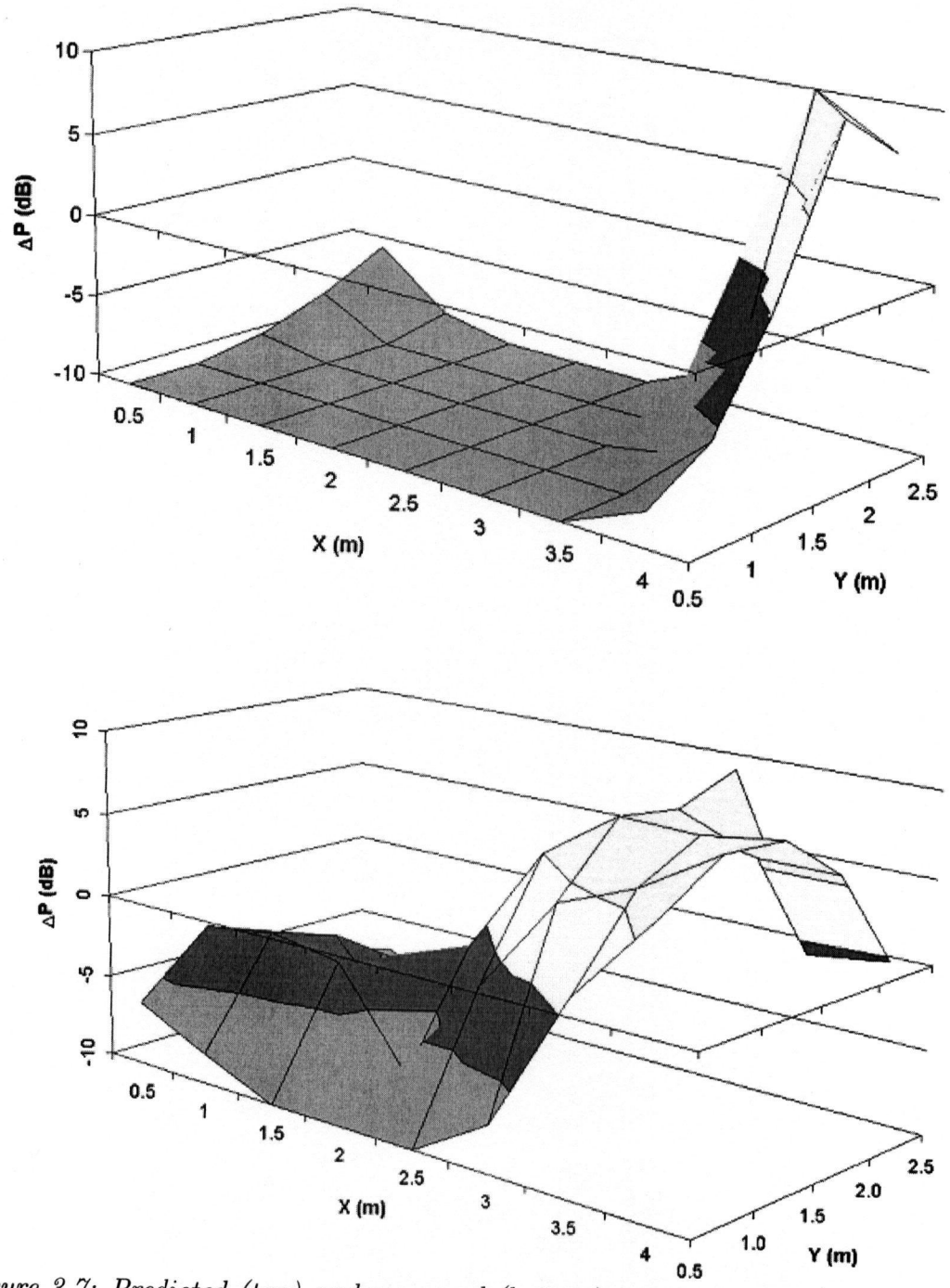

Figure 3.7: Predicted (top) and measured (bottom) noise attenuation in the plane of the ANC system for a dipole primary source oriented at 45° with $r_{ss} = 1.07m$.

3.4.3 Dipole at 90°

The results for the dipole oriented at 90° are shown in Fig. 3.8. In this configuration, the maximum radiation of the dipole was directed towards the control system. The simulation results show that a quiet zone was achieved almost everywhere in the measurement plane. A large quiet zone was also shown in the experimental results. In the areas where a quiet zone was not achieved, some attenuation was still seen, and the overall total sound power output increase of the control system in the measurement plane was negative. The control system is clearly the most effective when it is used to create quiet zones in the area with the strongest primary directivity.

3.5 Summary

It has been shown that a loudspeaker placed in the center of an enclosure with the front and back removed is a good approximation of a dipole source at low frequencies. The equations for the total power output of the control system were used to calculate the optimal range of separation of the control channels for three different orientations of a dipole primary source. When the null of the dipole is facing towards the control system ($\theta = 0°$), the control channels must be placed close together to achieve minimal total sound power output increase. The overall effectiveness of a local control system for this configuration is low, as the quiet zones that are produced are very small. For a dipole primary source oriented at 45°, attenuation was achieved in the area of strong primary source directivity, but the noise increased in other areas. The control system was most effective when it was used to control a primary dipole source oriented at 90°. In this case, the control array was facing the direction of the strongest primary directivity, and a large quiet zone was created. Simulations on the active control of a quadrupole source in the free-field performed by Guo resulted in similar conclusions [13].

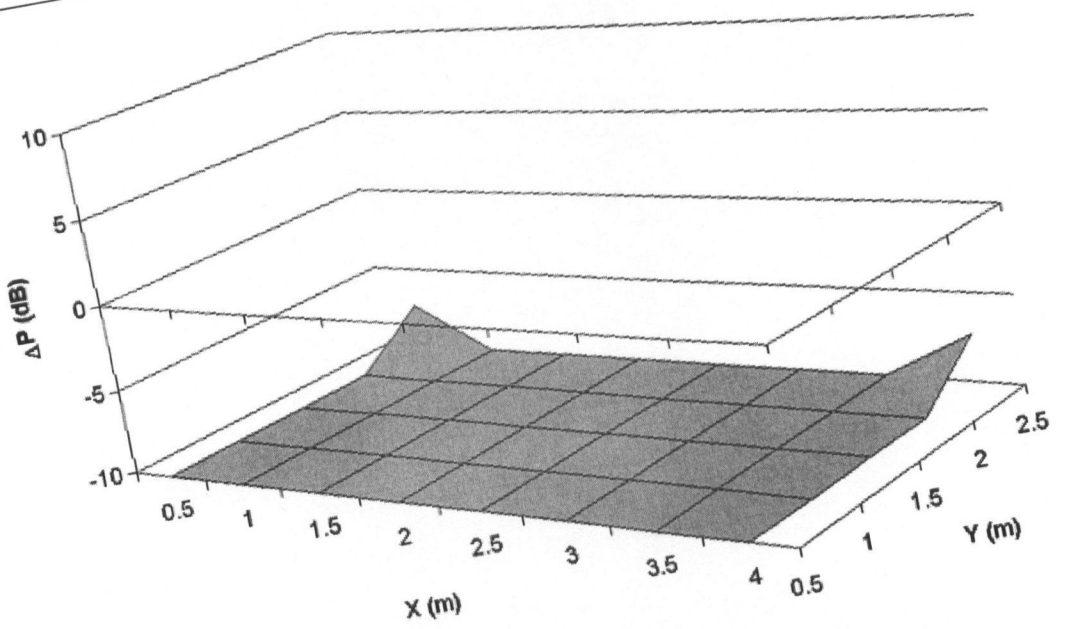

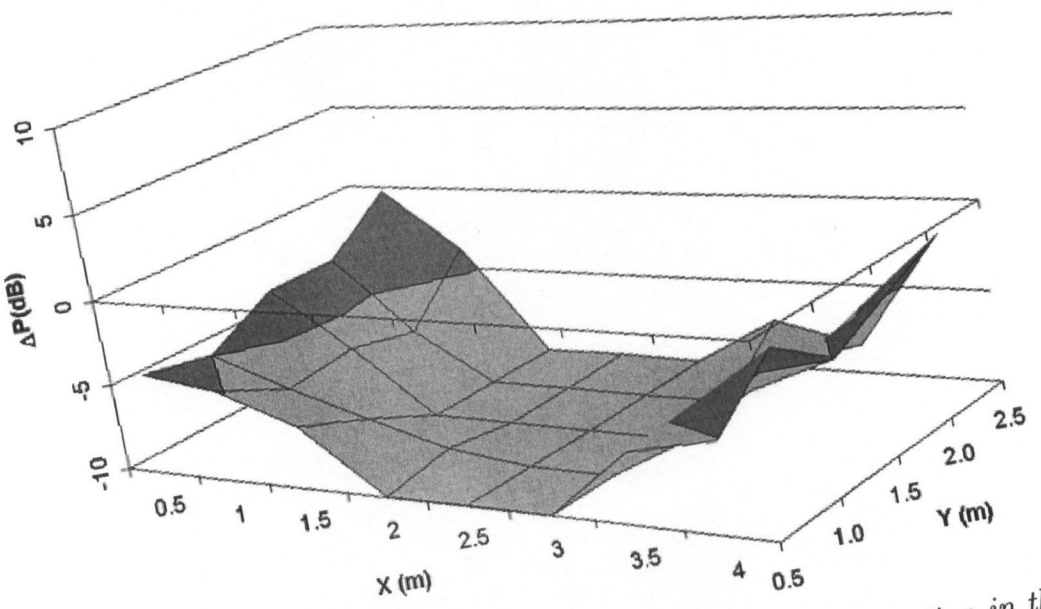

Figure 3.8: Predicted (top) and measured (bottom) noise attenuation in the plane of the ANC system for a dipole primary source oriented at 90° with $r_{ss} = 1.25m$.

The simulation and experimental results that were presented in this chapter have provided some understanding as to how directional noise sources can be controlled using multi-channel local control. It is essential to have an understanding of the directivity and spectral characteristics of the noise source before active control can be considered. The next chapter describes the analysis of Dash-8 run-up noise measurements.

Chapter 4

Run-up Noise Measurement and Analysis

4.1 Introduction

In order to design an effective active control system for aircraft propeller noise, it is necessary to understand how the engines and propellers act together as a noise source. Germain [2] recorded noise from a Beechcraft during normal run-up conditions and studied the spectra at various positions around the aircraft at distances of 73m, 98m, and 3km. The main objectives of Germain's work were to determine the noise directivity of the aircraft, find the blade-passing frequency (BPF) for ANC, and to evaluate the insertion loss of a blast fence located at the run-up site [2]. While this information was useful, in order to design an effective ANC system for the aircraft, a more detailed understanding of how the aircraft radiates noise and how the directivity changes for different engine settings is required. Furthermore, it was of interest to study the deHavilland Dash-8 aircraft, which is a source of noise complaints at the Vancouver International Airport.

Recordings of the noise from a deHavilland Dash-8 aircraft, provided by Air Canada Jazz (see Fig. 4.1), were made at Vancouver International Airport in August 2002. Details of the measurement procedure are presented in Section 4.2. The measured narrow-band and 1/3 octave band spectra were calculated, and analyzed in detail to determine the BPFs and noise directivities for three different engine settings (idle, 50% power and full power). The effect of the ground reflection on the noise spectra was also considered. Using Germain's results for the measurements taken 3 km away from the run-up site, estimates of the Dash-8 noise levels in the far field were made. Decibel subtraction of the idle engine spectra from the

Figure 4.1: Photograph of the deHavilland Dash-8 100. Source: www.aircanada.ca.

50% engine power spectra was performed in attempt to obtain the power spectra of a single engine operating at 50% power. Idle engine spectra are presented in Appendix A, full power spectra are shown in Appendix B, and the 50% engine power spectra and the decibel subtracted spectra are shown in Appendix C.

4.2 Run-up Noise Measurements

The deHavilland Dash-8 100 series has two PW120 turboprop engines of power 2000 shp. It has a wingspan of 25.9m, length of 22.3m and height of 7.49m, and is capable of carrying 37 to 39 passengers. The two propellers are Hamilton standard 14SF-7 four-blade reversible-pitch of diameter 3.96 m, and are centered at about 4.3 m above the ground [20].

The run-up measurements were performed on a clear summer night with low wind. Receiver microphones were positioned on a circle of radius 40m (measured from the center of the aircraft) at 20° increments, as shown in Fig. 4.2. The area

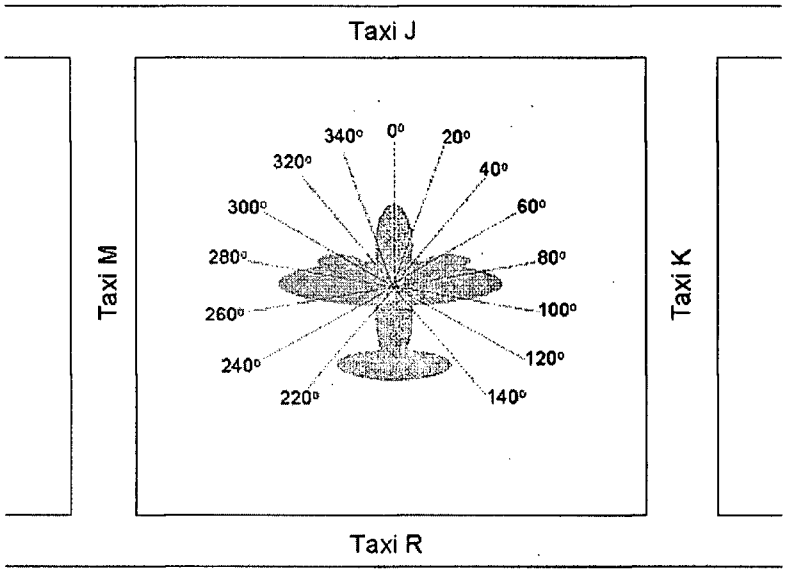

Figure 4.2: Measurement positions around the Dash-8.

area directly behind the plane was excluded due to excessive wind from the propellers, and because of safety concerns. Four different 1/2" free-field microphones, in combination with a conditioning amplifier or sound level meter, were used to record the data at the various positions; details are provided in Table 4.1. Each of the microphones was covered with a windscreen to reduce the wind noise in the recordings. Portable Sony PCM-M1 DAT recorders were used to capture the data at a sampling rate of 48kHz. A pure tone of amplitude 94dB at 1000Hz was recorded with each microphone at a noted gain setting for calibration. In total, noise was recorded at 15 positions around the aircraft for three conditions: both engines idling, both engines at full power, and the right engine at 50% power while the left engine was idling (it was not possible to run one engine at full power while the other idled).

The aircraft first ran both of the engines at idle settings, and the noise was recorded at four microphone positions for one minute. The microphones and DAT recorders were then moved to their next positions, and the process was repeated until all of the positions were covered. The aircraft then increased both of the

Table 4.1: Microphones used for the Dash-8 run-up recordings.

Microphone	Positions
Quest 2900 Sound Level Meter	220°, 240°, 260°
Quest 155 Sound Level Meter	280°, 300°, 320°
Bruel and Kjaer 4190	340°, 0°, 20°, 40°, 60°, 80°
Rion NA-29 Sound Level Meter	100°, 120°, 140°

engines to full power, and the noise was recorded at each position for 30 seconds. Finally, the aircraft decreased the left engine to idle and the right engine to 50% power, and the noise was again recorded at each position for 30 seconds.

The run-up noise recordings were downloaded to a computer as text files and analyzed with Matlab. For each run-up condition, at each position, narrow-band, 1/3 octave band and total noise levels were calculated, both unweighted and A-weighted. Spectral analysis is discussed in Section 4.3; noise directivity is discussed in Section 4.4.

4.3 Spectral Analysis

1/3 octave band and narrow-band spectra were studied to identify any characteristic frequencies (BPF and harmonics, peaks, dips, etc.) and how they differ at the various positions around the aircraft. To find the total unweighted and A-weighted levels at each position around the aircraft, each data set was truncated to 5×10^5 samples (corresponding to about 10 seconds of data) and filtered into 1/3 octave bands. Using calibration tones that were recorded for each microphone, reference levels were determined to convert the signal amplitudes into sound-pressure levels in dB. The unweighted and A-weighted levels were calculated for 1/3 octave bands from 16 to 8000Hz, and these results were used to calculate the total levels. The 1/3 octave band spectra and narrow-band spectra up to 1250Hz are shown in the appendices.

4.3.1 Idle Engine Spectra (Figs. A.1 to A.10)

The dominant frequency in the narrow-band spectra at most of the measurement positions was 18Hz; this is the BPF of the Dash-8 at idle engine power. A spike in the spectra at this frequency was clearly visible at all positions except 340° and 0°, the positions furthest away from the propellers. The amplitude at the BPF was as high as 79dB at measurement positions that were close to the propellers. First and second harmonics were only distinct in the spectra closest to the left propeller. A spike in the spectra at 365Hz was clearly visible at almost all of the measurement positions; its amplitude exceeded that of the BPF towards the front of the aircraft. The reasons for the spike at this frequency are unknown.

At all of the positions except 40° and 60°, there was a dip in the spectra at mid-frequencies (800Hz to 1.6kHz). At positions close to the propellers (from 220° to 280°, and from 100° to 140°), there was a also a slight dip at 315Hz. The noise spectra at the positions to the front of the aircraft (from 300° to 80°) show the loudest noise levels between 2kHz and 4kHz. The noise contribution at the BPF was not significant enough to cause a spike in the 16Hz or 20Hz bands of the 1/3 octave band spectra. Thus, at idle engine power, the noise contribution at the BPF is not significant enough to dominate the overall noise spectra. Given also that the harmonics were weak or insignificant, it can be concluded that idling engine noise does not contain enough tonal noise to be controlled by ANC.

Broadband noise is generated by random sources. One such source is the interaction of inflow turbulence with the blade leading edges. A second source is the blade trailing edge [17]. Since the propellers are rotating relatively slowly, steady sources (discussed in Chapter 3) and unsteady sources (to be discussed in the next section) are insignificant, and the idling engine noise is broadband.

Germain [2] did not analyze the idle engine spectra in detail; the idle engine noise was recorded mainly to compare the idle engine and full-power engine noise levels. At a distance of 98m, the total A-weighted idle engine noise level of the

Beechcraft was about 83dBA [2]. For the Dash-8 at a distance of 40m, the total A-weighed noise levels ranged between 80 and 100dBA. Since the noise levels were measured at different distances, it is difficult to compare the noise levels of the two aircraft directly.

4.3.2 Full Power Engine Spectra (Figs. B.1 to B.10)

As the propellers rotate more quickly, their contribution to the noise spectra becomes more significant. At full engine power, the BPF is 80Hz. The noise amplitude at this frequency reached as high as 120dB at 100°. At the measurement positions closest to the right propeller (100°, 120° and 140°), the noise at the BPF was clearly dominant over the harmonics. At other positions, the amplitudes of the first and second harmonics were close to or exceeded the amplitude of the BPF. Towards the front of the aircraft (340°, 0° and 20°), the amplitudes of the harmonics were constant within about 5dB until the seventh harmonic. Here, the noise of the second and higher harmonics is louder than that at positions closer to the propellers.

As mentioned in Chapter 3, one of the noise-generating mechanisms for propellers is that from unsteady sources. Unsteady sources include periodic and random variations of loading on the blades. The spectra of a single rotating propeller will have a strong spike at the fundamental frequency, but no significant higher frequency harmonics. The aerodynamic interaction of the counterrotating propeller causes the levels of the higher frequency harmonics to be significantly higher [17]. This explains why the Dash-8 spectra show significant harmonics at positions to the front of the plane, where there are contributions from each of the propellers.

In addition to the tones generated by the BPF and its harmonics, turbulent airflow over the propeller blades may create nonlinear noise characteristics [2]. Turbulent airflow causes quadrupole noise, which can be seen in the directivity plot shown in Fig. 4.4 of Section 4.4. The nonlinearity of this noise can generate tones that are not multiples of the BPF. These tones can be seen in the narrow-band

spectra shown in Appendix B, particularly at frequencies below the BPF.

The noise contribution at the BPF is also clearly visible in the 1/3 octave band spectra. To the sides of the aircraft, the 1/3 octave band levels at 80Hz and 160Hz are the loudest; to the front of the aircraft, high frequency noise (from higher harmonics) dominates the spectra. Unlike the idle engine spectra, there are no dips at any particular frequency range. Given the strong tonal noise components, it may be possible to control full-power engine noise with ANC.

The BPF of the Dash-8 is lower than that of the Beechcraft, which was found to be 112.5Hz [2]. The total noise levels for the Beechcraft with the engines at full-power, at a distance of 98m, ranged from 103 to 112dB (100 to 109dBA), while the Dash-8 noise ranged from 101 to 127dB (98 to 110dBA) at a distance of 40m. Although the Beechcraft noise was measured at a position of more than twice the distance away than that of the Dash-8, the total A-weighted noise levels were almost the same for both aircraft.

4.3.3 Half Power Engine Spectra (odd-numbered Figs. C.1 to C.20)

It is also of interest to understand how a single propeller behaves as a noise source; however, it was not possible to run one engine at full power with the other idling. Instead, noise recordings were made with the right engine running at 50% power and the left engine idle with the intention of isolating the spectrum from a single engine. This isolation can be performed by means of decibel subtraction, which will be discussed in Section 4.5.

The BPF of the propeller with the right engine at 50% power was found to be 69Hz. The spectra show a combination of the characteristics of the idle engine and full power engine spectra. Like the idle engine spectra, the dip at the 315Hz 1/3 octave band is visible at positions near the propellers. To the front of the aircraft, the harmonics are louder than the BPF, as was the case in the full-power spectra. The additional power in the right engine had the effect of leveling the

mid-frequency dip that was characteristic of the idle engine spectra at most of the measurement positions. It can thus be concluded that increasing the engine power not only causes a significant increase in lower frequency noise at the BPF, it also increases the high frequency noise towards the front of the aircraft. The presence of strong tonal noise components in the half-power engine noise spectra suggests that it may be possible to control the noise with ANC.

4.3.4 Effect of the Ground Reflection

The measurement positions were marked at 40m from the center of the aircraft, but the propellers themselves are located approximately 5.3m in front of, and 3.9m to the side of, the center point. The actual distance from the microphones to the closest propeller thus ranged from about 35 to 45m. Since the microphones were held at a height of approximately 1.4m, the path-length difference between the direct and reflected sound paths ranged from 0.1 to 0.2m. The frequencies at which destructive interference would have occurred are thus between 850 and 1700Hz. This may be the reason for the mid-frequency (800 to 1600Hz 1/3 octave bands) dips in the idle engine spectra. However, the ground reflection did not appear to have an effect on the half and full engine power spectra. Constructive interference may have occurred at frequencies between 1700 and 3400Hz, but these frequencies are outside of the region of interest for ANC.

4.4 Noise Directivity Patterns

The total unweighted and A-weighted noise levels calculated from the 1/3 octave band spectra were plotted on a polar plot to show the noise directivity of the Dash-8 for each of the measured engine power settings. The noise directivity for both of the engines at idle settings is shown in Fig. 4.3. The lowest levels were behind the left propeller, at about 80dBA; the loudest levels were to the front of the aircraft, at about 100dBA. Both the unweighted and A-weighted directivity

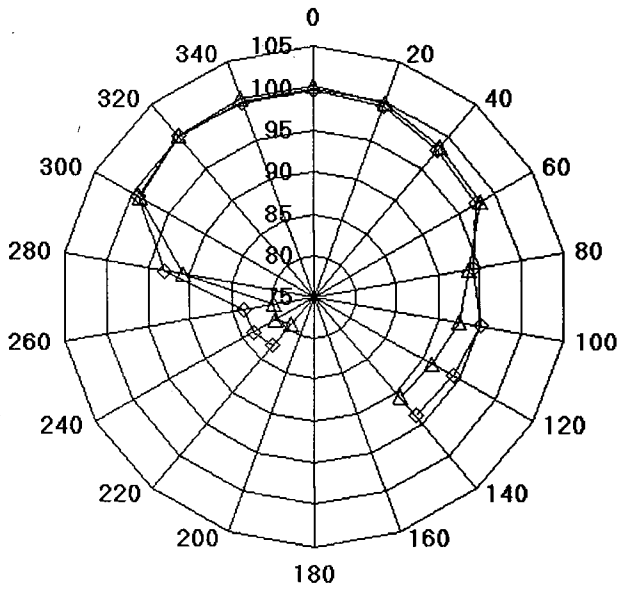

Figure 4.3: Noise directivity for both engines idle. ◇: total unweighted SPL, △: total A-weighted SPL.

patterns resemble that of a dipole source, with the strongest radiation to the front of the plane, and low levels to the sides, as expected for a fan-like source. However, unlike a perfect dipole source, the directivity – especially at the sides – is asymmetrical.

With both of the engines at full power, the directivity is as shown in Fig. 4.4. Clearly, it is very different from the idling results. The noise levels to the right of the aircraft are still louder than those to the left. The unweighted directivity pattern resembles the clover-leaf pattern characteristic of a quadrupole source, though it is asymmetrical, with the strongest lobe to the right of the aircraft at 127dB. The BPF in this case was found to be 80 Hz; the noise directivity at this frequency is shown in Fig. 4.5. The contribution at the BPF to the total noise levels to the sides of the aircraft is clearly seen. The directivity still has the shape of a clover-leaf, with a weak lobe to the front of the plane.

Germain [2] also plotted the full-power engine noise directivity of the Beechcraft. Unlike the Dash-8, the directivity pattern could not be identified clearly as a dipole

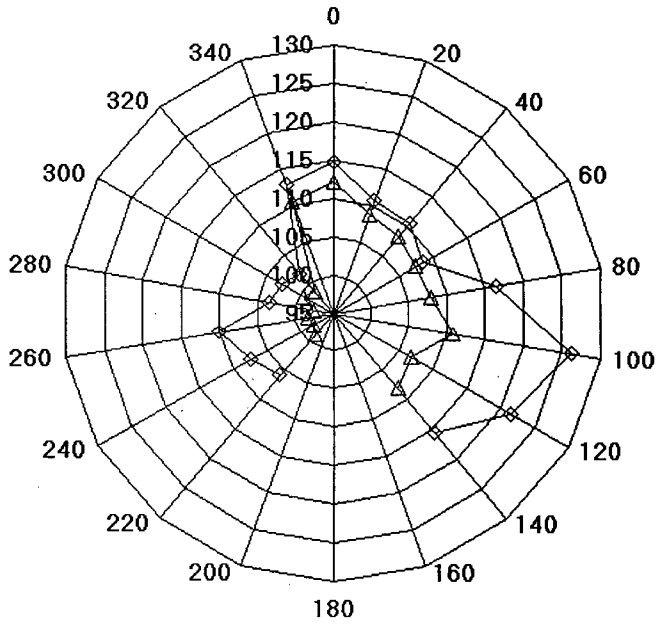

Figure 4.4: Noise directivity for both engines at full power. ◇: total unweighted SPL, △: total A-weighted SPL.

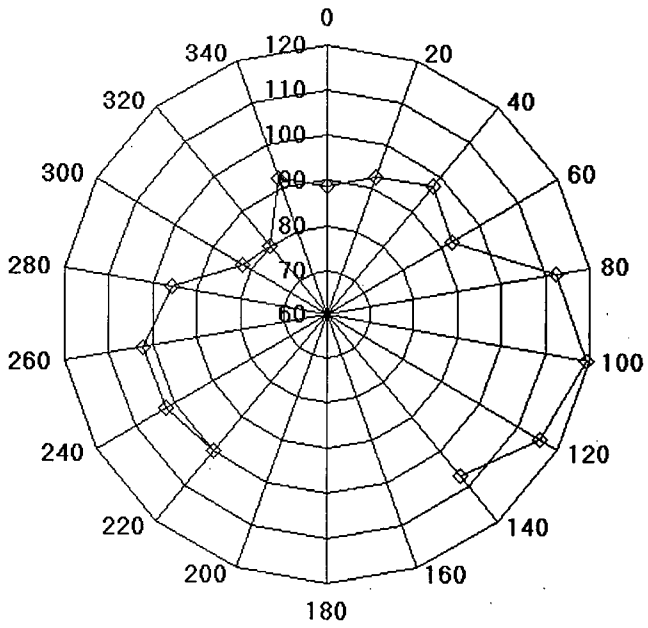

Figure 4.5: Total unweighted SPL at the blade-passing frequency (BPF) of 80 Hz for both engines at full power.

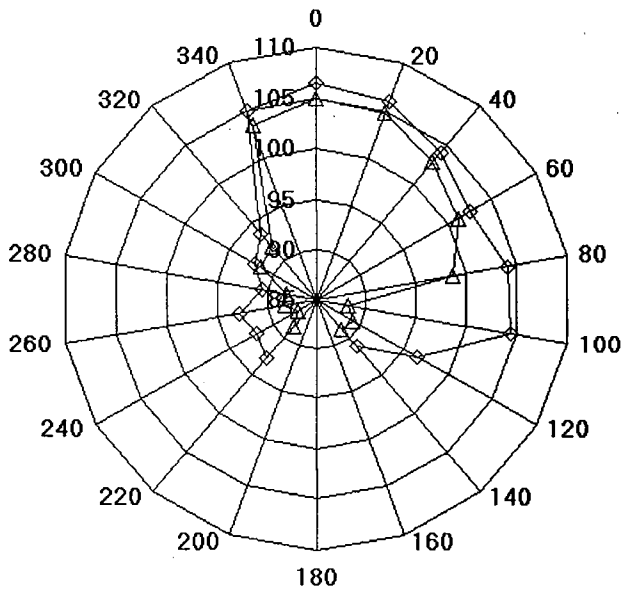

Figure 4.6: Noise directivity for right engine at 50% power, left engine idle. ◇: total unweighted SPL, △: total A-weighted SPL.

or quadrupole. The noise levels to the right of the aircraft were louder than to the left, as was the case with the Dash-8, but the strongest lobe was to the front of the right propeller (towards 30° and 60° as defined on the grids shown in Figs. 4.3 through 4.6) rather than to the right of the propeller.

The noise directivity of the aircraft with the left engine idling and the right engine at 50% power is shown in Fig. 4.6. The A-weighted directivity is roughly symmetrical about the 20° position, and both the A-weighted and unweighted patterns look like that of a dipole.

Judging from the different directivity patterns shown in Figs. 4.3 to 4.6, it appears that the position of the ANC system must be changed as appropriate to the engine settings during the run-up tests. It was shown in Chapter 3 that an ANC system is most effective when it is placed facing the lobe of strongest radiation from the primary source. The full-power and half-power engine noise spectra were shown to contain significant tonal noise in Section 4.3, making them potential candidates for ANC. In the full-power engine case, the ANC system would likely

be most effective if it was placed behind the right propeller (at 100°) and in the half-power engine case, the system should be placed in front of the aircraft (at 20°). Since the noise directivity of the Beechcraft at full engine power is different from the Dash-8, this suggests that the position of the ANC system must also be optimized differently for different aircraft.

4.5 Estimating Noise Levels in the Far Field

As well as measuring close to the aircraft, Germain [2] recorded the noise from the Beechcraft at a position in a community 3km north of the run-up site. This was done to quantify the noise levels heard by the residents of the community. It was of interest to use these results to estimate levels at 3km due to the Dash-8. However, in all but three of the far-field recordings measured by Germain, the ambient background noise was too excessive for the spectra to be usable. The headings for which data were obtained were 315°, 15° and 45°. The 315° and 15° headings correspond to the 240° and 300° headings used for the Dash-8, while the 45° heading is in between the 320° and 340° Dash-8 positions. Comparing the full-power directivities of the Beechcraft and the Dash-8, the 45° heading for the Beechcraft and the 340° for the Dash-8 both correspond to maxima, so the 340° Dash-8 heading was chosen for the estimation of noise in the far field.

The 1/3 octave band levels from the Beechcraft data in the far field were subtracted from the levels in the near field (73 m from the aircraft) to estimate the noise attenuation. These attenuation values were then subtracted from the corresponding Dash-8 levels; the results are shown in Fig. 4.7. Since the Dash-8 noise was measured at 40m from the aircraft, as opposed to 73m from the Beechcraft, the levels shown in Fig. 4.7 are likely higher than the actual levels, and should be considered as a "worst case scenario." The attenuation over the 3km distance resulted in levels no higher than 65dBA at any frequency; however, the unweighted levels in the 80Hz and 160Hz bands clearly show the contribution of the BPF and

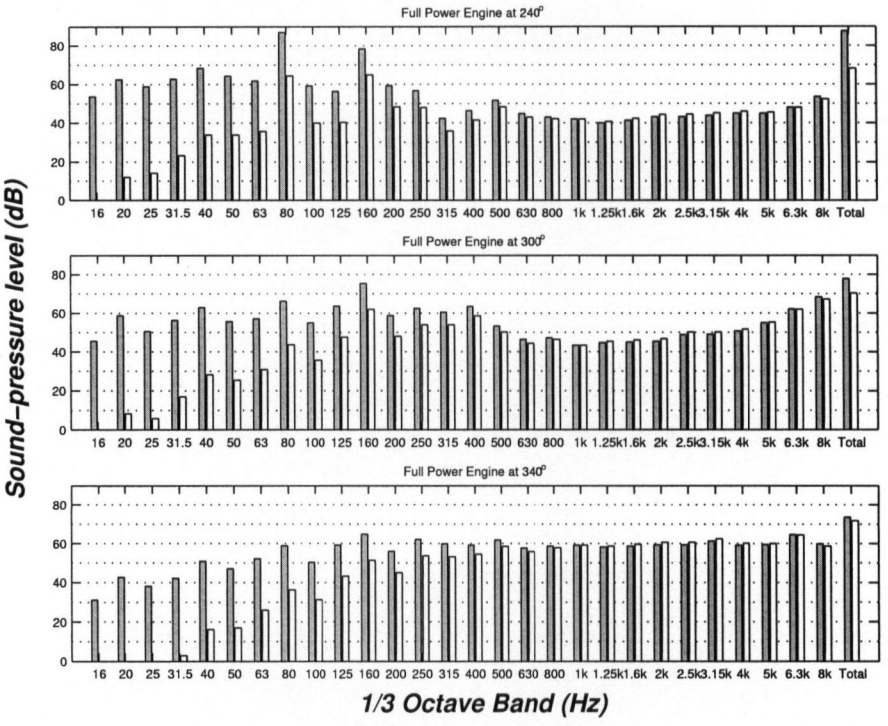

Figure 4.7: Estimated 1/3 octave band spectra at 3 km for positions 240°, 300° *and* 340°.

its first harmonic.

The total unweighted and A-weighted values for the Beechcraft and the Dash-8 are shown in Table 4.2 for comparison. The total unweighted noise level of the Dash-8 at 240° (315° for the Beechcraft) is 12dB higher than that of the Beechcraft, mainly due to the noise contribution at the BPF. The difference is less significant in the A-weighted levels, because the BPF of the Beechcraft is higher than the Dash-8, at 112.5Hz [21]. The A-weighting in the 80Hz band is 6.4dB lower than

Table 4.2: Total unweighted and A-weighted Beechcraft and (estimated) Dash-8 noise levels at a distance of 3km.

Heading (Beech/Dash-8)	Total Unweighted (dB)		Total A-weighted (dBA)	
	Beech	Dash-8	Beech	Dash-8
$315^0/240^0$	76	88	63	68
$15^0/300^0$	76	78	66	70
$45^0/340^0$	74	74	64	72

the 125Hz band, causing the BPF of the Dash-8 to give a smaller contribution to the total A-weighted level. For the other two headings, the unweighted values for the two aircraft were similar, while the A-weighted totals for the Dash-8 are higher than the Beechcraft. This suggests that the Dash-8 produces more high-frequency noise than the Beechcraft.

The estimated propagation of the Dash-8 noise into a community 3km to the north of the airport shows that the highest levels are caused by the BPF and its first harmonic. This confirms the need to use ANC to control these two frequencies.

4.6 Estimating the Noise Radiation of a Single Propeller

It is also of interest to understand how a single propeller acts as a noise source. It was not possible to run one engine at above idling power with the other engine turned off. Instead, noise recordings were made with the right engine at 50% power and the left engine idle, with the intention of removing the idling engine response through post-processing. To obtain an approximation of the spectra of a single engine operating at 50% power, the idling engine spectra were decibel-subtracted from the right engine 50% power/ left engine idling spectra. The results are shown in Appendix C.

For the most part, the decibel subtracted narrow-band spectra were virtually identical to the original spectra. This suggests that the idling engine noise is negligible compared to one engine running at 50% power, since the removal of the idling engine noise did not reduce the amplitude of the peaks at the BPF and its harmonics. These peaks dominate the spectra, although high levels at frequencies below the BPF (likely caused by turbulent airflow as discussed before) still exist.

The 1/3 octave band spectra show differences only at very low frequencies. For the positions to the left side of the plane (220° to 320°), the levels in the 1/3 octave bands up to 40Hz were up to 8dB lower than the levels that included the idling

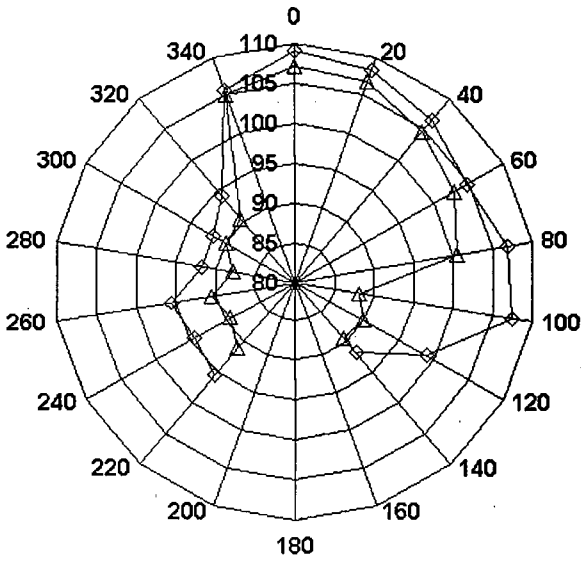

Figure 4.8: Decibel-subtracted noise directivity for right engine at 50% power. ◇: total unweighted SPL, △: total A-weighted SPL.

engine noise. Around the front of the aircraft (340° to 20°), the low frequency differences were less significant, ranging from 1 to 4dB. To the right of the aircraft, the spectra measured in front of the engine (40° to 80°) showed low frequency levels of only 1 to 2dB lower than before, while the differences behind the engine (100° to 140°) were up to 6dB. The idling engine noise does thus appear to make a small contribution to the noise of an engine operating at 50% power at frequencies below 45Hz, but it is not significant enough to change the total unweighted or A-weighted levels.

The directivity of the decibel subtracted data is shown in Fig. 4.8. This gives an approximation of the directivity of a single engine operating at 50% power. Given that the decibel subtracted noise spectra were similar to that of the right engine at 50% power with the left engine idling, it is not surprising that the directivity shown in Fig. 4.8 is almost identical that shown in Fig. 4.6. The radiation is approximately dipole, with the strongest headings towards 0° and 20°, and the weakest towards 300° and 140°.

Since the noise of both engines running at 50% power was not recorded, and it was not possible to record the noise of one engine operating at full power, the noise directivities for one propeller and two propellers cannot be compared directly. It can only be concluded that the directivity of two propeller engines operating at full power is approximately quadrupole, and that the directivity of a single propeller engine operating at 50% power is approximately dipole. The configuration of an ANC system thus must be changed accordingly for these two run-up conditions.

4.7 Conclusions

The Dash-8 run-up measurements made at the Vancouver International Airport in August 2002 were successful, as analysis of the recordings revealed important information about how the aircraft behaves as a noise source. It was shown that idling engine noise does not contain significant tonal components, which suggests that such noise cannot be controlled by ANC. It was also shown that the directivity changes as the engine power is increased. With one engine idling and the other at 50% power, the directivity is like that of a dipole; with both engines at full power, the directivity pattern resembles a quadrupole. It may thus be sufficient to model the noise of two full-power engines as a single quadrupole source. The Dash-8 was also found to have a noise directivity that is different from that of the Beechcraft. As such, the configuration of an ANC system must be modified for different run-up conditions, and for different aircraft.

Decibel subtraction of the idle engine response from the half engine power signal gave some insight into how a single propeller engine radiates noise. The radiation pattern was found to be approximately dipole. However, since the noise from both engines operating at 50% power was not recorded, it cannot be concluded that the dipole radiation is a result of the engine running at a lower speed, or a result of the removal of the response of the second engine. If the run-up measurements could be repeated, it would be of interest to record the noise for 1). one engine at 50% power and the other at full power and 2). both engines at 50% power to obtain

a better understanding of the directivity differences between a single engine and two engines.

Since half-power and full-power engine noise have significant tonal components, it may be possible to use ANC to reduce the noise. The fundamental frequencies to be controlled are 69Hz in the case of half engine power and 80Hz in the case of full engine power. It would also be of interest to control the 1st harmonic frequencies. From the conclusions reached in Chapter 3, the control system would have to be placed such that it is used to create quiet zones in the direction of the strongest primary radiation. At this point, it is not known how many control channels would be required to achieve sufficient noise attenuation. Even if it is not possible to implement ANC, since the noise directivity of the Dash-8 is now known, the aircraft could be oriented during the run-up tests such that the strongest radiation is directed away from noise-sensitive areas (i.e. residential communities).

The next chapter will discuss prediction models for outdoor sound propagation.

Chapter 5

Prediction Models for Outdoor Sound Propagation

5.1 Introduction

The ANC theory discussed in Chapter 2 is applicable to non-refracting, free-field and half-space conditions. In reality, the assumption of a free-field or a half-space is not valid in any real environment. Although a large open space with a hard ground surface (such as an aircraft engine run-up site at an airport) may be considered as a half-space for near-field sound propagation, environmental effects must be factored in when considering long-range sound propagation. Since the Vancouver International Airport Authority's main concern is reducing the noise that is radiated into communities several kilometers away from the airport, it is essential to study prediction models for long-range sound propagation.

In the interest of choosing a model that can be modified to predict the effectiveness of an ANC system on outdoor sound, a number of factors must be considered. Since the performance of an ANC system depends on the exact amplitude and phase relationships between the primary and secondary sources, the model must be able to predict the sound field accurately in amplitude and phase. In other words, the output of the model must be complex pressures rather than energy values. The model must also be able to account for the effects of finite ground impedance, wind-speed and temperature gradients and, ideally, turbulence and irregular terrain. This chapter provides an overview of some of the prediction models that have been developed for accurate outdoor sound propagation.

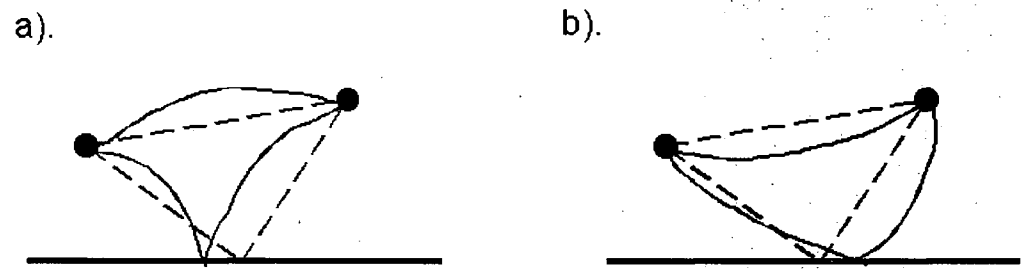

Figure 5.1: Direct ray and ray reflected by the ground surface, in a a). downward refracting atmosphere and an b). upward refracting atmosphere [21].

5.2 Ray-tracing model

A basic example of sound propagation in the case of a single reflection from the ground was shown in Section 1.4.1. In that analysis, the sound heard at the receiver is the sum of the sound pressures arriving by the direct and reflected paths. The sound waves traveling along the different propagation paths can be thought of as rays. In a non-refractive atmosphere, the ray paths are straight. In a refractive atmosphere, the rays are curved, as shown in Fig. 5.1 [21].

For large source-receiver distances, more than two sound rays must be considered. In a downwardly refracting atmosphere, the number of ground reflections is typically a few tens. The calculation of all ray paths from a source to a receiver is called ray-tracing [21]. The sound pressure at the receiver is the combination of the sound from the direct path, and all of the reflected paths. One problem that arises in this geometrical approach in the case of a refractive atmosphere is the formation of caustics. Refracted sound rays focus at certain points in the atmosphere, in the same way that light rays that are refracted by a lens converge at focal points [21]. Geometrical acoustics predicts that the sound pressure at these focal points is infinite; hence, any set of focal points is called a caustic. In two dimensions, a caustic is a curve on which one side is illuminated by sound waves,

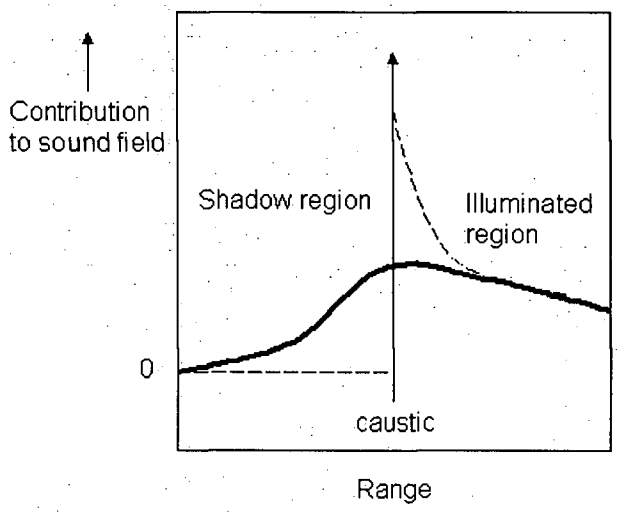

Figure 5.2: Schematic illustration of the sound pressure contribution of two sound rays focusing at a caustic. The dashed line represents the geometical acoustics solution, which has a discontinuity at the caustic. The solid line represents the real, continuous solution [21].

and the other side is shadowed.

Ludwig and Kravstov (cited in [21]) developed a ray model that accounts for the effects of caustics. In this two-dimensional model, the atmosphere is considered to be non-moving, and wind effects are modeled by using a smooth, vertical effective sound speed profile. The sound field at the receiver is the sum of the illuminated field (geometrical acoustics solution), p_{illum}, and the caustic diffraction field, p_{shadow}. The two regions are shown in Fig. 5.2. The contribution of the caustic diffraction field to the p_{shadow} term is discontinuous at the caustic; it has a finite value on the shadow side, and is zero on the illuminated side. However, since p_{illum} has the opposite discontinuity at the caustic, the total sound field is continuous. In three-dimensional space, the caustic points lie on a set of surfaces, called caustic surfaces. The intersection of these surfaces with the vertical plane on which both the source and receiver lie are called the caustic curves [21].

Ray-tracing models are limited because of long computational times and their inaccuracy, particularly at low frequencies. Since the implementation of ANC requires that the model be accurate in amplitude and phase at low frequencies, a

ray-tracing model is not appropriate for this research.

5.3 Fast-field program

The Fast-field Program (FFP) is a technique that was developed for underwater acoustics, and later adapted to atmospheric acoustics [22]. The FFP calculates a solution to an approximation of the wave equation in the frequency domain for a monopole source above an absorbing or rigid surface. The atmosphere can be horizontally stratified to model atmospheric refraction. The sound field is usually predicted in two dimensions, in a vertical plane through the source and the receiver. The model thus assumes azimuthal symmetry; this is known as the axisymmetric approximation. The axisymmetric approximation is valid in many practical situations, because wind and temperature variations with azimuthal angle are small compared to variations with height [21].

The FFP method uses a Fourier transform to transform the wave equation from the horizontal spatial domain to the horizontal wave-number domain. The transformed wave equation is solved numerically, then changed back to the spatial domain with the inverse Fourier transform. The spatial solution is thus an inverse Fourier integral over horizontal wave numbers.

It follows from the equations of mass conservation and momentum conservation in a fluid that the equation for sound waves is

$$\nabla^2 p - \frac{1}{c^2}\frac{\partial^2 p}{\partial t^2} = 0 \tag{5.1}$$

where p is the complex sound pressure and c is the speed of sound. For harmonic sound waves radiating from a monopole source, Eq. 5.1 can be expressed as

$$\frac{1}{r}\frac{\partial^2}{\partial r^2}(rp_c) + k^2 p_c = 0. \tag{5.2}$$

The solution is

$$p_c = S\frac{\exp(ikr)}{r} \tag{5.3}$$

where S is a constant. Since the field given by Eq. 5.1 diverges for $r \to 0$, a term is included on the right-hand side:

$$\nabla^2 p_c + k^2 p_c = -4\pi S\delta(\mathbf{r} - \mathbf{r}_s), \tag{5.4}$$

where $\mathbf{r}_s = (x_s, y_s, z_s)$ is the source position. In the FFP method, the sound pressure p is calculated in the wave-number domain. Let P denote the Fourier transform of p. The two-dimensional inhomogeneous Helmholtz equation in cylindrical coordinates can be written as

$$k^2\frac{\partial}{\partial z}\left(\frac{1}{k^2}\frac{\partial P}{\partial z}\right) + k_z^2 P = -\sqrt{2\pi k_r}\,\delta(z - z_s). \tag{5.5}$$

Eq. 5.4 is the basic equation of the Fast Field Program (FFP) method.

The FFP method can predict the sound field at a receiver point in the presence of a vertical wind-speed gradient. The wave number k in Eq. 5.5 is defined as

$$k = \frac{\omega}{c(z)} - \frac{k_x u_{av}}{c(z)} - \frac{k_y v_{av}}{c(z)} \tag{5.6}$$

where u_{av} and v_{av} are the x and y components of the wind velocity [21]. k is a function of the height z such that the atmosphere is represented by a vertical sound-speed profile. The profile is approximated by dividing the atmosphere into N horizontal layers such that k is constant within each layer. The heights at the interfaces between the layers are labelled z_j for $j = 1, 2, ..., N$, and the source height z_s coincides with interface z_m such that $z_s = z_m$. Since k is constant within each layer, Eq. 5.5 becomes

$$\frac{\partial^2 P}{\partial z^2} + K_z^2 P = -4\pi\delta(z - z_s) \tag{5.7}$$

for which the solution in layer j is

$$P_j = A_j \exp(ik_{zj}) + B_j \exp(-ik_{zj}z) \tag{5.8}$$

for $z_j \leq z \leq z_{j+1}$, and A_j and B_j are constants. In the region below the ground surface ($z \leq 0$), there is no wave travelling upward, so $A_0 = 0$. In the top layer ($z_{N-1} \leq z \leq z_N$), it is assumed that there is only an upward travelling wave (i.e. sound is absorbed above the top layer and not refracted down towards the receiver), so $B_{N-1} = 0$. The constants A_j and B_j can be calculated from the boundary conditions, which are:

- continuity of acoustic pressure at all interfaces;
- continuity of normal sound velocity at all interfaces, except at $z_s = z_m$.

The P_j can be found in each successive layer by iteration. Solving Eq. 5.5, it can be shown that

$$P_j(z + \Delta z) = \cos(k_{zj}\Delta z)P_j(z) + k_{zj}^{-1} \sin(k_{zj}\Delta z)P_j'(z). \tag{5.9}$$

and

$$P_j'(z + \Delta z) = -k_{zj} \sin(k_{zj}\Delta z)P_j(z) + \cos(k_{zj}\Delta z)P_j'(z). \tag{5.10}$$

The inverse Fourier transform on P_j values can be calculated to obtain the sound pressure at the receiver. This is given by

$$q_c(r, z) = \frac{1}{\pi\sqrt{2}} \int_{-\infty}^{\infty} [\exp(ik_r r) + \exp(-ik_r r)]Q(K_r, z)dk_r, \tag{5.11}$$

where $q_c = p/r$ and Q is the Fourier transform of q_c. Further details on the FFP method can be found in reference [21].

The computational time required to solve Eq. 5.11 depends on the number of layers used. Therefore, a rapidly varying wind-speed profile will be more demanding computationally than a slowly varying profile. Because the solution is calculated in the horizontal wave-number domain, the FFP method can only be

used for a layered atmosphere above homogeneous ground. Range-dependent effects, such as irregular terrain and turbulence, cannot be modeled.

5.4 Parabolic equation

The parabolic equation (PE) method is based on an approximation to the wave equation that puts it into the form of a parabolic partial differential equation (PDE). A PDE of the form

$$Au_{xx} + 2Bu_{xy} + Cu_{yy} + DU_x + Eu_y + F = 0 \tag{5.12}$$

is defined to be parabolic if

$$\mathbf{Z} = \begin{bmatrix} A & B \\ B & C \end{bmatrix}, \tag{5.13}$$

satisfies $\det(Z) = 0$. The wave equation itself is a hyperbolic PDE because it satisfies $\det(Z) < 0$. The PE method can be used to predict the sound field of a monopole source above a ground surface in the presence of a refractive atmosphere. Unlike the FFP method, the PE method does not require that the atmosphere be divided into layers, and has the ability to model an inhomogeneous ground surface [21].

The PE method calculates the sound field in a region that is limited by a maximum elevation angle, γ_{max}, as shown in Fig. 5.3. Sound waves that leave the source at angles greater than γ_{max} are neglected in the calculation of the sound field at the receiver. The value of γ_{max} depends on the implementation of the PE method. Two approaches to the PE method will be discussed: the Crank-Nicholson method and the Green's function method. An overview of how turbulence and irregular terrain can be incorporated into the PE model will follow.

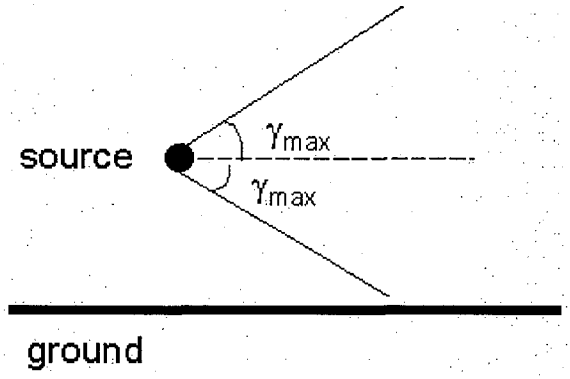

Figure 5.3: Region for which the PE method is valid. The boundaries of the region are defined by the maximum elevation angle γ_{max} [21].

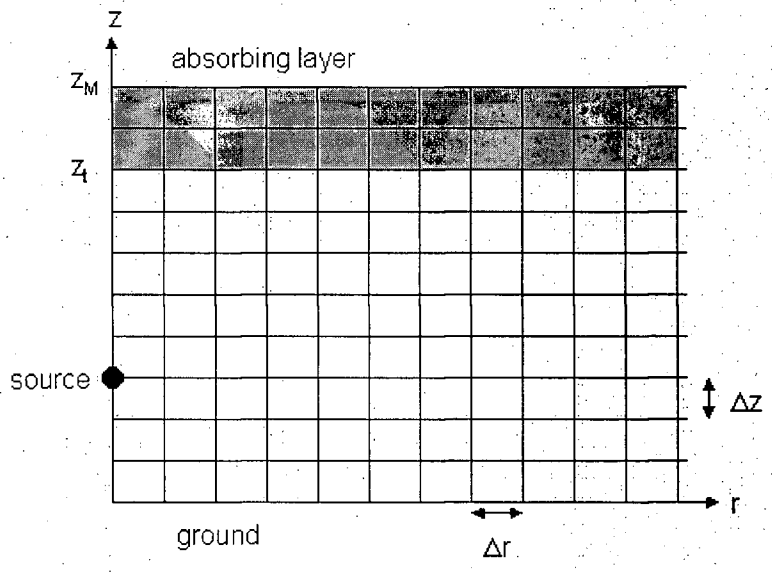

Figure 5.4: Grid in the rz plane for the PE method. The ground surface is located at $z = 0$ and the absorbing layer lies at the top in the shaded region $z_t \leq z \leq z_M$ [21].

5.4.1 Crank-Nicholson Parabolic Equation

The Crank-Nicholson PE (CNPE) method was developed by Gilbert and White [23]. In the CNPE method, an axisymmetric approximation is used to reduce a three-dimensional problem to two dimensions [6]. Using the standard definition of cylindrical coordinates, the variation of the sound field with the azimuthal angle ϕ is neglected. The two-dimensional Helmholtz equation is then given by

$$\frac{\partial^2 q}{\partial r^2} + \frac{\partial^2 q}{\partial z^2} + k^2 q = 0 \tag{5.14}$$

where $q = p\sqrt{r}$. The field $q(r, z)$ is calculated on a grid in the rz plane, starting at the source, as shown in Fig. 5.4. The sound field at a given point is determined iteratively from the sound field at the previous grid location. In order to begin the calculations, the sound field at the starting point, $r = 0$ must be determined. The exact equation for the field of a monopole source in an unbounded, non-refracting atmosphere is

$$q(r, z) = \frac{\exp(ikR)}{R}\sqrt{r} \tag{5.15}$$

where R is the radial distance from the source. However, this equation cannot be used as the starting field for the PE method because:

- $q(r, z) \to \infty$ for $R \to 0$;
- the sound waves produced may have elevation angles that are larger than the interval within which the PE method is valid [21].

The expression for the starting field used in the CNPE method is given by

$$q(0, z) = q_o(z - z_s) + Cq_o(z + z_s), \tag{5.16}$$

where z_s is the source height, C is the reflection coefficient and $q_o(z)$ is the starting field for the source in an unbounded atmosphere. This is given by

$$q_o(z) = \sqrt{ik_a}\exp(-\frac{1}{2}k_a^2 z^2), \tag{5.17}$$

for the narrow-angle PE method ($\gamma < 10°$), and

$$q_o(z) = \sqrt{ik_a}(1.3717 - 0.3701k_a^2z^2)\exp\left(-\frac{k_a^2z^2}{3}\right), \tag{5.18}$$

for the wide-angle PE ($10° < \gamma < 30°$). k_a is the reference wave number, usually taken to be the wave number at the ground.

The starting function, $q(0,z)$, is extrapolated in the positive r direction to obtain the field at all of the grid points. Accurate results can only be obtained if the horizontal and vertical grid spacing, Δr and Δz, are less than $\frac{\lambda}{10}$ [21]. The grid is bounded at the top by an artificial absorptive layer to eliminate reflections, and at the bottom by the boundary conditions imposed by the ground.

Going back to the Helmholtz equation, the solution to Eq. 5.12 is

$$q(r,z) = \psi(r,z)\exp(ik_ar). \tag{5.19}$$

Substituting Eq. 5.17 into Eq. 5.12 gives

$$\frac{\partial^2\psi}{\partial r^2} + 2ik_a\frac{\partial\psi}{\partial r} + \frac{\partial^2\psi}{\partial z^2} + (k^2 - k_a^2)\psi = 0. \tag{5.20}$$

Assuming that ψ varies slowly with r, Eq. 5.18 becomes

$$2ik_a\frac{\partial\psi}{\partial r} + \frac{\partial^2\psi}{\partial z^2} + (k^2 - k_a^2)\psi = 0, \tag{5.21}$$

which is called the narrow-angle parabolic equation [21]. Eq. 5.19 is valid for elevation angles of up to about 10°. It can be shown that a wide-angle parabolic equation that is valid for elevation angles of $10° < \gamma < 30°$ is given by [21]

$$\left(1 + \frac{1}{4}s\right)\frac{\partial\psi}{\partial r} = \frac{1}{2}ik_as\psi, \tag{5.22}$$

where

$$s = \frac{k^2(z) - k_a^2}{k_a^2} + \frac{1}{k_a^2}\frac{\partial^2}{\partial z^2}. \tag{5.23}$$

The solution for ψ in both cases can be obtained by approximating the derivatives with finite differences. These solutions are presented in reference [21].

5.4.2 Green's Function Parabolic Equation

The Green's function parabolic method (GFPE) was developed by Gilbert and Di [24]. The GFPE calculates the sound field of a point source above a finite-impedance ground as a sum of three terms: a direct wave, a specularly reflected wave and a surface wave. It is more computationally efficient than the CNPE, because it is possible to use range steps, Δr, that are several wavelengths long.

Like the CNPE, the theoretical formulation of the GFPE begins with the Helmholtz equation. Applying a Fourier transform such that $q \rightarrow Q$ and $z \rightarrow k_z$, Eq. 5.12 becomes

$$\frac{\partial^2 Q}{\partial r^2} + (k^2 - k_z^2)Q = 0. \tag{5.24}$$

Eq. 5.22 can be written as

$$\left(\frac{\partial}{\partial r} - i\sqrt{k^2 - k_z^2}\right)\left(\frac{\partial}{\partial r} + i\sqrt{k^2 - k_z^2}\right)Q = 0, \tag{5.25}$$

so the two bracketed terms can be solved separately. The left term gives rise to a solution that is a wave travelling in the positive r direction, while the right term has a solution that is a wave travelling in the negative r direction. The solution can be restricted to sound propagation in the positive r direction, yielding the result

$$Q(r + \Delta r, k_z) = Q(r, k_z)\exp(i\Delta r\sqrt{k^2 - k_z^2}). \tag{5.26}$$

The sound field q is then given by the inverse Fourier transform

$$q(r + \Delta r, z) = \frac{1}{2\pi}\int_{-\infty}^{\infty}\exp(ik_z z)\exp(i\Delta r\sqrt{k^2 - k_z^2})Q(r, k_z)dk_z. \tag{5.27}$$

Eq. 5.25 is valid for an unbounded, non-refracting atmosphere [21].

The equations for a refractive atmosphere can be derived using the spectral theorem of functional analysis [21, 23]. It can be shown that

$$q(r+\Delta r, z) = \exp(i\Delta r H_2^{1/2}) q(r, z), \tag{5.28}$$

is the solution to the one-way wave equation, $\partial_r q = iH_2^{1/2} q$, where $H_2 = \partial_z^2 + k^2$. To obtain an explicit form of the exponential operator in Eq. 5.26, H_2 can be expressed in a spectral representation for a general function of an operator:

$$F(H_2) = \frac{1}{2\pi i} \int_C \frac{F(\tau)}{\tau - H_2} d\tau, \tag{5.29}$$

and Eq. 5.26 can be expressed as

$$q(r+\Delta r, z) = \frac{1}{2\pi i} \int_C \frac{\exp(i\Delta r)\tau^{1/2})}{\tau - H_2} q(r, z) d\tau. \tag{5.30}$$

If $\tau = k^2$, it is noted that $(k^2 - H_2)^{-1}$ is the Green's operator, $G(k)$, that satisfies

$$(Q - k^2) G(k) = -I, \tag{5.31}$$

where I is the unit operator [24]. The exponential operator can then be expressed as

$$\exp(i\Delta r\sqrt{H_2}) = \frac{1}{\pi i} \int_C G(k) \exp(ik\Delta r) k dk, \tag{5.32}$$

and Eq. 5.28 becomes

$$q(r+\Delta r, z) = \frac{1}{4\pi^2 i} \int_{-\infty}^{\infty} \exp(ik\Delta r) k dk \int_0^{\infty} G(k, z', z) q(r, z') dz'. \tag{5.33}$$

It follows that the basic equations of the GFPE for a refracting atmosphere are

$$\psi(r+\Delta r, z) = \exp\left(i\Delta r \frac{\delta k^2(z)}{2k_a}\right) \{\frac{1}{2\pi} \int_{-\infty}^{\infty} [\Psi(r, k_z) + R(k_z)\Psi(r, -k_z)]$$

$$\times \exp\left(i\Delta r\left[\sqrt{k_a^2 - k_z^2} - k_a\right]\right)\exp(ik_z z)dk_z$$
$$+2i\beta\Psi(r,\beta)\exp\left(i\Delta r\left[\sqrt{k_a^2 - \beta^2} - k_a\right]\right)\exp(-i\beta z)\} \quad (5.34)$$

where

$$\Psi(r,k_z) = \int_0^\infty \exp(-ik_z z')\psi(r,z')dz' \quad (5.35)$$

and $\psi(r,z) = \exp(-ik_a r)q(r,z)$ (recall that $q = p\sqrt{(r)}$) [21].

The GFPE method uses a Gaussian starting field given by [24]

$$\Psi(r=0,z) = \left\{\exp\left[-\left(\frac{z-z_s}{\sigma}\right)^2\right] + \frac{Z_g - 1}{Z+1}\exp\left[-\left(\frac{z+z_s}{\sigma}\right)^2\right]\right\} \times (\sqrt{\sigma})^{-1}. \quad (5.36)$$

Like the CNPE method, the starting field is calculated at $r = 0$ up to the top of the grid shown in Fig. 5.4. The solution is then calculated vertically at each successive range step.

The GFPE method has the advantage over the CNPE that it is computationally efficient. It has been shown that the results are in agreement with those calculated with the FFP, and that the computation time is approximately two orders of magnitude faster than the CNPE [24]. The GFPE can model range-dependent effects that cannot be implemented with the FFP. It has been shown that atmospheric turbulence and irregular terrain can be modeled in the GFPE [21]. The GFPE would thus likely be appropriate for prediction of ANC of outdoor sound, because of its ability to model many types of atmospheric and ground conditions, and because of its computational efficiency.

The next chapter describes ANC simulations on outdoor sound that were done using the GFPE method.

Chapter 6

Computer Simulations of Active Noise Control under Realistic Outdoor Conditions

6.1 Introduction

After performing a literature search, it was found that the prediction of the effectiveness of active control on outdoor sound in the presence of realistic ground and meteorological conditions has not been investigated in any published literature. As was seen in the previous chapter, prediction of outdoor sound propagation is a difficult problem. This is especially true for long-range propagation, because a number of complex phenomena must be taken into account. These phenomena include atmospheric refraction, complex ground impedance, irregular terrain and turbulence. The addition of active control into a prediction model further complicates the problem, because it requires accurate amplitude and phase prediction of multiple sources.

The Green's function parabolic equation (GFPE) method has been applied extensively for prediction of the sound field of a monopole source over long ranges, in the presence of a refractive, turbulent atmosphere over a finite-impedance ground. For the purpose of studying the effect of atmospheric and ground conditions on the performance of an active-noise-control system, it was of interest to modify the GFPE code to implement control sources. This chapter discusses some preliminary results of active control under typical meteorological conditions using the GFPE. A specific objective is to investigate whether realistic meteorological conditions affect the effectiveness of ANC.

Table 6.1: Parameter values used in Attenborough's four parameter model for ground impedance.

Parameter	Value
Flow resistivity (σ)	366000 Pa s m^2
Porosity (Ω)	0.27
Pore shape factor (s_p)	0.25
Grain shape factor (n')	0.5

6.2 Validation of the GFPE Model

A GFPE code written in Fortran was obtained from Dr. Xiao Di of the Applied Research Laboratory at Pennsylvania State University. This implementation of the model allows for one-dimensional prediction of the sound field of a monopole source, calculated at some receiver height, or two-dimensional prediction in a vertical plane. Atmospheric refraction is calculated from a vertical sound-speed gradient that is defined by the user, and the effects of turbulence can be included. This section presents the results of validation tests performed with the GFPE model.

6.2.1 Benchmark Case Results

To validate the sound-field amplitude calculations of the GFPE model, predictions for the four benchmark cases defined by Attenborough *et al.* [22] were performed. The ground surface was a 2m-deep, homogeneous and isotropic layer of porous sand above a nonporous substrate, with parameters as listed in Table 6.1. Attenborough's four-parameter model was used to calculate the complex ground impedances [22]. The four benchmark cases represent different types of atmospheres. Case 1 represents a non-refractive atmosphere, with a constant sound speed throughout. Case 2 is a downwardly refractive atmosphere with a strong positive sound-speed gradient of $0.1s^{-1}$. An upwardly refractive atmosphere is represented by Case 3, which uses a strong negative sound-speed gradient of $-0.1s^{-1}$. Case 4 represents a composite profile, which has a positive sound-speed gradient of $0.1s^{-1}$ up to a height of 100 m, a negative sound-speed gradient of $-0.1s^{-1}$ from

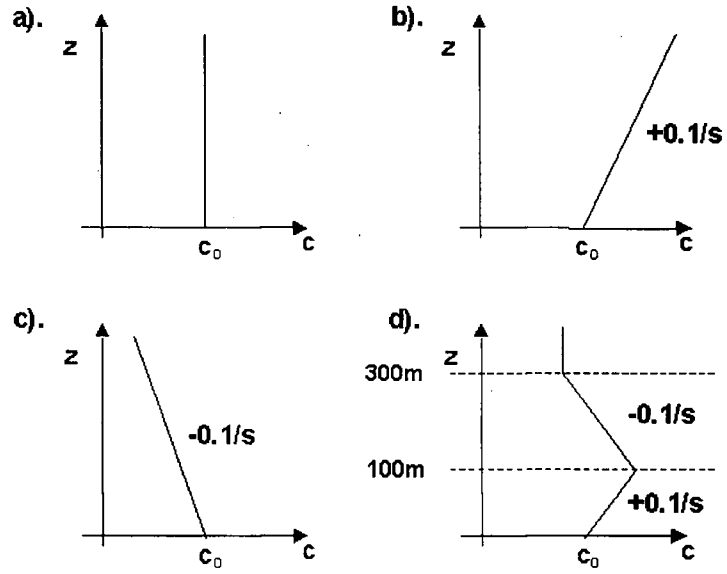

Figure 6.1: Sound-speed profiles for a). Case 1, b). Case 2, c). Case 3 and d). Case 4.

100 m to 300 m above the ground, and which is non-refractive above a height of 300 m. The sound-speed profiles are illustrated in Fig. 6.1.

Di's GFPE model was validated by repeating the benchmark-case simulations at the three frequencies (10, 100 and 1000Hz) used in [22]. As mentioned in Chapter 5, the GFPE calculates the solution on a grid in the vertical plane (see Fig. 5.4). It has been shown that the accuracy of the sound pressure levels predicted by the GFPE depends on the grid spacing used in the calculation of the solution [25]. The vertical grid spacing and range step (horizontal grid spacing) are defined by the user in an input file. In order to determine a grid spacing that would produce accurate results, different grid spacings were tried at each of the three frequencies until the results matched those shown in reference [22]. It was found that using a range step of $dr = 10$m gave the best results for all three frequencies, although the results changed little for larger grid spacings. The results were much more sensitive to the vertical grid spacing dz. The best results were obtained using $dz = 4$m for 10Hz, $dz = 0.4$m for 100Hz and $dz = 0.12$m for 1000Hz. The GFPE was then used to predict the transmission loss at 80Hz and 160Hz, corresponding to the funda-

mental and 1st harmonics of the Dash-8 noise, respectively. The transmission loss is defined as:

$$TL = -20\log\left(\frac{\text{total acoustic pressure at a field point}}{\text{acoustic pressure of the direct sound field at 1m}}\right) \quad (6.1)$$

The complex ground impedances, calculated using the parameter values listed in Table 6.1, were 14.66+13.63i at 80Hz and 10.74+9.29i at 160Hz. The predictions were run for a source height of 5m and a receiver height of 1m over a horizontal range of 10km, using a horizontal range step of 10m for both frequencies. Vertical grid spacings of 0.4m at 80Hz and 0.38m at 160Hz were used.

Fig. 6.2 shows the 80Hz transmission loss for the four benchmark cases. The result for no atmospheric refraction over reflective ground is also shown as a reference. In this case, the sound decay is almost completely due to spherical spreading (atmospheric absorption has very little effect at this frequency), and amounts to 20dB of decay per decade of distance. The finite-impedance ground used in the benchmark cases absorbs some of the sound energy and causes the signal to decay much more quickly. This can be seen in the results for Case 1, as the signal travels only about 2.5km before it has decayed by 80dB. The strong downwind conditions of Case 2 cause large destructive-interference dips to occur between 1km and 2km; beyond 2km, there are rapid fluctuations of up to 5dB. The average levels in the far field are only a few dB lower than in the reference case. This implies that the presence of a strong downwind counters the absorptive effect of a soft-ground surface. In Case 3, the presence of a strong upwind cause the sound waves to be refracted above the receiver, resulting in the signal decaying by 80dB over a distance of 1km. For the composite profile (Case 4), the curve is almost identical to that of Case 2 up to about 1.5km. Beyond 1.5km, the presence of strong upwind conditions above a height of 100m counteracts the downwind conditions and causes the signal to decay more rapidly than in Case 2.

The results for 160Hz are shown in Fig. 6.3. In the non-refractive case (Case 1), the signal decays by 80dB over a distance of 1km. The upwind conditions of

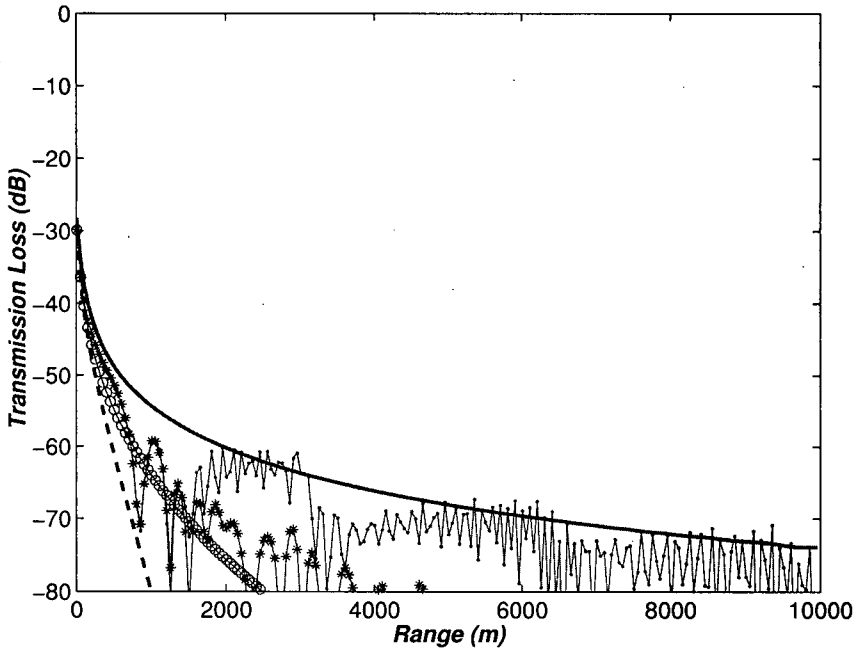

Figure 6.2: 80Hz transmission loss for the 4 benchmark cases. The non-refractive case over reflective ground is also shown for reference. — = no refraction, reflective ground, -o- = Case 1, — · — = Case 2, - - = Case 3, -∗- = Case 4.

Case 3 cause an 80dB attenuation to occur over only a slightly shorter distance of 800m. At this frequency, absorption by the ground is a more significant factor than upward refraction in terms of sound-field attenuation. The results for Case 2 and Case 4 are similar up to about 5km. The sound-speed profile above a height of 100m thus does not have as much of an effect on the sound field near the ground as it did at 80Hz.

It is evident that the ground surface and atmospheric refraction have a significant effect on sound propagation at low frequencies. It is thus essential to study the effect of these factors on the performance of an active-control system.

6.2.2 Single-channel Control Validation

The GFPE code was modified to include a single active-control channel using equations described by Guo and Pan [16]. The model was validated by comparing the results obtained using the GFPE model with Guo's and Pan's image-phase

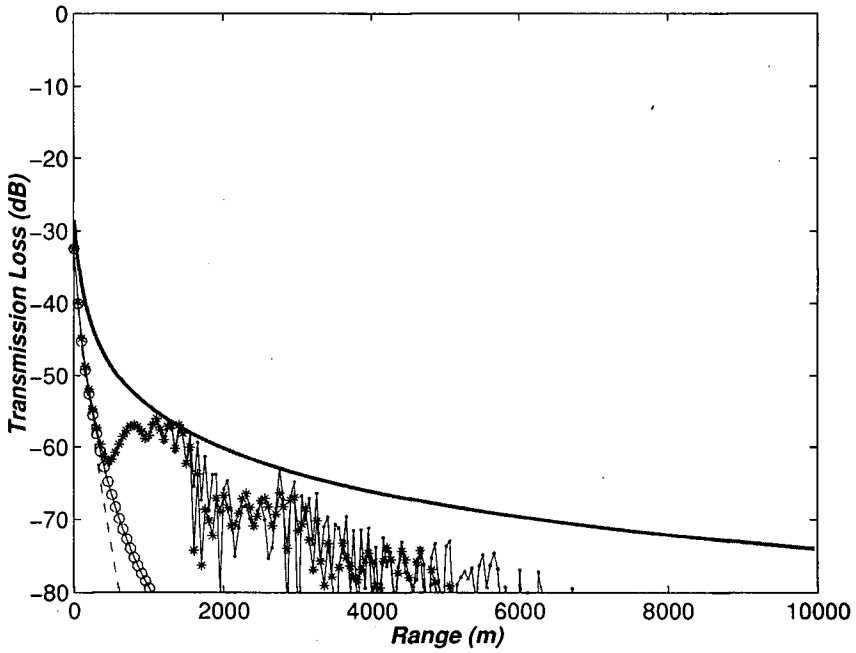

Figure 6.3: 160Hz transmission loss for the 4 benchmark cases. The non-refractive case over reflective ground is also shown for reference. — = no refraction, reflective ground, -o- = Case 1, – · – = Case 2, - - = Case 3, -- = Case 4.*

model for a non-refractive atmosphere above a reflective plane, which was discussed in Chapter 2 [16]. Single-channel ANC predictions for a monopole primary source were done up to a horizontal distance of 10km, using source and receiver heights of 4.5m (the height of the center of the Dash-8 propellers). For all of the predictions, the control source and error sensor were positioned in a line at the height of the primary source.

The results calculated using the GFPE method may not be accurate in the near field because the GFPE uses a Gaussian starting field. Because the Gaussian does not represent an exact starting field, the GFPE predictions are not accurate at distances of less than a few wavelengths. The secondary source must be placed farther than a few wavelengths away from the primary source for the complex pressures to be added correctly.

It was found that the ANC predictions using the GFPE method were sensitive

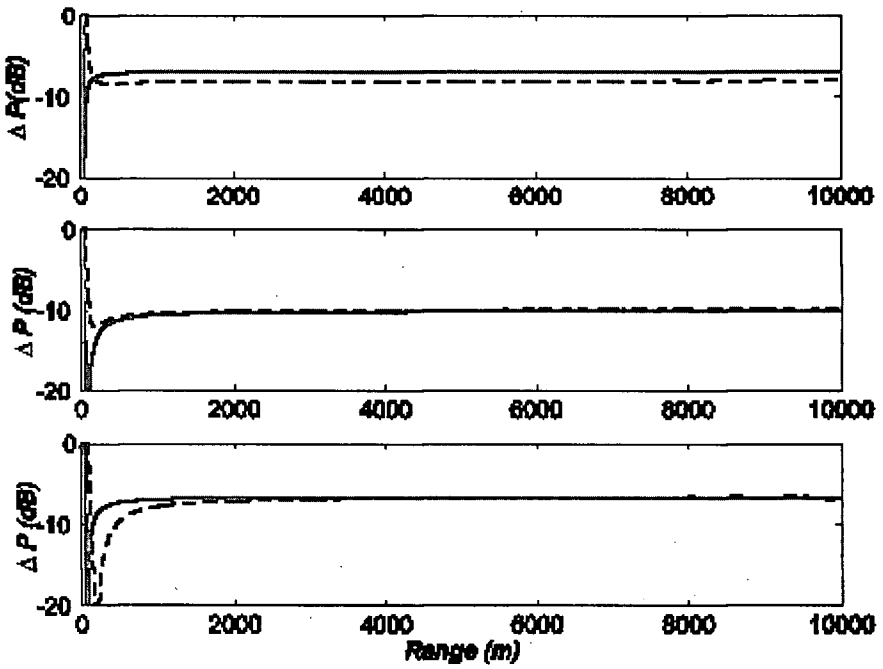

Figure 6.4: Single-channel ANC results for Guo's and Pan's image-source model (–) and the GFPE model (- -) for a monopole primary source at 80Hz. Top: $r_{ps} = r_{se} = 30m$. Middle: $r_{ps} = 30m$, $r_{se} = 60m$. Bottom: $r_{ps} = r_{se} = 40m$.

to the reference sound speed. At 80Hz, the results agreed with the image-source predictions when a reference sound speed (sound speed at the ground) of 343m/s was used. When a reference speed of 340m/s was used, the control results differed by as much as 10dB, although the amplitude predictions of the primary source and the secondary source separately did not change. The phase predictions of the GFPE thus appear to be quite sensitive at low frequencies. At higher frequencies, the value of the reference sound speed was less significant. For the results shown here for 160Hz, a reference sound speed of 340m/s was used.

Sample validation results for 80Hz are shown in Fig. 6.4 for $r_{ps} = r_{se} = 10$m, $r_{ps} = 30$m, $r_{se} = 30$m and $r_{ps} = r_{se} = 40$m. The GFPE results do not match the predictions made by the image-phase model in the near field. The phase prediction of the GFPE is less exact than the image-phase model, but it is expected that the solutions will converge in the far field. It is shown in Fig. 6.5 that this is indeed

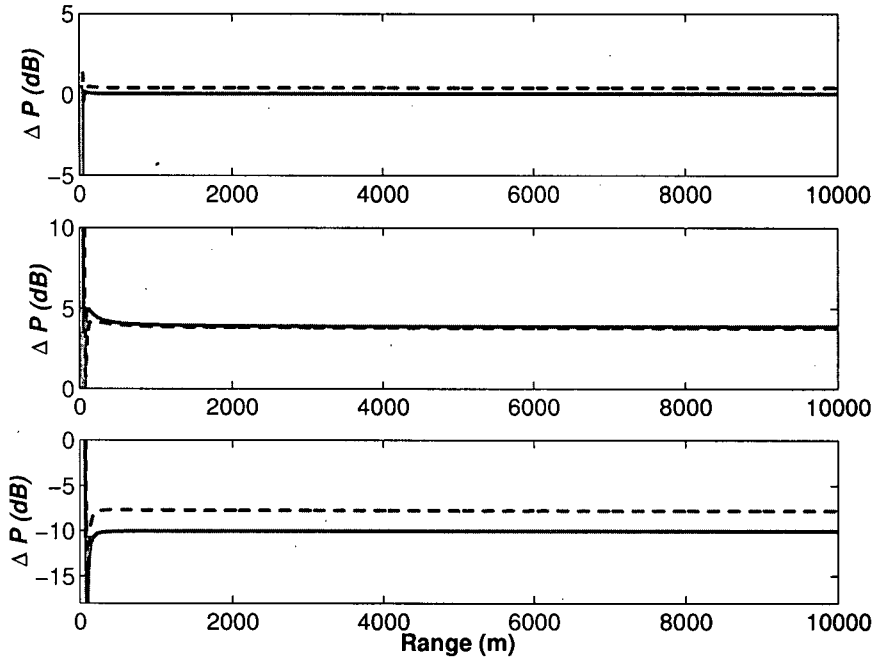

Figure 6.5: Single-channel ANC results for Guo's and Pan's image-source model (-) and the GFPE model (- -) for a monopole primary source at 160Hz. Top: $r_{ps} = r_{se} = 20m$. Middle: $r_{ps} = r_{se} = 30m$. Bottom: $r_{ps} = 30m, r_{se} = 60m$.

the case, except for the configuration with $r_{ps} = r_{se} = 10$m where the results differ by about 1dB in the far field. The wavelength at 80Hz is 4.25m, so the secondary source was likely placed too close to the primary source for the results to be accurate. The best configuration for this frequency was $r_{ps} = 30$m, $r_{se} = 60$m, where about 10dB of attenuation was achieved.

Fig. 6.5 shows sample validation results for 160Hz for $r_{ps} = r_{se} = 20$m, $r_{ps} = r_{se} = 30$m and $r_{ps} = 30$m, $r_{se} = 60$m. The results for the image-source model and GFPE model did not converge as well as they did for an 80Hz signal. This indicates that ANC predictions using the GFPE may be less accurate at higher frequencies where small inaccuracies in the phase prediction have a more significant effect on the results. The best configuration in this case was $r_{ps} = 30$m, $r_{se} = 60$m, where about 10dB of attenuation was achieved by the image-phase method, and 8dB by the GFPE method. The results support the conclusion of

Germain that a quiet zone can be achieved when $r_{se} \geq 2r_{ps}$ [2].

6.3 Single-channel Control Results

6.3.1 Test Conditions

The effects of ground surface, temperature gradients and wind-speed gradients on the effectiveness of a single-channel control system were studied separately and in combination. The following atmospheric conditions were modeled:

- Stationary atmosphere;
- Weak, medium and strong temperature inversions;
- Temperature lapse;
- Weak, medium and strong temperature inversions with downwind;
- Temperature lapse with upwind.

For each atmospheric condition, predictions were made for reflective ground and for the finite-impedance ground used in the benchmark cases. The temperature-inversion conditions were defined as an increase of 0.9°C/100m for weak inversion, 1.8°C/100m for medium inversion and 3.6°C/100m for strong inversion [7]. Di's GFPE model uses an input file, in which the sound speed is given at different heights, to calculate the sound-speed gradient. The sound speeds that were input for the various temperature gradients are listed in Table 6.2.

The wind-speed gradient at height z was implemented using an effective sound-speed profile defined by:

$$c_{eff}(z) = c_o + b\ln\left(\frac{z}{z_o} + 1\right) \tag{6.2}$$

where c_o is the sound speed at the ground, z_o is the roughness length of the ground surface in meters, and b is a parameter describing refraction, in meters per second [21]. For the results shown here, $c_{eff}(z)$ was calculated using $b = 1\text{m/s}$ for downwind, $b = -1\text{m/s}$ for upwind, $z_o = 10^{-4}\text{m}$ for hard ground and $z_o = 10^{-2}\text{m}$ for soft

Table 6.2: Sound-speed profiles used in the GFPE model relative to ground sound speed for temperature lapse and weak, medium and strong inversion conditions.

	Relative sound speed (m/s)			
Height(m)	Weak inversion	Medium inversion	Strong inversion	Lapse
1				-2.97
10	+0.1	+0.1	+0.2	
100	+0.5	+1.1	+2.1	-6.0
200	+1.1	+2.1	+4.2	-6.0
300	+1.6	+3.2	+6.3	-6.0
350	+1.9	+3.7	+7.4	-6.0

Table 6.3: Sound-speed profiles used in the GFPE model relative to ground sound speed for temperature lapse with upwind and weak, medium and strong inversion conditions with downwind, for hard and soft ground.

	Relative sound speed (m/s)							
	Weak inversion		Medium inversion		Strong inversion		Lapse	
Height(m)	Hard	Soft	Hard	Soft	Hard	Soft	Hard	Soft
1							-12.2	-7.6
10	+11.6	+7.0	+11.6	+7.0	+11.7	+7.1		
100	+14.4	+9.7	+14.9	+10.3	+15.9	+11.3	-19.8	-15.2
200	+15.6	+11.0	+16.6	+12.0	+18.7	+14.1	-20.5	-16.9
300	+16.6	+11.9	+18.1	+ 13.5	+21.2	+16.6	-20.9	-17.3
350	+16.9	+12.3	+18.8	+14.2	+22.4	+17.8	-21.0	-17.4

ground. The downwind sound-speed profile was combined with the temperature-inversion conditions to simulate maximal downward refraction, and the upwind sound-speed profile was combined with the temperature-lapse conditions to simulate maximal upward refraction. The resulting sound speeds that were input to the GFPE model are summarized in Table 6.3.

The single-channel active-control simulations were run using r_{ps} = 30m, r_{se} = 60m for both 80Hz and 160Hz. As in the validation simulations, results were calculated up to a horizontal distance of 10km, using source and receiver heights of 4.5m.

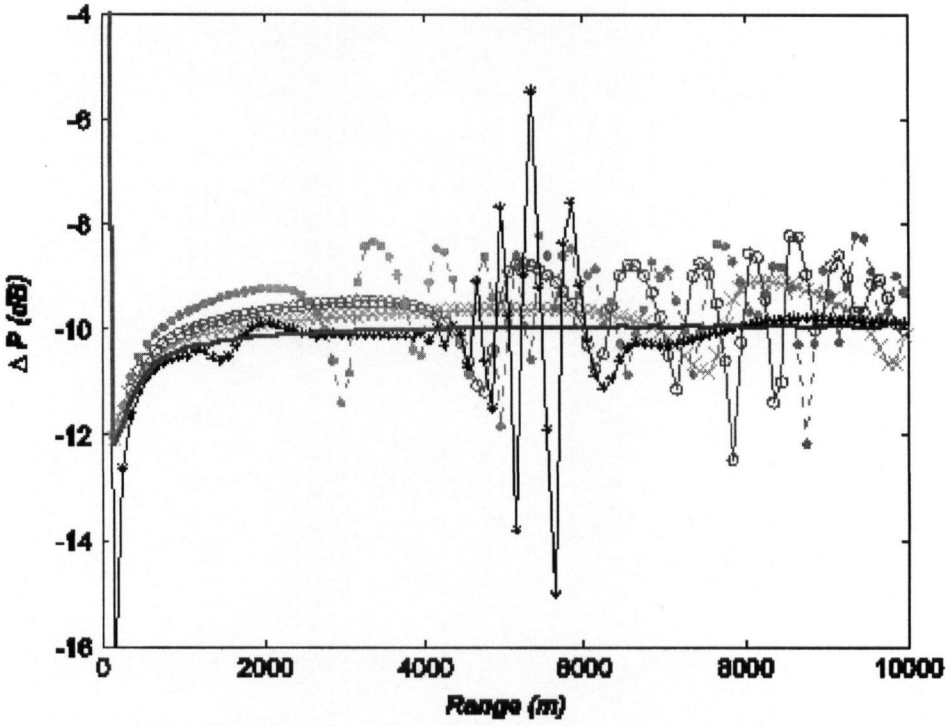

Figure 6.6: Single-channel ANC results for a monopole primary source at 80Hz in the presence of temperature gradients above reflective ground. — = no refraction, -x- = weak inversion, -o- = medium inversion, — · — = strong inversion, -∗- = lapse.

6.3.2 Effect of Temperature Gradients

The results at 80Hz for temperature inversion and lapse conditions above reflective ground are shown in Figs. 6.6. In the case of no refraction, about 10dB of attenuation was achieved in the far field. The temperature inversion caused fluctuations in the attenuation of ±2 to 3 dB. About 10dB of attenuation was achieved on average under all of the inversion conditions, although there were fluctuations. The spatial variations are caused by the interference patterns between the direct and reflected waves. Stronger inversion conditions, or stronger downwardly refractive conditions, cause constructive and destructive interference to occur at more points along the range. The temperature lapse caused large fluctuations in the middle range (4 to 6km).

At 160Hz, the control system is less effective overall, as can be seen in Fig. 6.7.

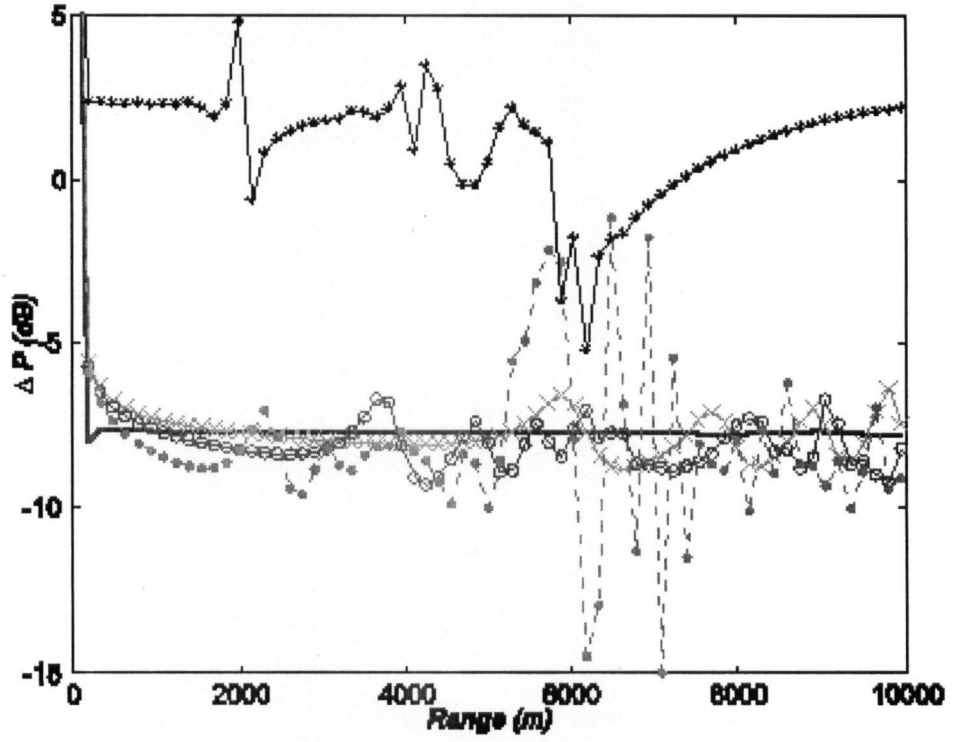

Figure 6.7: Single-channel ANC results for a monopole primary source at 160Hz in the presence of temperature gradients above reflective ground. — = no refraction, -x- = weak inversion, -o- = medium inversion, — · — = strong inversion, -∗- = lapse.

About 8dB of attenuation was obtained in the case of no refraction and, on average, under the temperature inversion conditions. The strong inversion case caused large fluctuations of (7 to 8 dB between 5km and 8km. Under temperature lapse conditions, no attenuation was achieved, on average. At this higher frequency, the performance of the control system was more sensitive to the refractive atmosphere. The shorter wavelength makes phase matching more difficult, which can cause larger fluctuations in the control results.

6.3.3 Effect of Temperature Gradients Over Soft Ground

Fig. 6.8 shows the results for temperature inversion and lapse conditions in the presence of soft ground at 80Hz. The attenuation for a non-refractive atmosphere

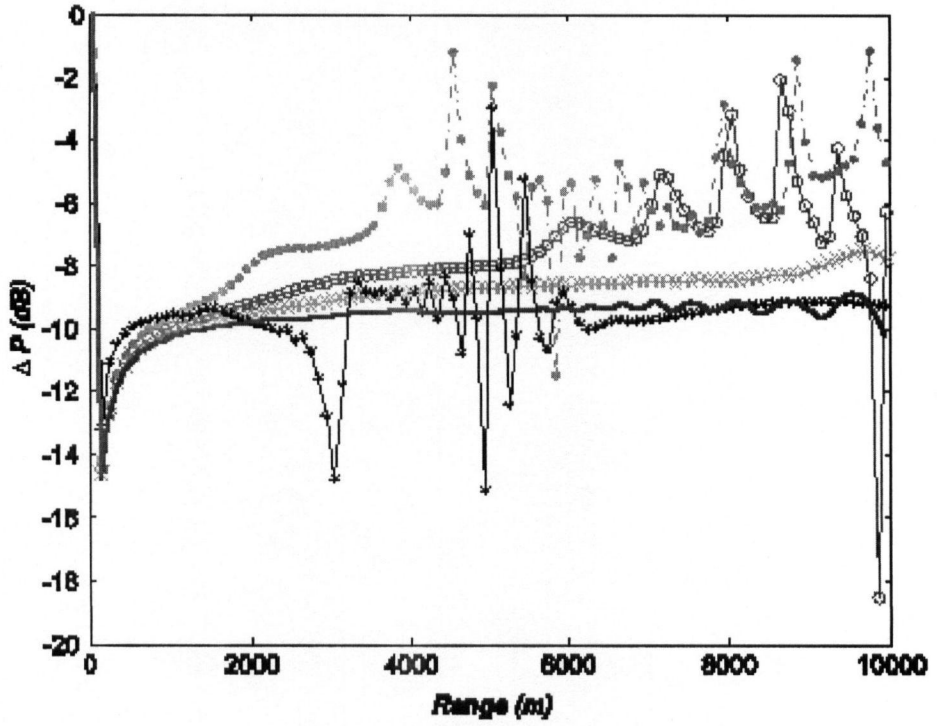

Figure 6.8: Single-channel ANC results for a monopole primary source at 80Hz in the presence of temperature gradients above soft ground. — = no refraction, -x- = weak inversion, -o- = medium inversion, — · — = strong inversion, -∗- = lapse.

is also shown, to show the effect that the soft ground has on the control results. For no refraction over reflective ground, the attenuation levels are relatively flat across the entire 10km range for both frequencies, as shown in Figs 6.7 and 6.8. At 80Hz, the soft ground causes the attenuation to vary slightly in the far field, although the fluctuations are less than 1dB. Temperature inversion conditions decreased the performance of the ANC system. The attenuation was 8 to 9dB under weak inversion conditions and about 7dB on average for medium and strong inversion conditions. The stronger inversions caused large fluctuations in the attenuation. The result for the temperature lapse is similar to that with reflective ground, with large fluctuations in the middle of the range.

The temperature gradients combined with the soft ground had a more severe effect on the performance of the control system at 160Hz, as can be seen in

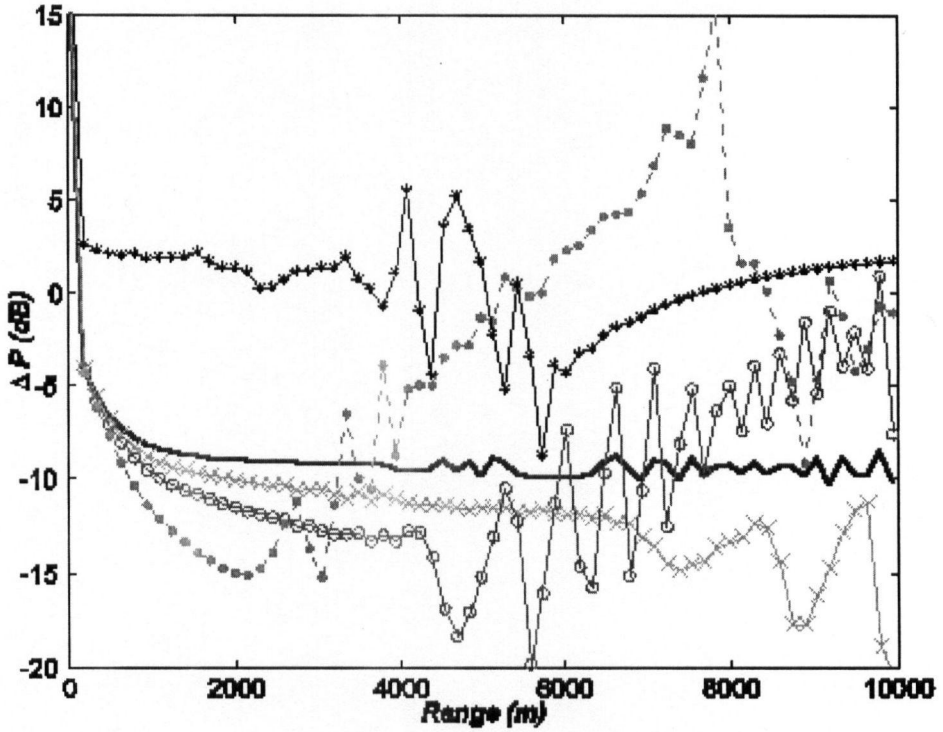

Figure 6.9: Single-channel ANC results for a monopole primary source at 160Hz in the presence of temperature gradients above soft ground. — = no refraction, -x- = weak inversion, -o- = medium inversion, – · – = strong inversion, -∗- = lapse.

Fig. 6.9. In the case of no refraction, the system decreased the sound field by about 9dB on average. While the performance of the system actually increased slightly under weak inversion conditions, medium and strong inversion conditions caused strong fluctuations, rendering the system ineffective in the far field. As was the case for reflective ground at this frequency, no attenuation was obtained under temperature-lapse conditions. The complex impedance of the ground surface causes the sound waves to suffer a phase shift on reflection, which clearly has an adverse effect on the performance of the control system, particularly at this higher frequency.

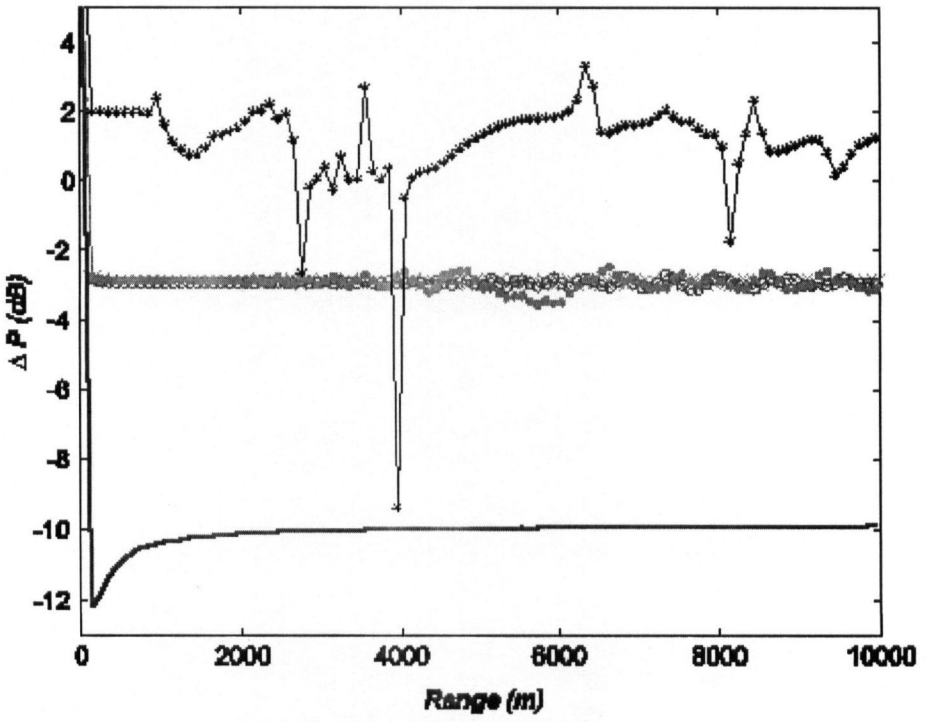

Figure 6.10: Single-channel ANC results for a monopole primary source at 80Hz in the presence of temperature and wind-speed gradients above hard ground. — = no refraction, -x- = weak inversion, -o- = medium inversion, – · – = strong inversion, -∗- = lapse.

6.3.4 Effect of Temperature and Wind-speed Gradients

Fig. 6.10 shows the results at 80Hz for temperature inversion with downwind conditions, as well as for temperature lapse with upwind conditions, in the presence of reflective ground. The results for the different degrees of temperature inversion are almost identical, showing about 3dB of attenuation along the entire range. This indicates that the effects of a strong downwind dominate over temperature-inversion effects. The control system is ineffective under temperature-lapse conditions in the presence of an upwind; the sound field increased by about 1dB on average.

For 160Hz, the results were also similar for the different degrees of temperature inversion, as shown in Fig. 6.11. However, no attenuation was achieved at this frequency, and the inversion conditions caused fluctuations of about 2 to 3dB

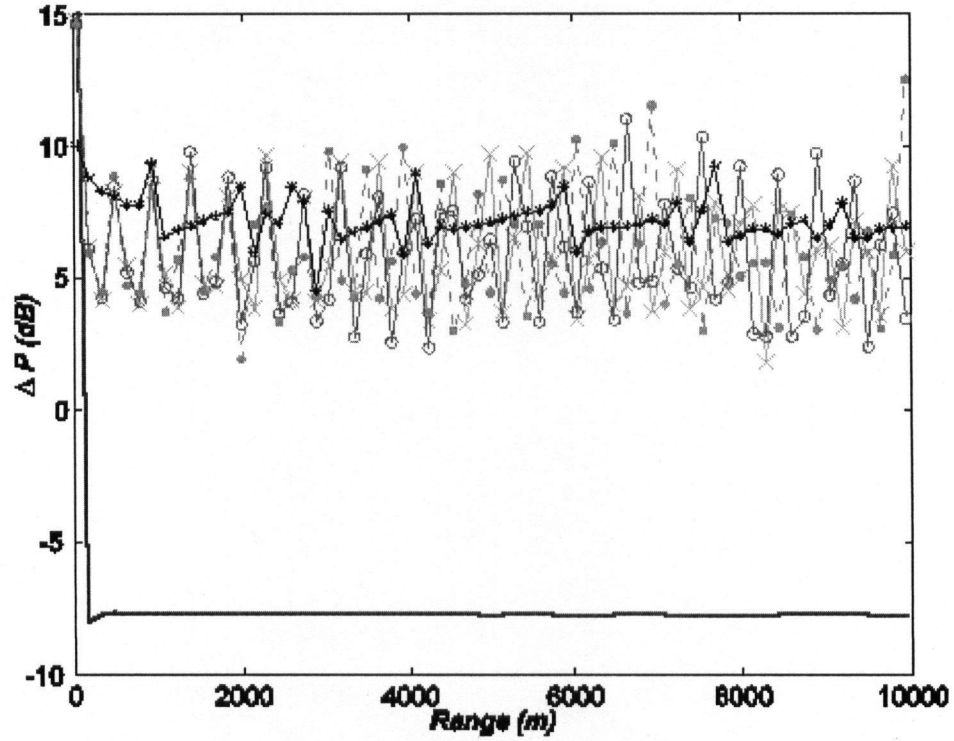

Figure 6.11: Single-channel ANC results for a monopole primary source at 160Hz in the presence of temperature and wind-speed gradients above hard ground. — = no refraction, -x- = weak inversion, -o- = medium inversion, — · — = strong inversion, -∗- = lapse.

across the entire range. Under temperature-lapse conditions, the fluctuations were less severe but, as was the case for inversion conditions, the sound field increased by about 7dB on average.

6.3.5 Effect of Temperature and Wind-Speed Gradients Over Soft Ground

Figs. 6.12 and 6.13 show the results for the most complex conditions, combining temperature and wind-speed gradients with soft ground at 80Hz and 160Hz, respectively. The control system did not achieve any attenuation at large distances for any of the refractive cases. The sound field increased by an average of 2dB at 80Hz and 5dB at 160Hz. As in the previous cases, the fluctuations in the results were much larger at 160Hz than at 80Hz. The combination of soft ground and

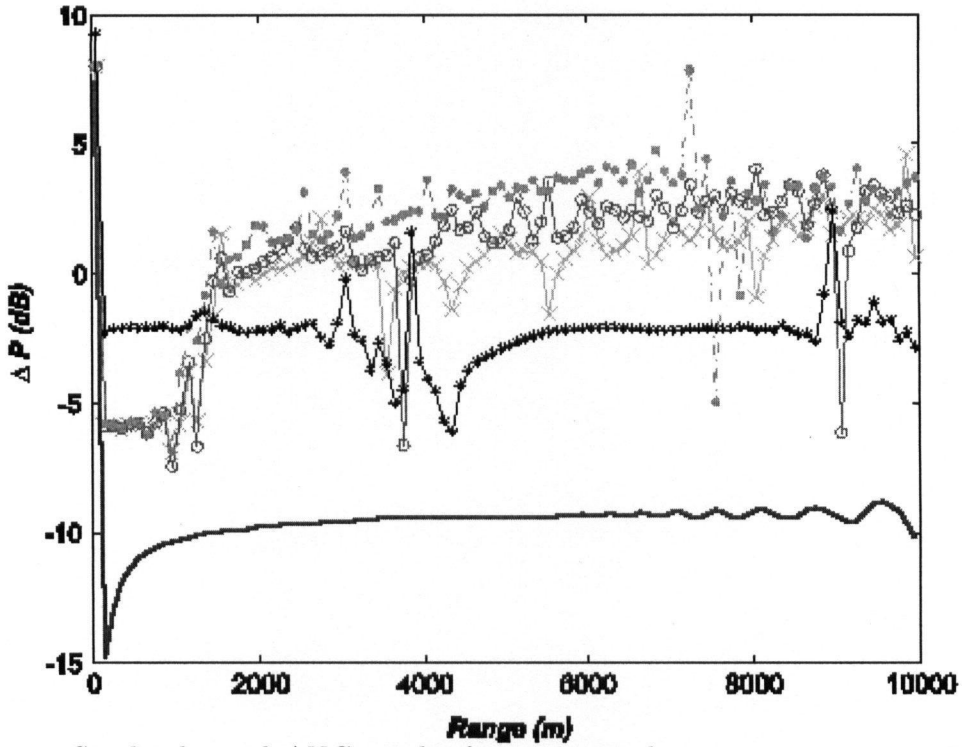

Figure 6.12: Single-channel ANC results for a monopole primary source at 80Hz in the presence of temperature and wind-speed gradients above soft ground. — = no refraction, -x- = weak inversion, -o- = medium inversion, — · — = strong inversion, -∗- = lapse.

wind-speed gradients causes complex interference patterns in the sound field that cannot be controlled by a single-channel ANC system.

6.3.6 Discussion of the Results

Clearly, atmospheric refraction and complex-impedance ground have a significant effect on the performance of a single-channel control system. It is most difficult to achieve attenuation under temperature-lapse conditions, especially in the presence of an upwind. However, under such conditions, the noise levels near the ground have already been significantly attenuated due to upward refraction of the sound waves, as was shown in Figs. 6.2 and 6.3. It is thus more important to concentrate on attenuating the noise under temperature-inversion and downwind

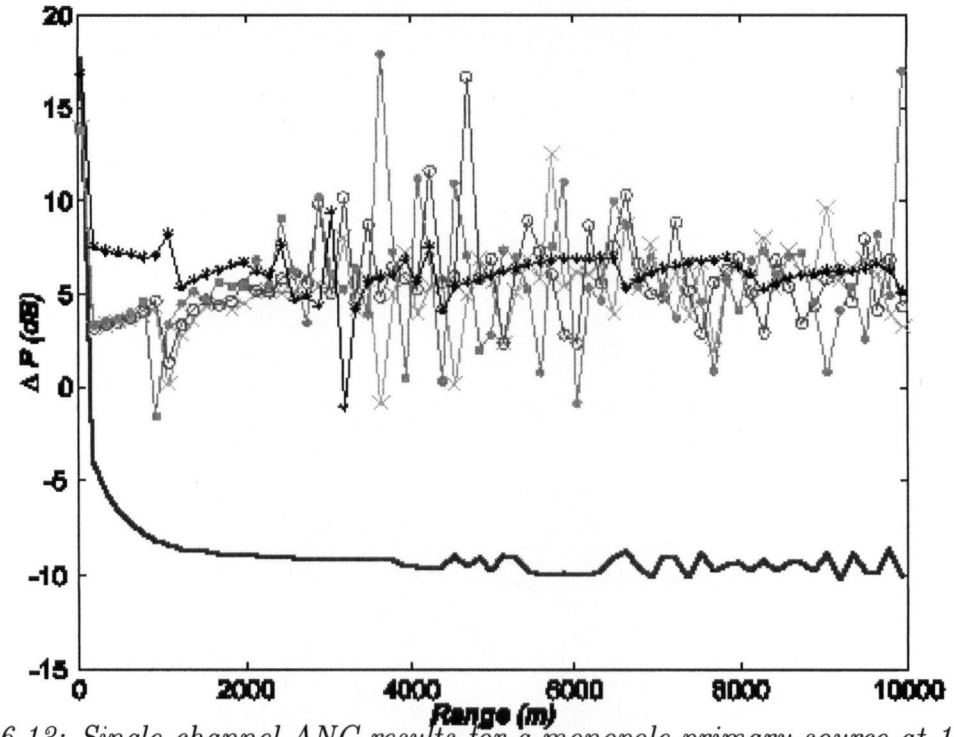

Figure 6.13: Single-channel ANC results for a monopole primary source at 160Hz in the presence of temperature and wind-speed gradients above soft ground. — = no refraction, -x- = weak inversion, -o- = medium inversion, — · — = strong inversion, -∗- = lapse.

conditions.

The approximate total sound power output increase of the single-channel control system at the distance of 3km are listed in Table 6.4. This table summarizes the amount of attention that can be expected at a community located 3km away from the airport for the various environmental conditions. Transmission loss values, including the attenuation achieved by the ANC system, are also listed. A significant amount of attenuation (7.0 to 13.0dB) can be expected at 80 and 160Hz when atmospheric refraction is relatively weak; that is, when there is only refraction due to temperature gradients. For these cases, the transmission loss was already significant before the attenuation achieved by ANC was taken into account, so ANC may not be necessary.

In the presence of a downwind or upwind, the system achieves little or no at-

Table 6.4: Approximate total sound power output increase of a single-channel control system, and total transmission loss including ANC, at a distance of 3km for different grounds and atmospheric conditions.

Atmospheric Conditions	Ground Type	ΔP (dB)		Transmission Loss (dB)	
		80 Hz	160 Hz	80 Hz	160Hz
No Refraction	Hard	-10.5	-7.0	-72.5	-71.0
	Soft	-10.0	-9.0	-93.5	-108.7
Weak inversion	Hard	-10.0	-7.0	-68.1	-62.8
	Soft	-10.0	-10.5	-92.2	-110.4
Medium inversion	Hard	-9.5	-7.0	-63.0	-60.2
	Soft	-8.5	-12.5	-85.7	-91.0
Strong inversion	Hard	-11.0	-7.5	-69.6	-59.7
	Soft	-7.5	-12.0	-77.6	-87.8
Lapse	Hard	-10.5	+2.0	-107.4	-106.8
	Soft	-13.0	0.0	-127.0	-124.2
Weak inversion	Hard	-3.0	+6.0	-52.1	-41.5
+ downwind	Soft	0.0	+ 5.0	-99.5	-63.6
Medium inversion	Hard	-3.0	+6.0	-52.2	-43.4
+ downwind	Soft	0.0	+ 6.0	-109.0	-60.4
Strong inversion	Hard	-3.0	+7.0	-52.2	-39.4
+ downwind	Soft	+1.0	+ 7.0	-98.5	-58.4
Lapse	Hard	0.0	+7.0	-138.8	-153.4
+ upwind	Soft	-4.0	+ 3.0	-151.0	-137.1

tenuation at 80Hz, and increases the noise by several dB at 160Hz. In the case of an upwind, the transmission loss is already significant, so ANC is not required. Under downwind conditions, however, the 80Hz signal only decays by about 50dB in the case of hard ground. As shown in Chapter 5, the loudest tonal signal at 80Hz when the Dash-8 engines were operating at full power was 120dB. Thus, a 70dB signal would be heard at a community 3km away. The 160Hz noise would also be audible, as the transmission loss is only about 40dB for hard ground. For soft ground, the transmission loss is significant at 80Hz, indicating that strong destructive interference occurs at 3km. The losses are less significant for 160Hz (about 60dB). It is clear that noise reduction is needed under downwind conditions, particularly in the case of hard ground.

These simulation results show that a quiet zone (>10dB of attenuation) cannot

be achieved by a single-channel control system under realistic outdoor conditions. It is evident that more control channels must be included in the simulations, in order to investigate the feasibility of using ANC to control the Dash-8 tonal noise. However, implementing an array of control channels into the GFPE model would require extending the model to 3 dimensions. Limitations of the GFPE model are discussed in the next section.

6.4 Limitations of the GFPE: Implications for Future Work

The GFPE method is only valid for sound waves leaving the source at propagation angles of less than about 30°. Thus, predictions can only be made for a monopole source, as dipole and quadrupole radiation cannot be accurately modeled. Furthermore, although it is possible to predict the sound field due to multiple monopole noise sources, all of the sources must lie in the vertical (x-z) plane. Since it is not possible to model the contribution of sources lying in the horizontal plane, only single-channel control can be implemented. Salomons describes equations for a three-dimensional GFPE model in his book, but there is no indication that the model has been successfully implemented numerically [21].

Taherzadeh has developed an FFP model that can predict the sound field for dipole and quadrupole sources. However, contributions from off-axis sources (i.e. from an array of control channels) cannot be included in the existing model. As was the case with the GFPE model, only single-channel control can be implemented. In addition, the FFP model is limited in that it cannot model range-dependent factors such as irregular terrain and turbulence [21].

In order to predict the effectiveness of a multiple-channel active-control system on a directional noise source under complex meteorological conditions, a fully three-dimensional model is required. In the interest of predicting the performance of an active control system on the Dash-8 run-up noise, it would be best to extend

the FFP model predict to a three-dimensional solution so that multi-channel control can be implemented. While the model may have some limitations, it has the advantage over the GFPE model that directional noise sources can be modeled.

Chapter 7

Conclusion

7.1 Accomplishments

The purpose of this work was to extend Germain's work [2] on investigating the feasibility of using active noise control to reduce the propeller aircraft engine run-up noise that is radiated into communities near the Vancouver International Airport. Germain's work focused on ANC in free-field and half-space conditions. Since the engine run-up tests are performed outdoors, it was essential to consider the effects of meteorological conditions and outdoor ground surfaces on the performance of an ANC system. Furthermore, since propeller aircraft are not omnidirectional noise sources, it was of interest to measure the performance of an ANC system on directional noise sources.

A literature overview on outdoor sound propagation was performed. It was found that the simple treatment of sound propagation in a half-space condition, in which only the contributions from the direct and reflected sound waves are considered, is insufficient for sound propagation over a ground with a complex impedance. Complex ground surfaces give rise to ground and surface waves whose contributions to the sound field must be included for accurate results [7]. In an outdoor environment, sound waves are refracted by temperature and wind-speed gradients. Since the run-up tests are performed at nighttime, when there are typically temperature lapse conditions, sound waves are refracted down towards the ground, resulting in higher levels than would be heard during the daytime. If temperature inversion conditions are combined with a downwind, the noise levels can be even louder.

ANC simulations and experiments were performed on a dipole primary source

in the free-field. For multi-channel control, it was found that the range of secondary speaker spacings for optimal control is smaller than that for a monopole primary source. The performance of the control system depends on the orientation of the dipole source. The ANC system was found to be most effective when it is used to create quiet zones in the direction of the strongest primary source radiations. Guo and Pan found a similar result for a quadrupole primary source [13]. Thus, it is important to understand the directivity of the aircraft in order to set-up the active control system in the optimal configuration.

Germain performed measurements and analysis of run-up noise from a Beechcraft 1900D. While this information was useful, it was of interest to study the Dash-8, as it is a source of noise complaints at the Vancouver International Airport. Measurement and analysis of Dash-8 noise was done for idle, full-power and half-power engine settings. It was found that the idling engine noise does not contain enough tonal components to be a candidate for ANC. The fundamental frequencies for half-power and full-power engine noises were 69Hz and 80Hz, respectively, making them good candidates for ANC. The harmonics of these frequencies were significant near the front of the plane. The directivity of the Dash-8 operating at full engine power was shown to be asymmetric, with the strongest radiation behind the right propeller. The directivity was approximately quadrupole in shape, further confirming the need to study ANC on directional sources. Even if ANC is not implemented, it may be feasible to turn the aircraft such that the direction of strongest noise radiation is not directed at noise-sensitive areas (residential communities).

A literature review on prediction models for outdoor sound propagation was also performed. The models become increasingly complex as more and more outdoor phenomena are included. The Green's function parabolic equation (GFPE) method has been used by many researchers in recent years because it is computationally efficient, and complex phenomena such as turbulence and irregular terrain can be accounted for. This makes the GFPE a more sophisticated ap-

proach than the Crank-Nicholson parabolic equation (CNPE) and the Fast-field program (FFP), which can model atmospheric refraction, but cannot model range-dependent effects. The GFPE model was thus chosen as the method to be used in the prediction of active control on outdoor sound.

A GFPE model was obtained by Dr. Xiao Di at Pennsylvania State University. The code was modified to include a single active control channel, and validation work was performed by comparing the results to those predicted with Guo's and Pan's image-source model for ANC in a half-space. Predictions were then done over a horizontal range of 10km using the GFPE model for a number of atmospheric conditions, using reflective and soft ground. Atmospheric refraction tended to cause fluctuations in the attenuation and decrease the overall performance of the control system. Little or no attenuation was achieved under temperature lapse conditions, and soft ground decreased the average amount of attenuation. In general, the control system was more effective at controlling an 80Hz signal than a 160Hz signal.

The single-channel control results at a distance of 3km were summarized in Table 6.4 to show the expected performance of the control system at a residential community near YVR. Significant attenuation can be achieved in the case of weak atmospheric refraction (temperature gradients only, with no wind) for both reflective and soft ground. However, the system is ineffective in the presence of wind, particularly at 160Hz. It is evident that a single-channel control system is insufficient to achieve significant attenuation under realistic meteorological conditions.

7.2 Future Work

This research has succeeded in measuring the effectiveness of an active control system on directional sources. Further investigations could include ANC experiments on a quadrupole primary source to verify the simulation results obtained by Guo [13]. Preliminary results for the effect of meteorological conditions and ground impedance on a single control system were obtained. However, the GFPE

model that was used for the predictions is limited. Since the parabolic equation approximation that is used by the GFPE limits the propagation angles of the sound waves that are radiated from the source, dipole and quadrupole sources cannot be modeled. In addition, the GFPE that was used is a two-dimensional model. Contributions of off-axis sources to the sound field cannot be included in the solution, meaning that an array of control channels in the horizontal plane cannot be implemented. In order to predict for multi-channel control, a fully three-dimensional model is required. Three-dimensional models for outdoor sound propagation are not often found in literature. Although there have been some references to a three-dimensional GFPE model, [21], it is not clear from the theory that the model can predict the contribution of off-axis sources.

In the single-channel ANC predictions that were performed in this research, the ground was assumed to be homogenous. The land surrounding the Vancouver International Airport consists of different types of ground surfaces. The region from which noise complaints are generated is on an upslope, meaning that varying terrain must be considered in the predictions.

ANC experiments could be performed on-site on a small scale. It may be feasible to attempt using single- or multi-channel control on a dipole or a quadrupole primary source placed at the run-up site, and take measurements in the far-field. These experiments would serve to validate the single-channel control results shown in this thesis, as well as give an idea as to the difference in performance between a single-channel and a multi-channel ANC system.

Bibliography

[1] Vancouver International Airport Authority. Noise Management Annual Report, 2000.

[2] P. Germain. Active Control of Run-up Noise from Propeller Aircraft. M.A.Sc. Thesis, 2000.

[3] L.J. Eriksson. Active Sound and Vibration Control: A Technology in Transition. Noise Control Eng. J. 44 (1), 1996.

[4] T.J. Sutton, S.J. Elliot, A.M. McDonald, and T.J. Saunders. Active Control of Road Noise Inside Vehicles. Noise Control Eng. J. 42 (4), 1994.

[5] J. Guo and J. Pan. Local or global control - The applicable active noise control strategy in enclosed environments. ACTIVE 2002 conference proceedings, 2002.

[6] C. M. Harris. Handbook of Acoustical Measurements and Noise Control. McGraw-Hill Inc., 1991.

[7] T. F. W. Embleton. Tutorial on Sound Propagation Outdoors. J. Acoust. Soc. Am. 100(1), July 1996.

[8] M. J. Crocker and A. J. Price. Noise and Noise Control. CRC Press, 1975.

[9] D. A. Bies and C. H. Hansen. Engineering Noise Control, Theory and Practice. E & FN Spon, 1996.

[10] E. M. Salomons. Computational Atmospheric Acoustics. Kluwer Academic Publishers, 2001.

[11] G. C. Lauchle, J. R. MacGillivray and D. C. Swanson. Active Control of Axial-Flow Fan Noise. J. Acoust. Soc. Am. 101(1), 1997.

[12] K. M. Li, S. Taherzadeh and K. Attenborough. Sound Propagation from a Dipole Source Near an Impedance Plane." J. Acoust. Soc. Am. 101(6), 1997.

[13] J. Guo, J. Pan, M. Hodgson and A. Nakashima. Active Control of Noise from Directional Sources in Open Spaces. WESPAC VIII Conference proceedings, 2003.

[14] J. Guo. Active Noise Control in Open Space and Active Noise Barriers. Ph.D. Dissertation, University of Western Australia, 1997.

[15] J. Guo and J. Pan. Further Investigation on Actively Created Quiet Zones by Multiple Control Sources in Free Space. J. Acoust. Soc. Am. 102(5), 1997.

[16] J. Guo and J. Pan. Effects of Reflective Ground on the Actively Created Quiet Zones. J. Acoust. Soc. Am, 103(2), 1998.

[17] Aeroacoustics of Flight Vehicles. Acoustical Society of America, 1995.

[18] K. M. Li, S. Taherzadeh and K. Attenborough. Sound Propagation from a Dipole Source Near an Impedance Plane. J. Acoust. Soc. Am. 101(6), 1997.

[19] A. Nakashima, J. Guo and M. Hodgson. Preliminary Investigation of Active Control for Dipole Noise Sources. ACTIVE 2002 conference proceedings, 2002.

[20] Burns and McDonnel. Aircraft Characteristics Planning Data, 1995.

[21] E. M. Salomons. Computational Atmospheric Acoustics. Kluwer Academic Publishers, 2001.

[22] K. Attenborough *et al.* Benchmark Cases for Outdoor Sound Propagation. J. Acoust. Soc. Am. 97(1), 1995.

[23] K.E. Gilbert and X. Di. A Fast Green's Function Method for One-way Sound Propagation in the Atmosphere. J. Acoust. Soc. Am. 94(4), 1993.

[24] K. E. Gilbert and M. J. White. Application of the parabolic equation to sound propagation in a refracting atmosphere. J. Acoust. Soc. Am. 85(2), 1989.

[25] E. M. Salomons. Improved Green's Function Parabolic Equation Method for Atmospheric Sound Propagation. J. Acoust. Soc Am. 104(1), 1998.

Appendix A

Idle Engine Spectra

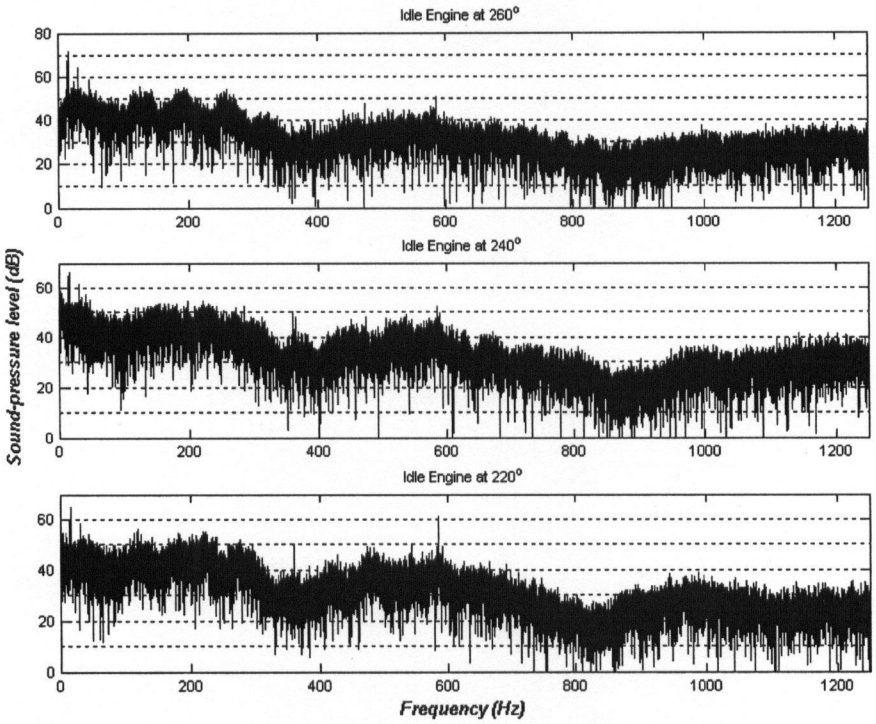

Figure A.1: Narrow band spectra for both engines idle at positions 220^0, 240^0 *and* 260^0.

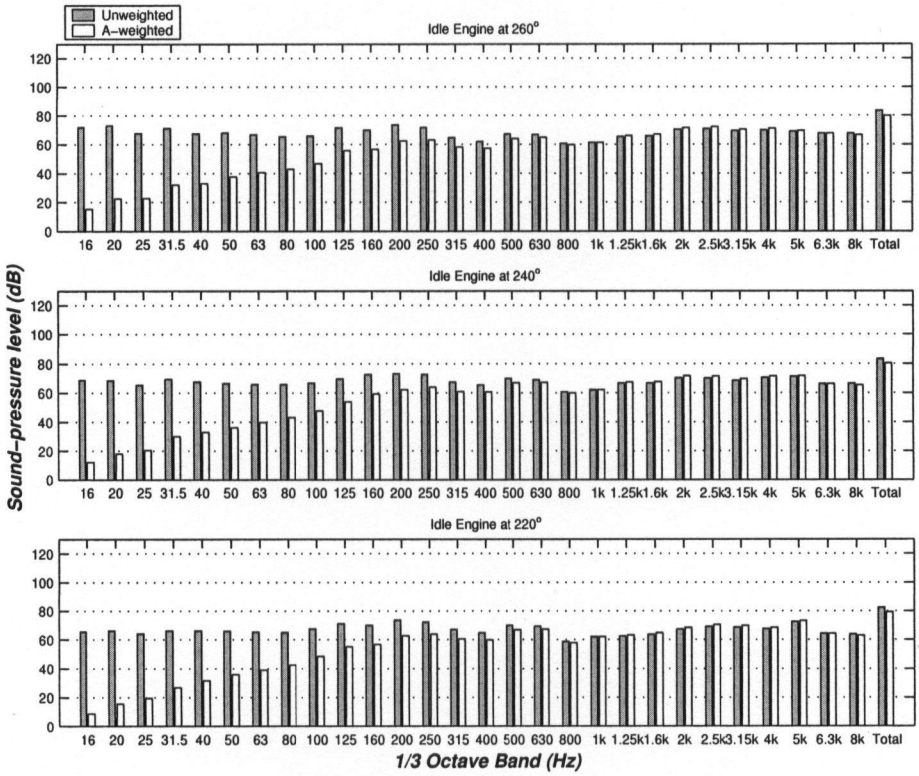

Figure A.2: 1/3 octave band spectra for both engines idle at positions 220^0, 240^0 *and* 260^0.

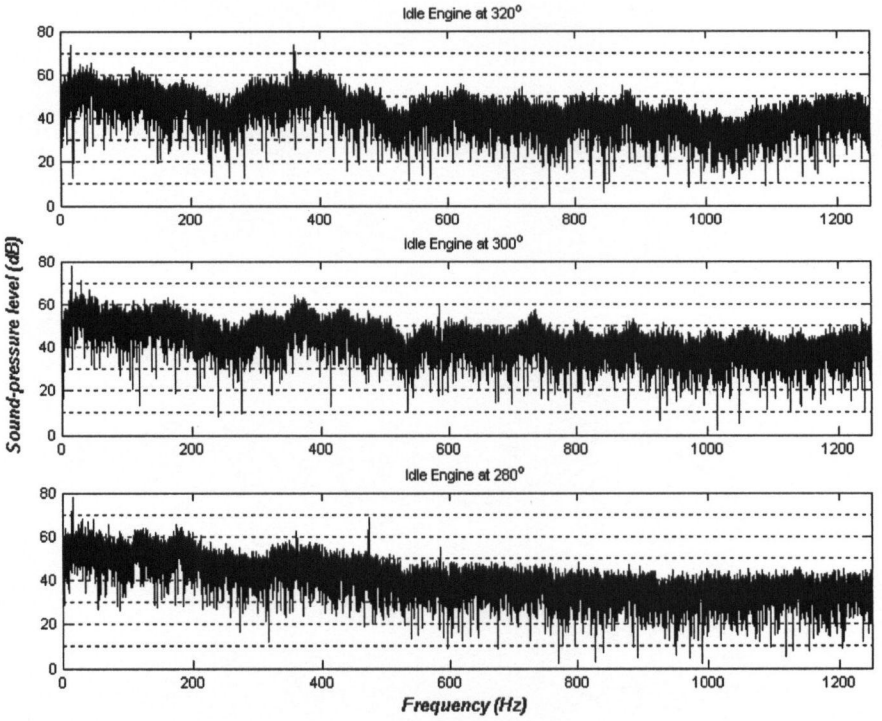

Figure A.3: Narrow band spectra for both engines idle at positions 280^0, 300^0 *and* 320^0.

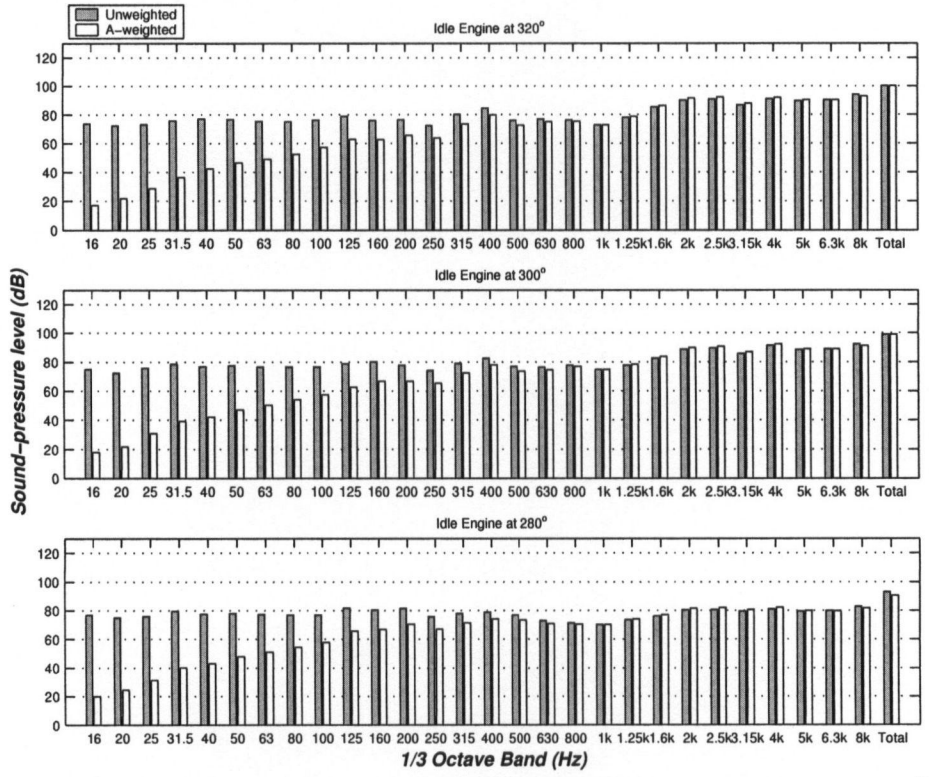

Figure A.4: 1/3 octave band spectra for both engines idle at positions 280^0, 300^0 *and* 320^0.

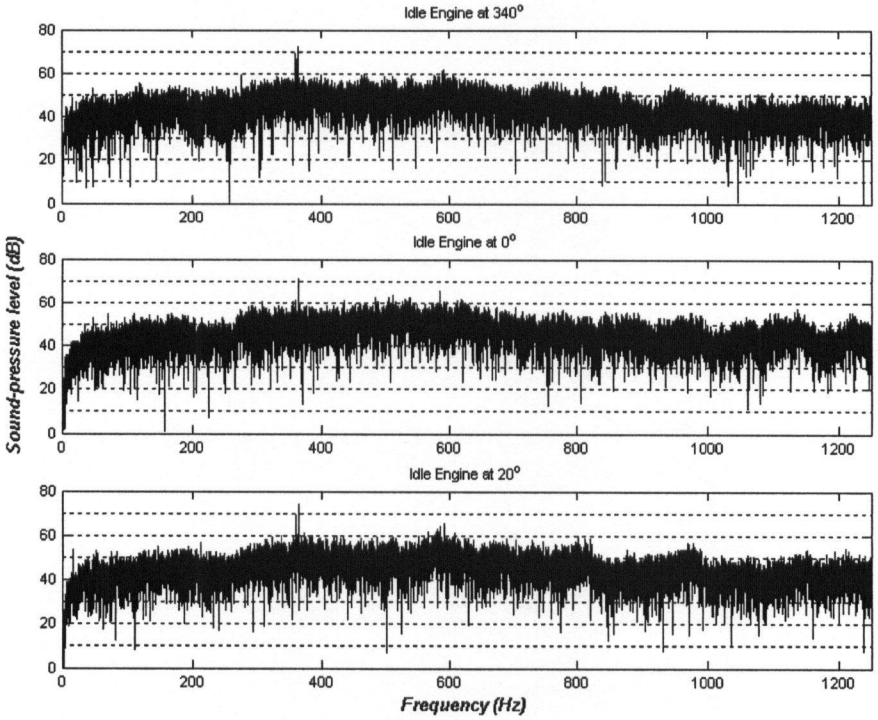

Figure A.5: Narrow band spectra for both engines idle at positions 340^0, 0^0 *and* 20^0.

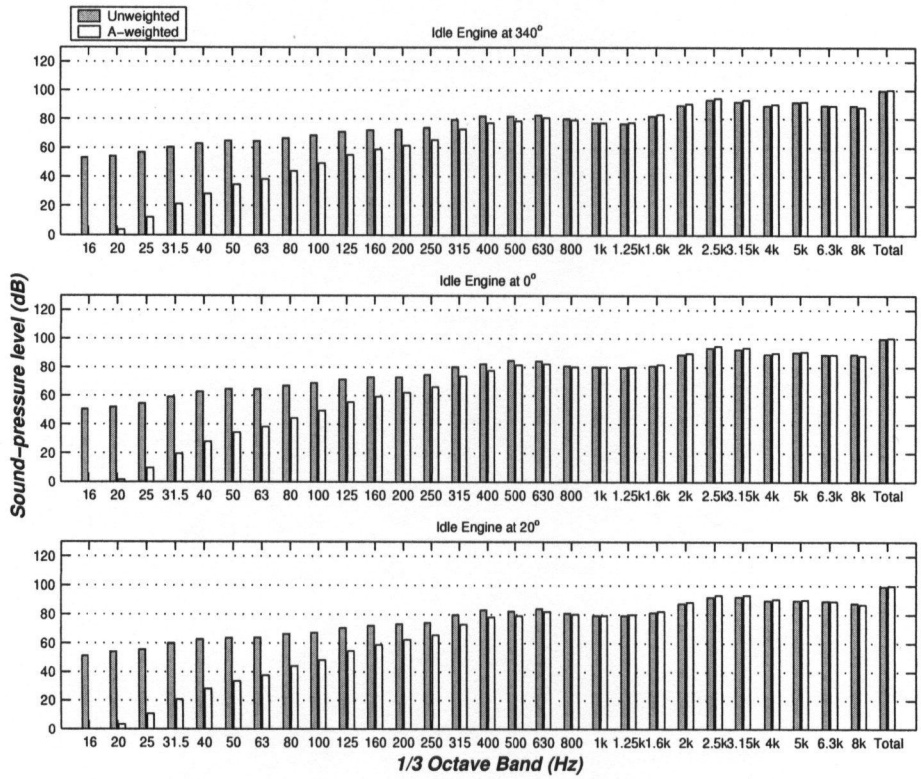

Figure A.6: 1/3 octave band spectra for both engines idle at positions 340^0, 0^0 *and* 20^0.

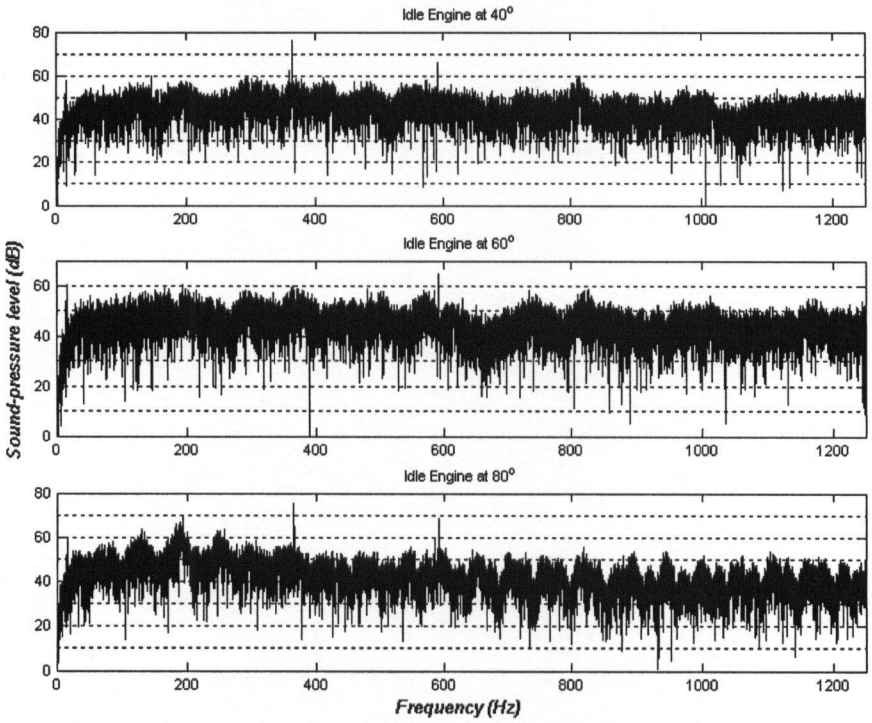

Figure A.7: Narrow band spectra for both engines idle at positions 40^0, 60^0 *and* 80^0.

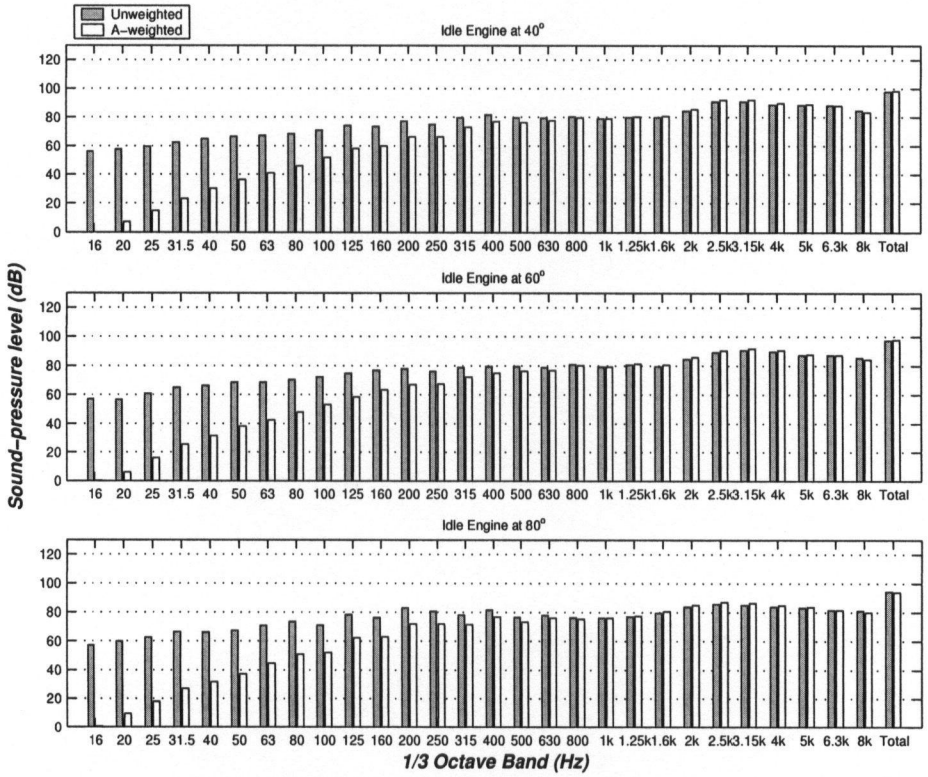

Figure A.8: 1/3 octave band spectra for both engines idle at positions 40^0, 60^0 *and* 80^0.

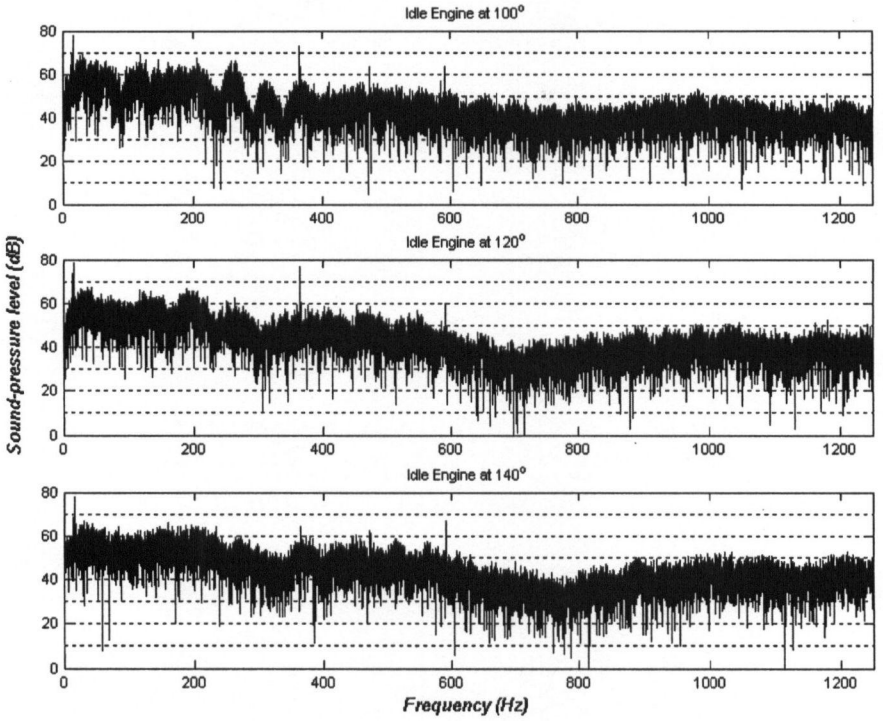

Figure A.9: Narrow band spectra for both engines idle at positions 100^0, 120^0 *and* 140^0.

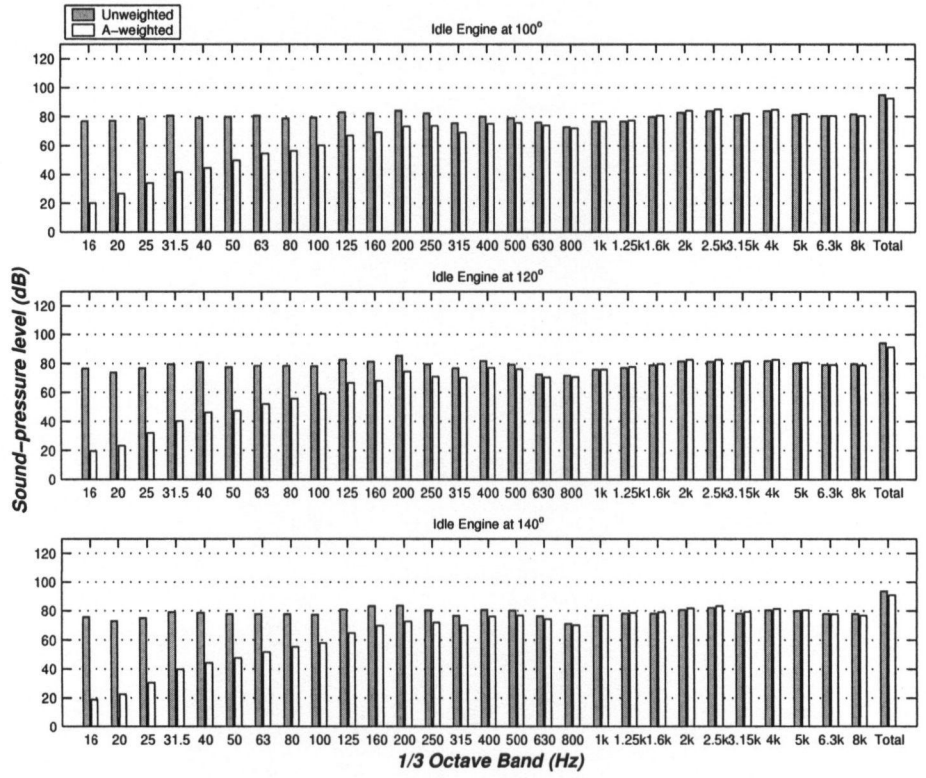

Figure A.10: 1/3 octave band spectra for both engines idle at positions 100^0, 120^0 *and* 140^0.

Appendix B

Full Power Engine Spectra

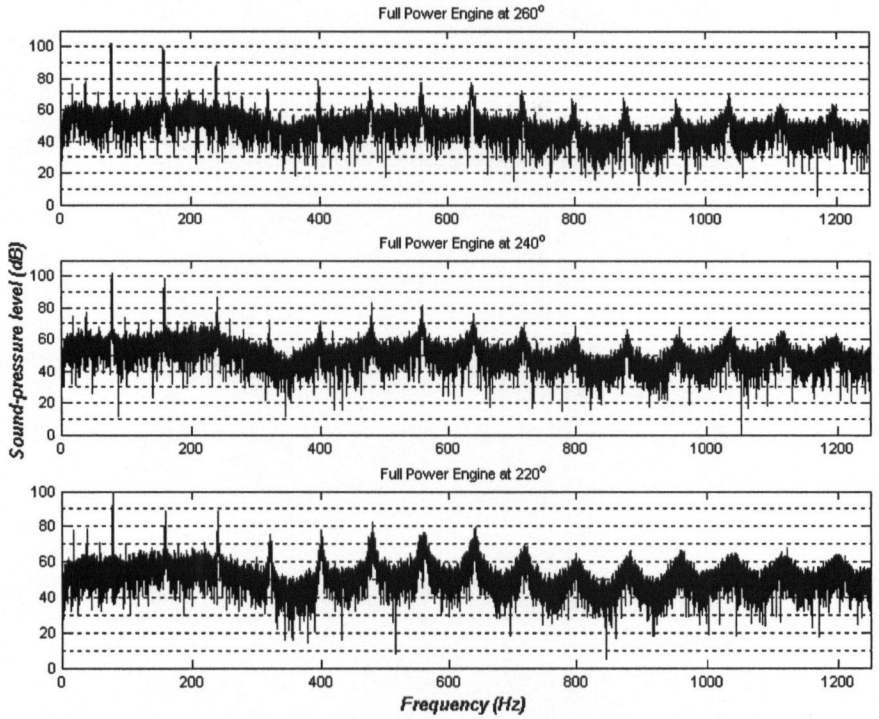

Figure B.1: Narrow band spectra for both engines at full power at positions 220^0, 240^0 *and* 260^0.

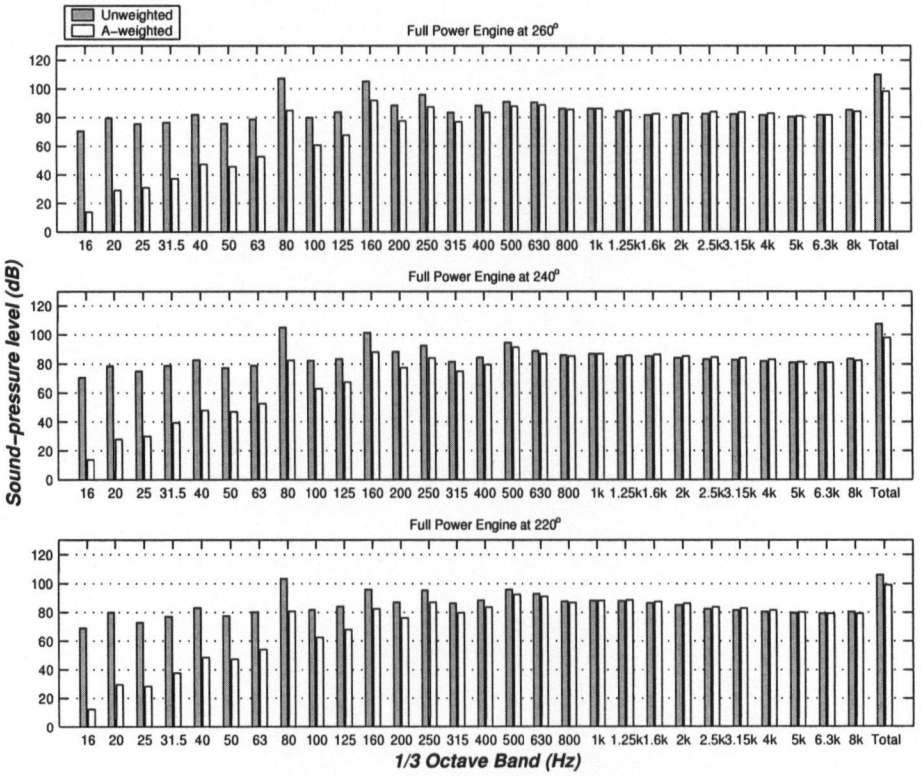

Figure B.2: 1/3 octave band spectra for both engines at full power at positions 220^0, 240^0 *and* 260^0.

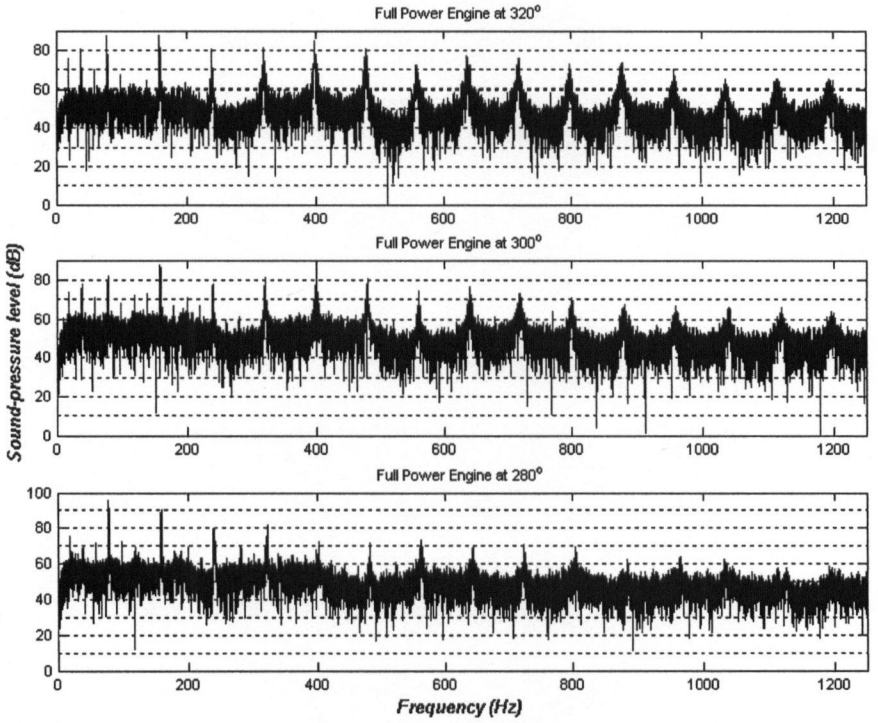

Figure B.3: Narrow band spectra for both engines at full power at positions 280^0, 300^0 *and* 320^0.

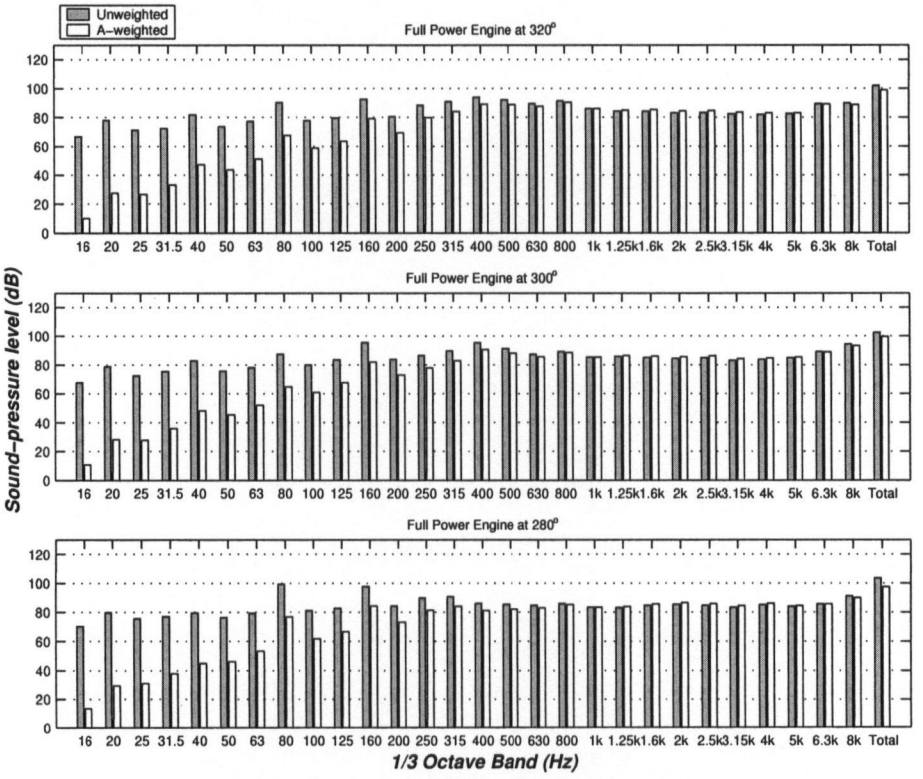

Figure B.4: 1/3 octave band spectra for both engines at full power at positions 280^0, 300^0 *and* 320^0.

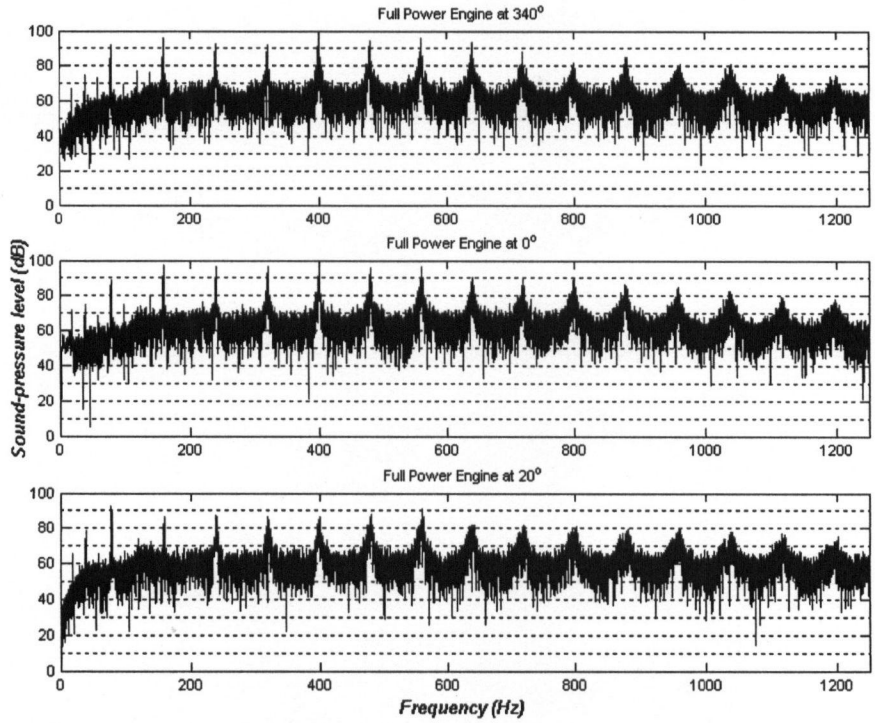

Figure B.5: Narrow band spectra for both engines at full power at positions 340^0, 0^0 *and* 20^0.

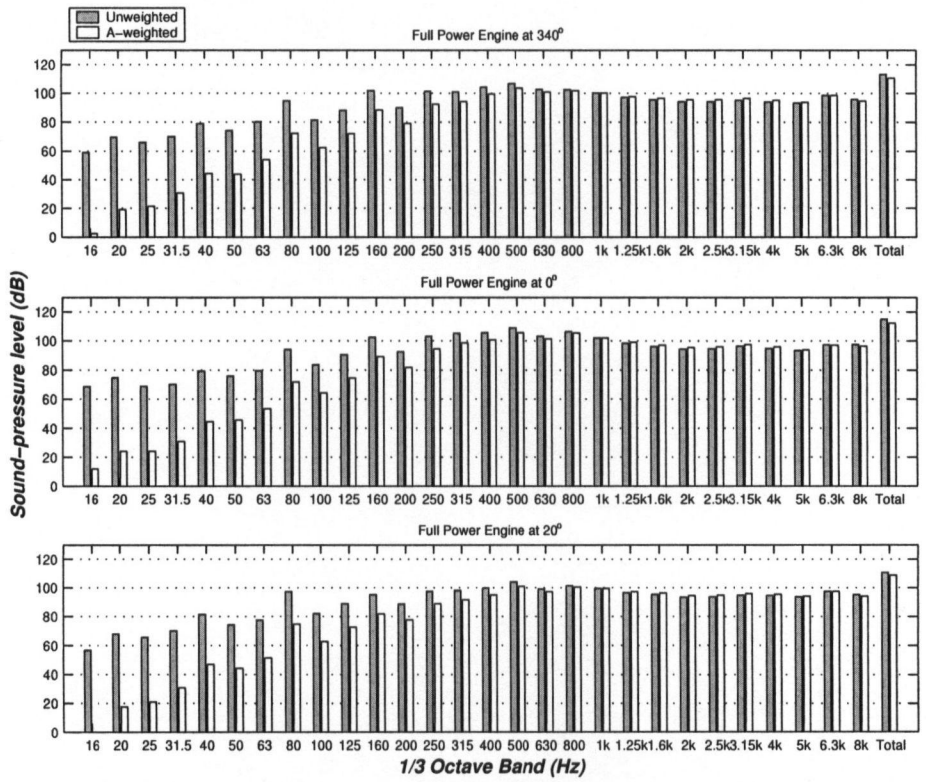

Figure B.6: 1/3 octave band spectra for both engines at full power at positions 340^0, 0^0 *and* 20^0.

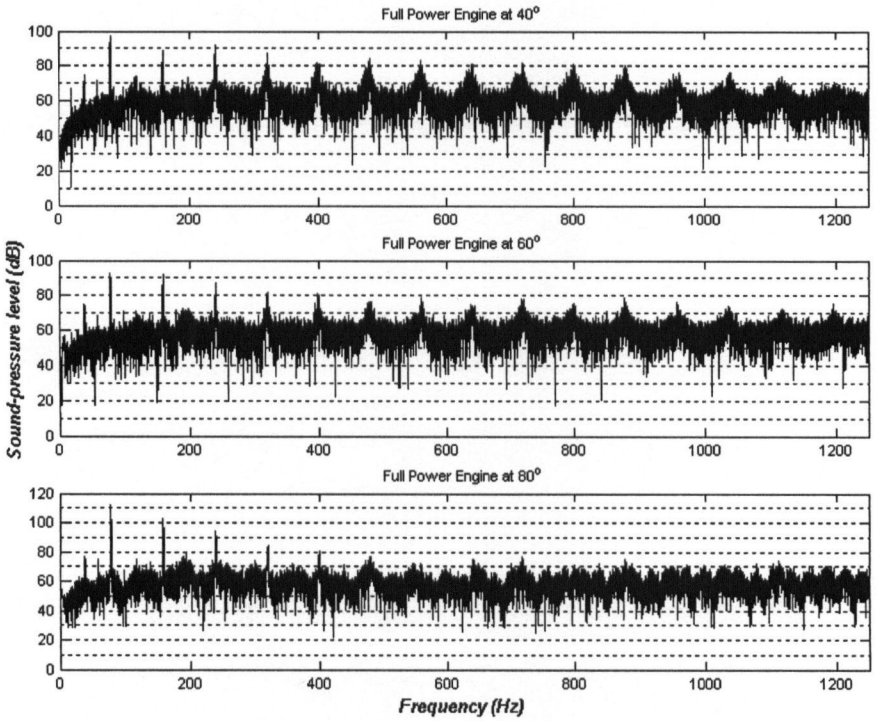

Figure B.7: Narrow band spectra for both engines at full power at positions 40^0, 60^0 *and* 80^0.

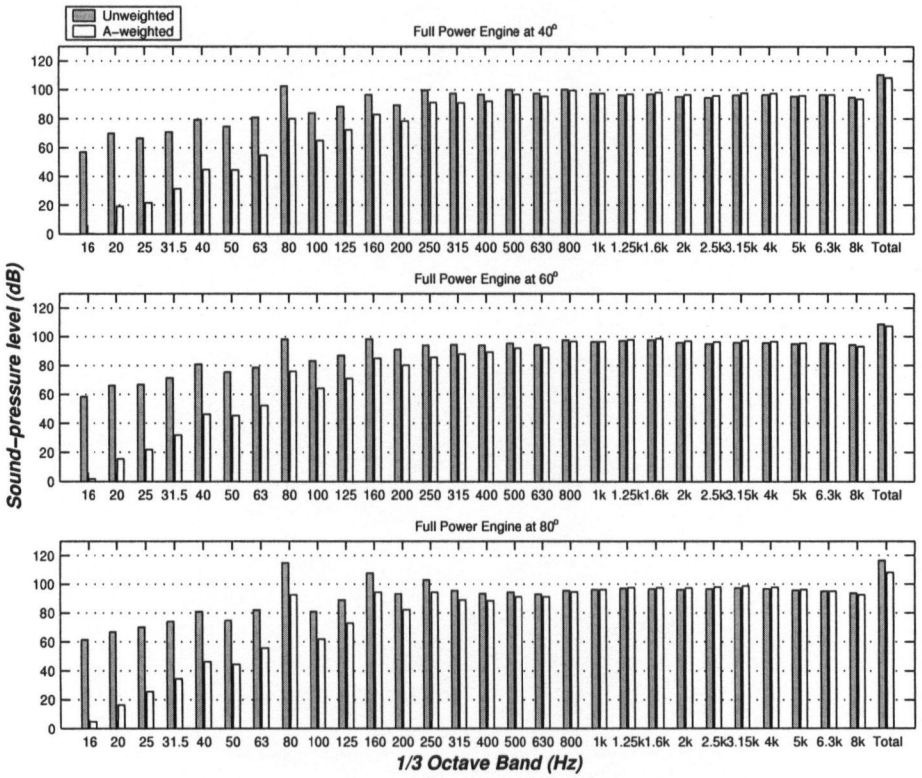

Figure B.8: 1/3 octave band spectra for both engines at full power at positions 40^0, 60^0 *and* 80^0.

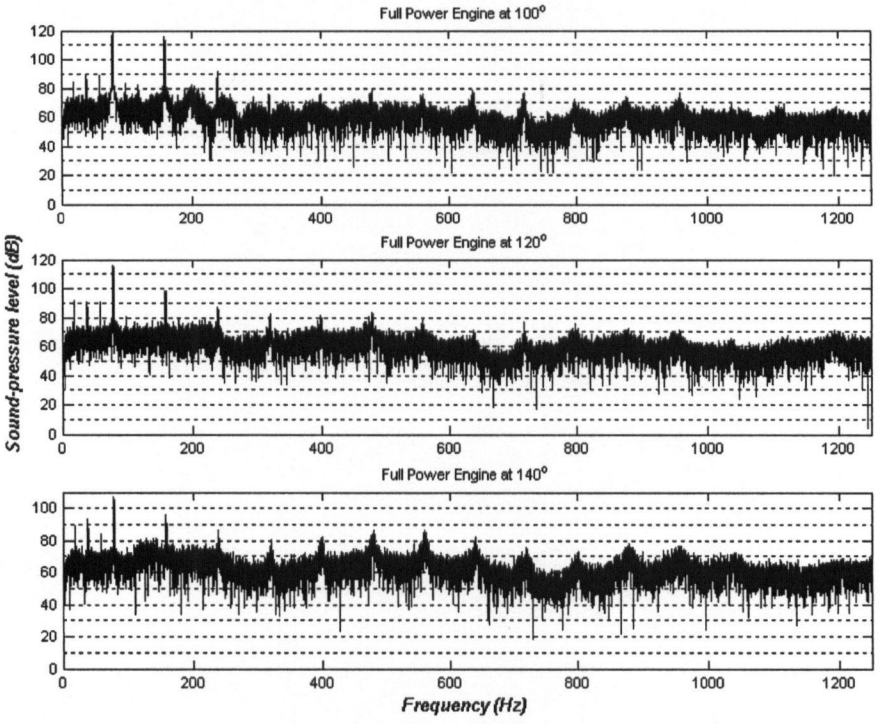

Figure B.9: Narrow band spectra for both engines at full power at positions 100^0, 120^0 *and* 140^0.

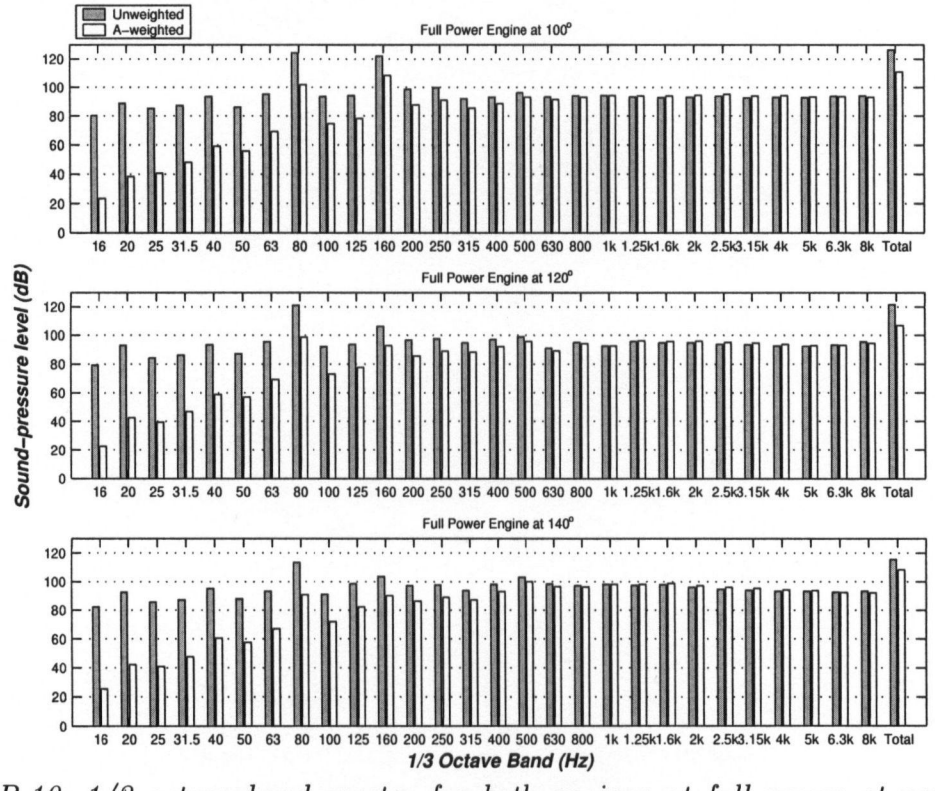

Figure B.10: 1/3 octave band spectra for both engines at full power at positions 100^0, 120^0 *and* 140^0.

Appendix C

Half Power and Single Engine Spectra

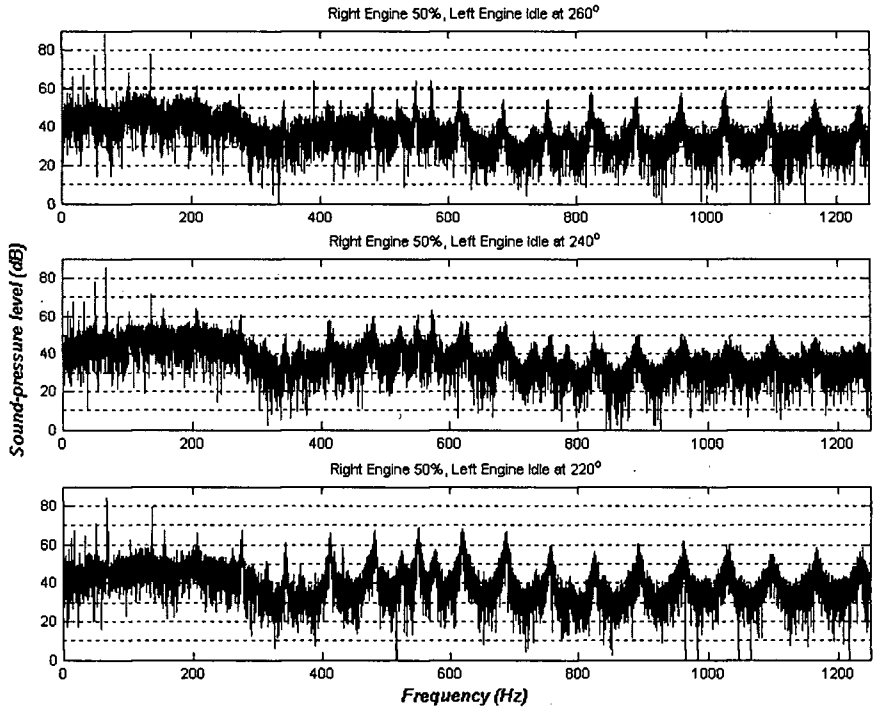

Figure C.1: Narrow band spectra for the right engine at 50% and the left engine idle at positions 220^0, 240^0 *and* 260^0.

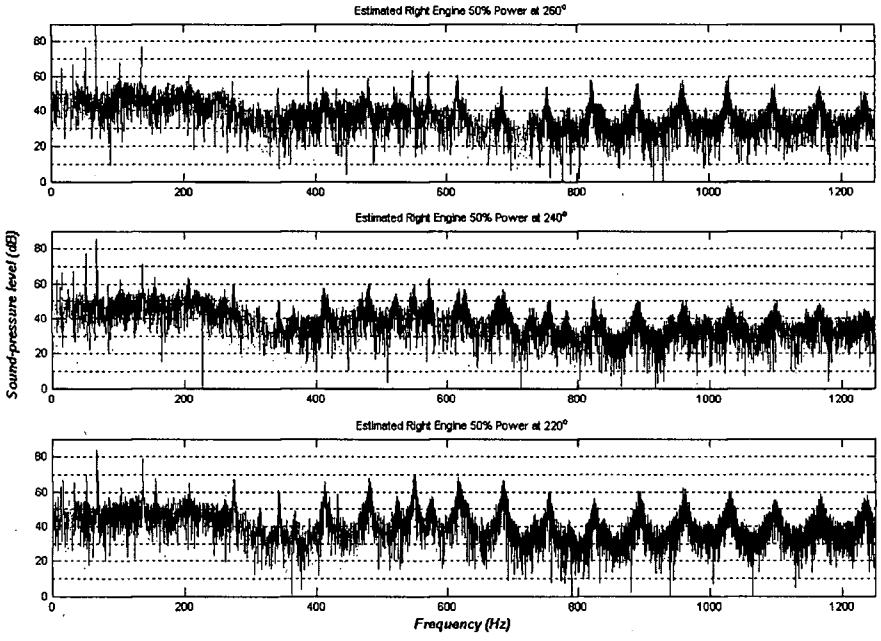

Figure C.2: Narrow band spectra for the right engine at 50% power at positions 220^0, 240^0 *and* 260^0.

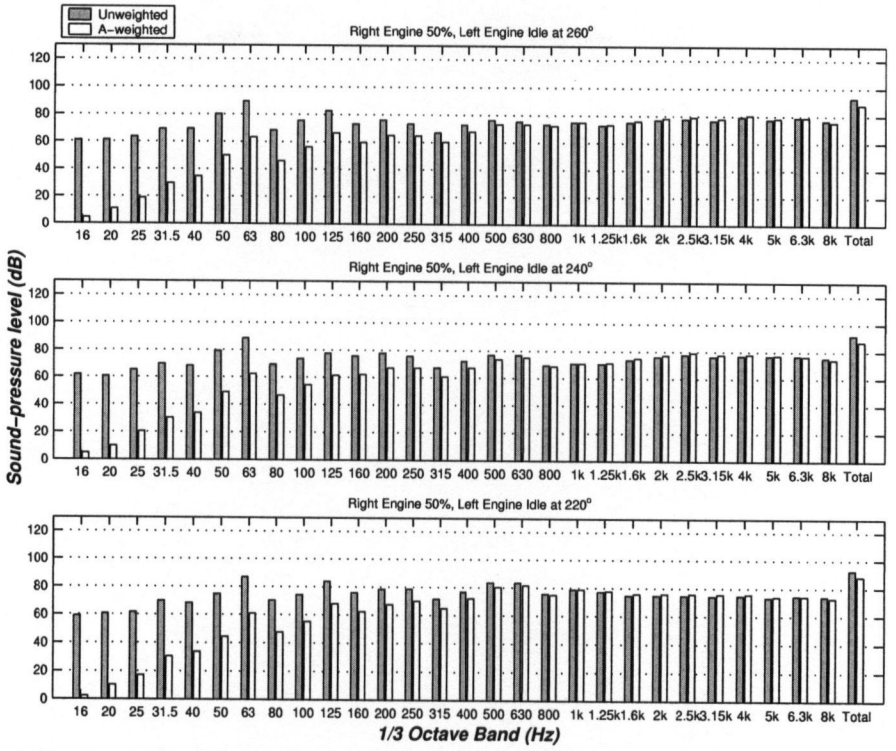

Figure C.3: 1/3 octave band spectra for the right engine at 50% and the left engine idle at positions 220^0, 240^0 *and* 260^0.

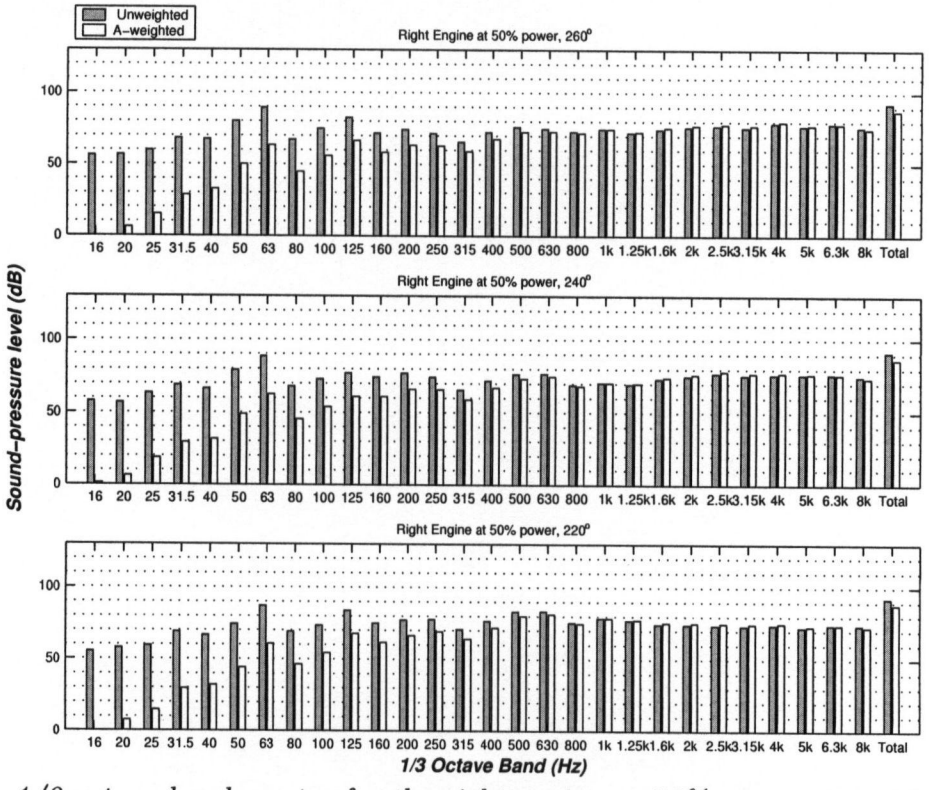

Figure C.4: 1/3 octave band spectra for the right engine at 50% power at positions 220^0, 240^0 *and* 260^0.

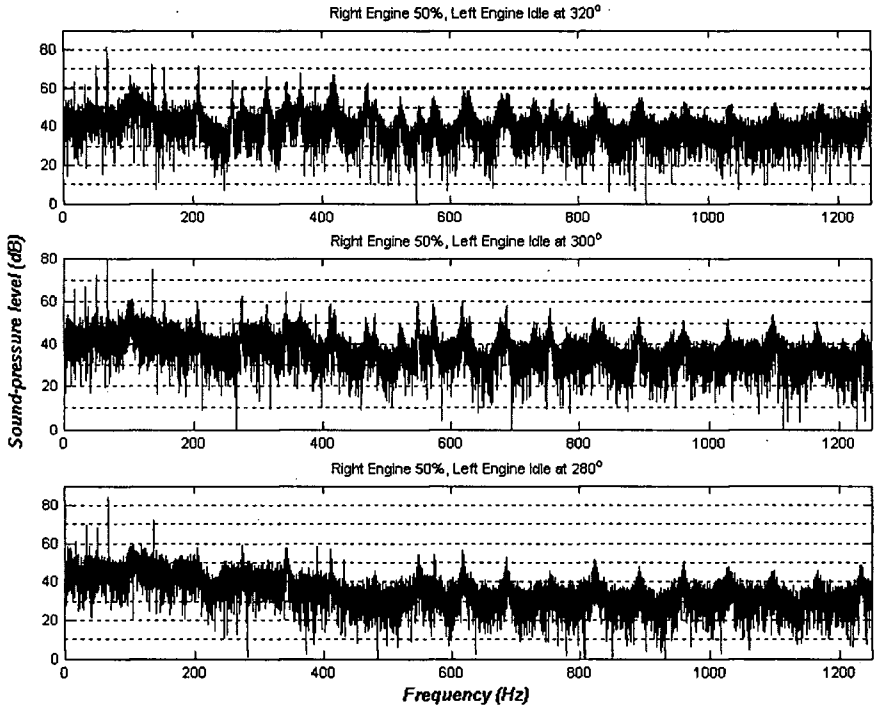

Figure C.5: Narrow band spectra for the right engine at 50% and the left engine idle at positions 280^0, 300^0 *and* 320^0.

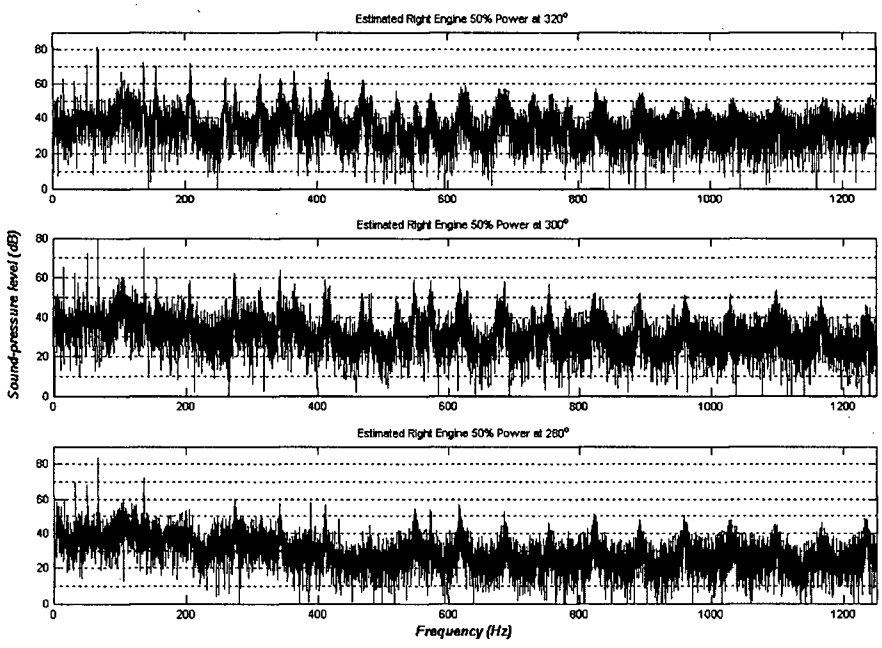

Figure C.6: Narrow band spectra for the right engine at 50% power at positions 280^0, 300^0 *and* 320^0.

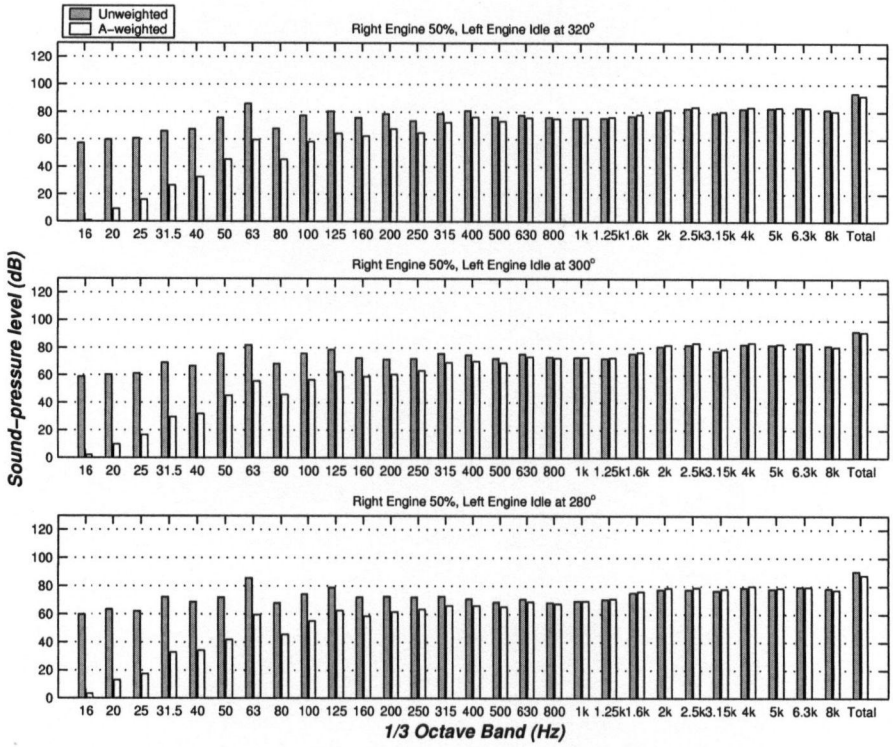

Figure C.7: 1/3 octave band spectra for the right engine at 50% and the left engine idle at positions 280^0, 300^0 *and* 320^0.

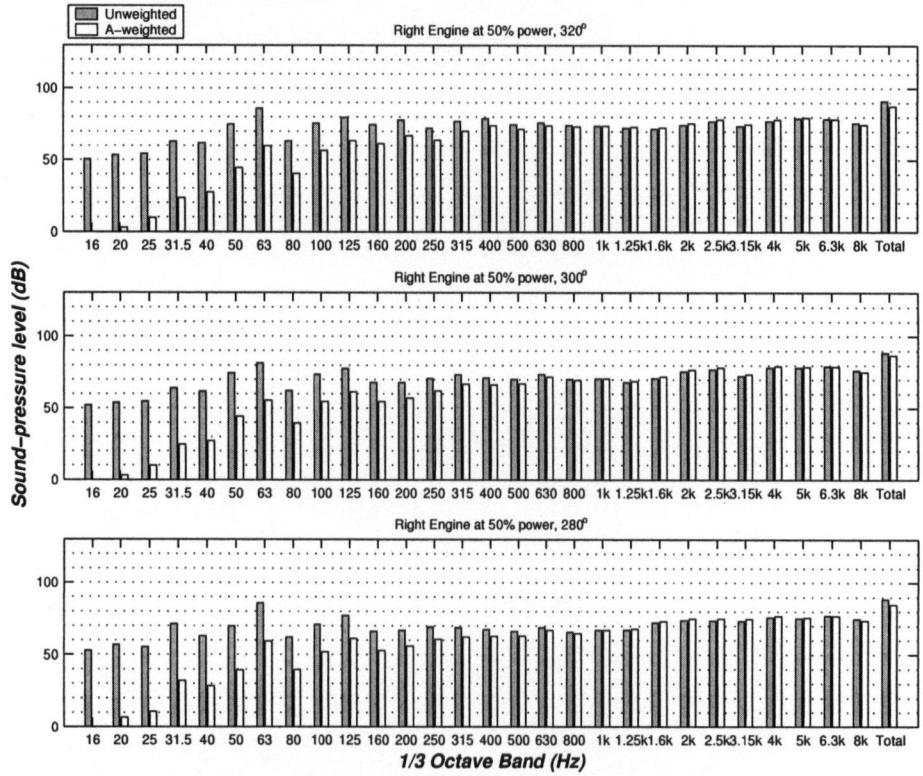

Figure C.8: 1/3 octave band spectra for the right engine at 50% power at positions 280^0, 300^0 *and* 320^0.

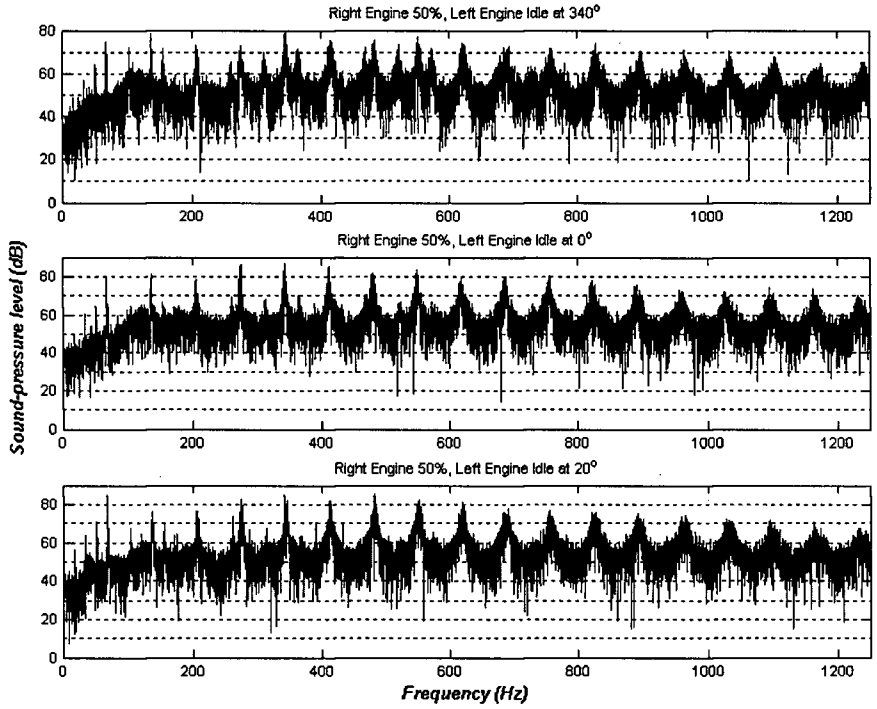

Figure C.9: Narrow band spectra for the right engine at 50% and the left engine idle at positions 340^0, 0^0 *and* 20^0.

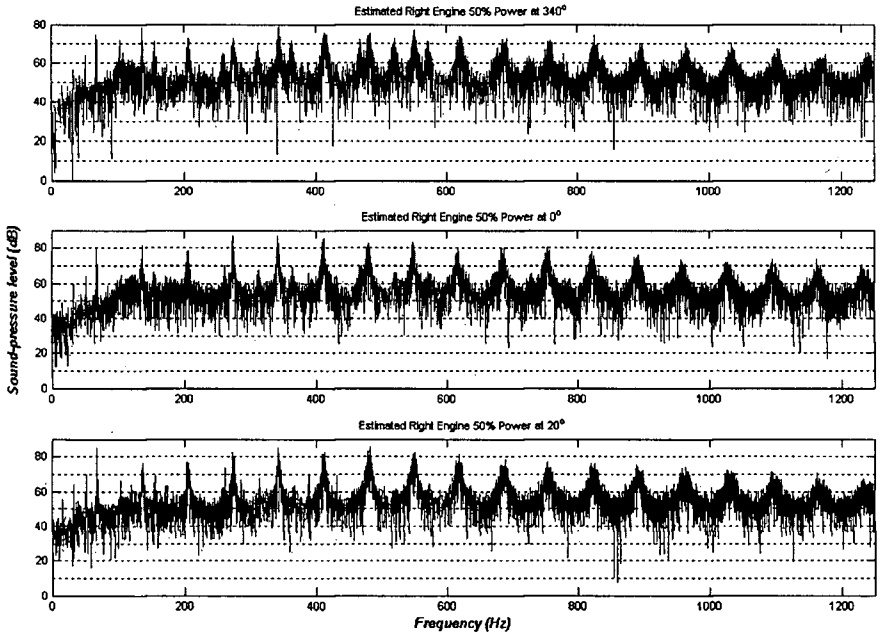

Figure C.10: Narrow band spectra for the right engine at 50% power at positions 340^0, 0^0 *and* 20^0.

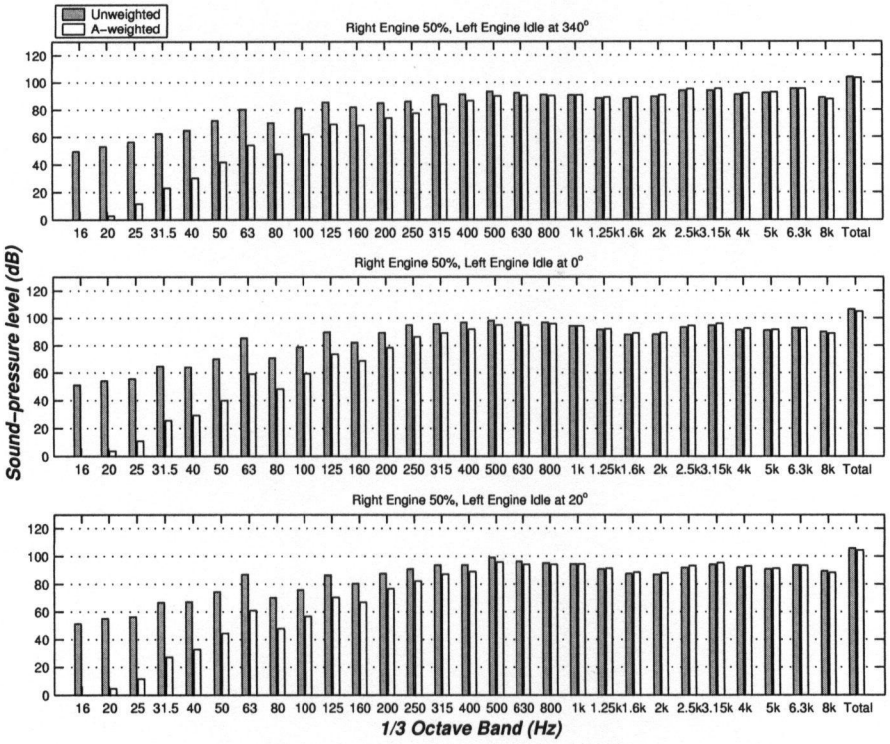

Figure C.11: 1/3 octave band spectra for the right engine at 50% and the left engine idle at positions 340^0, 0^0 *and* 20^0.

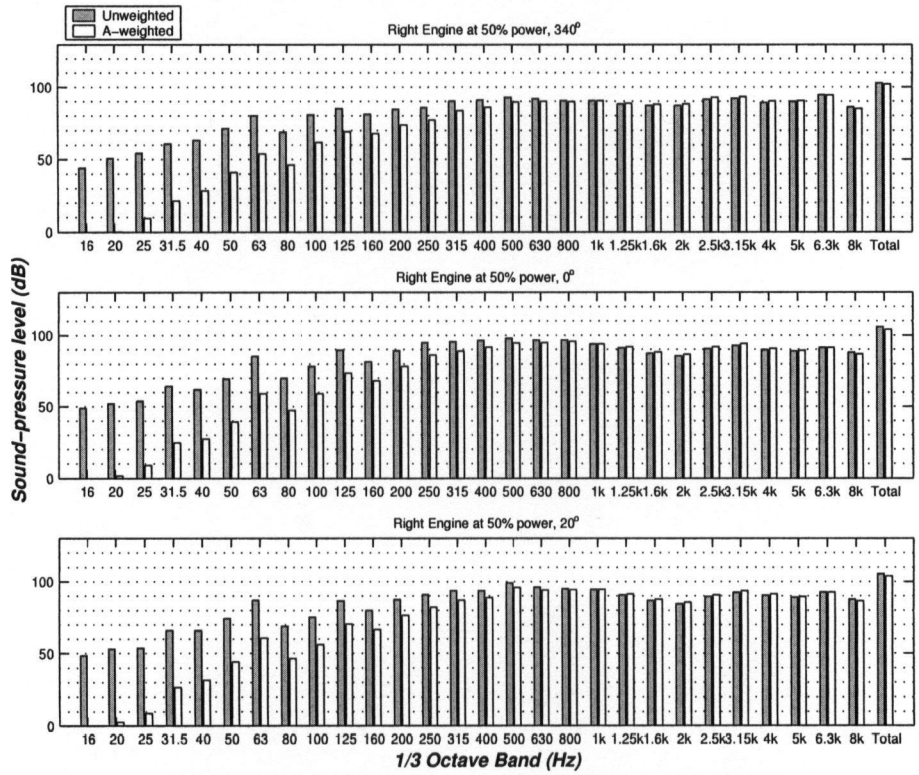

Figure C.12: 1/3 octave band spectra for the right engine at 50% power at positions 340^0, 0^0 *and* 20^0.

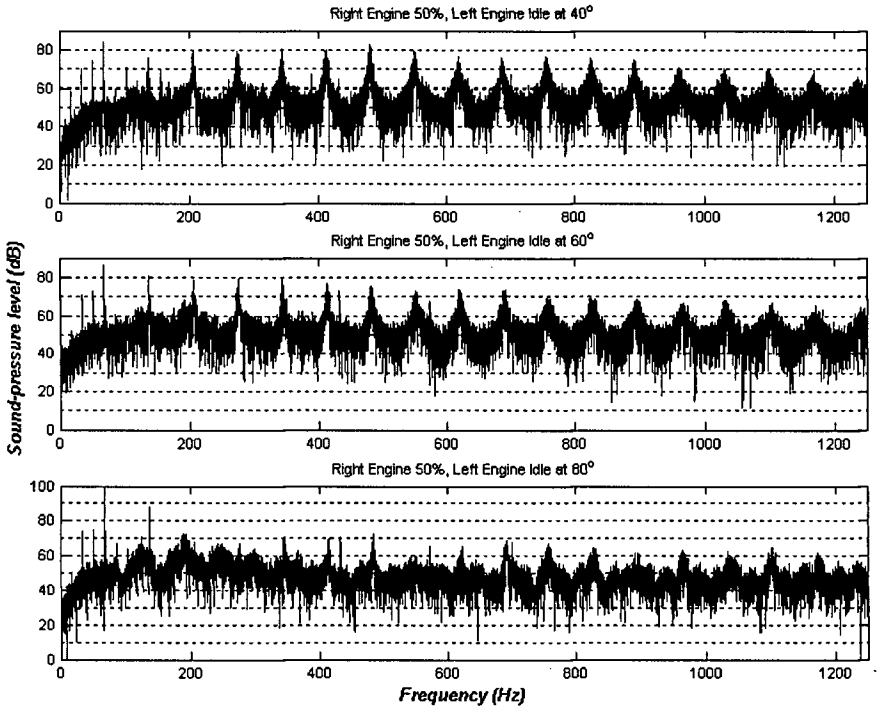

Figure C.13: Narrow band spectra for the right engine at 50% and the left engine idle at positions 40^0, 60^0 *and* 80^0.

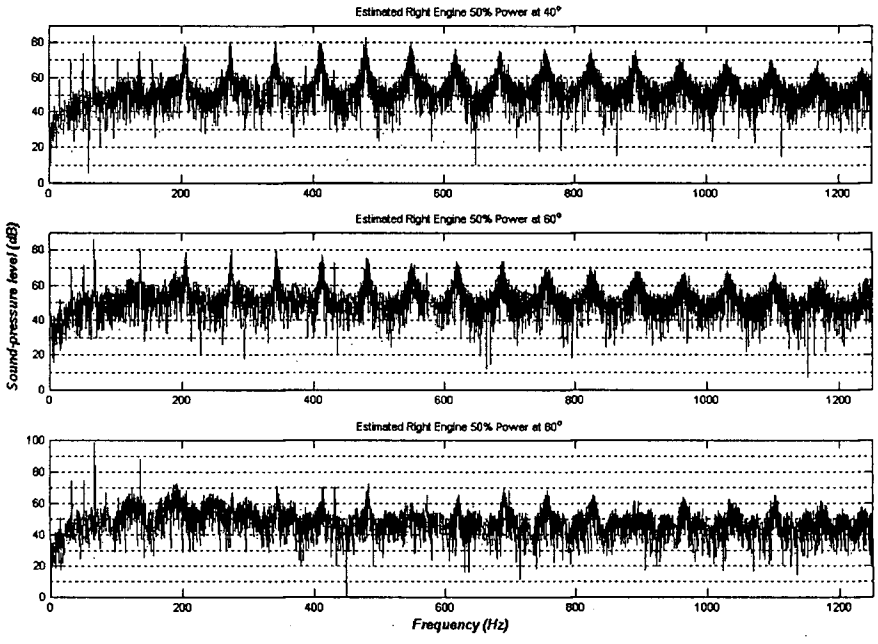

Figure C.14: Narrow band spectra for the right engine at 50% power at positions 40^0, 60^0 *and* 80^0.

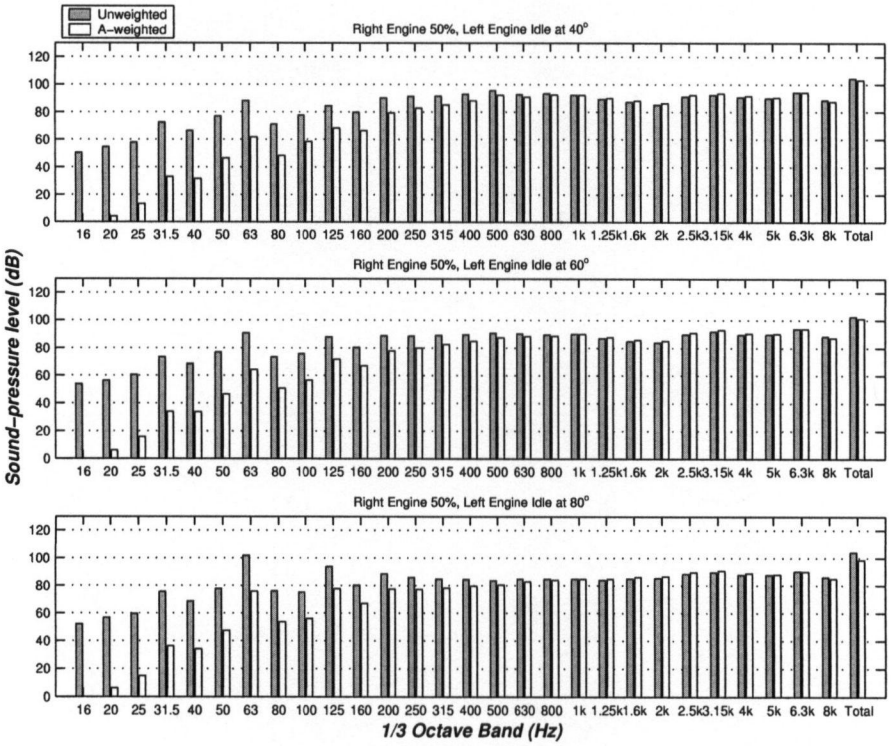

Figure C.15: 1/3 octave band spectra for the right engine at 50% and the left engine idle at positions 40^0, 60^0 *and* 80^0.

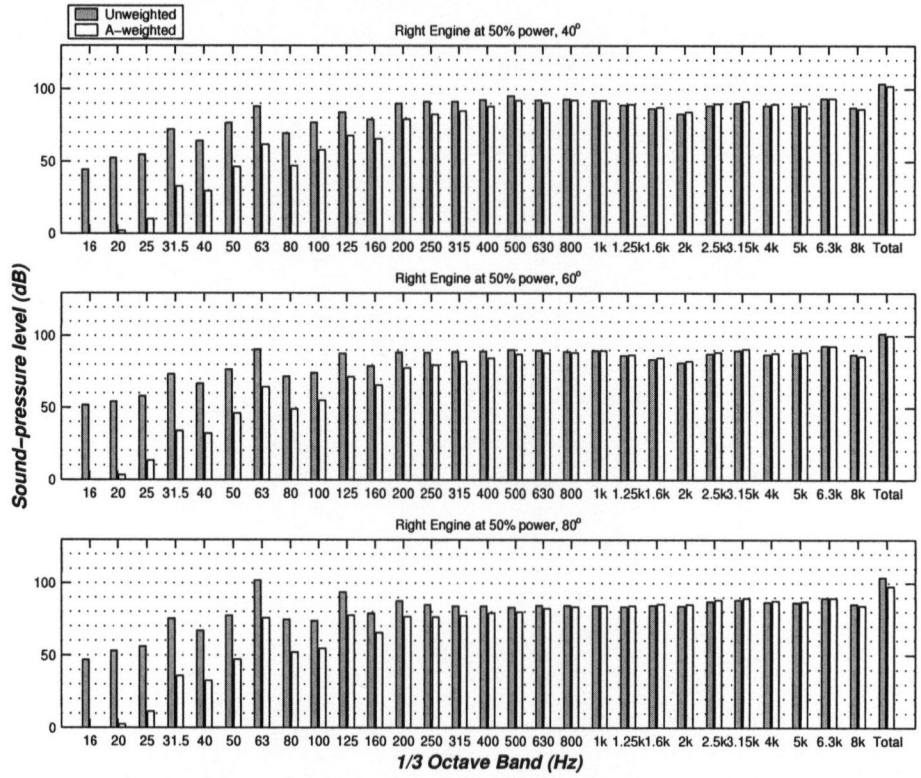

Figure C.16: 1/3 octave band spectra for the right engine at 50% power at positions 40^0, 60^0 *and* 80^0.

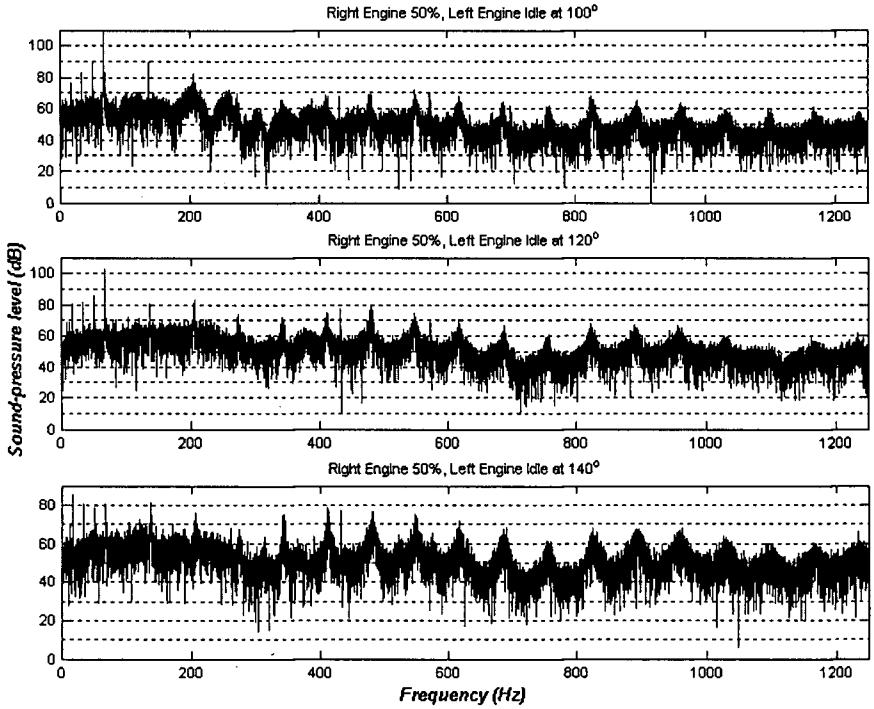

Figure C.17: Narrow band spectra for the right engine at 50% and the left engine idle at positions 100^0, 120^0 *and* 140^0.

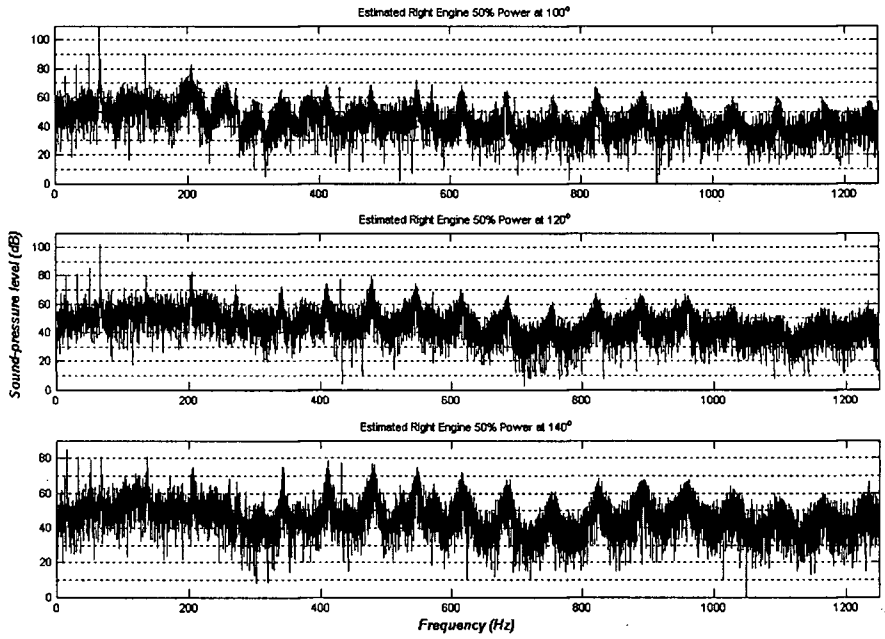

Figure C.18: Narrow band spectra for the right engine at 50% power at positions 100^0, 120^0 *and* 140^0.

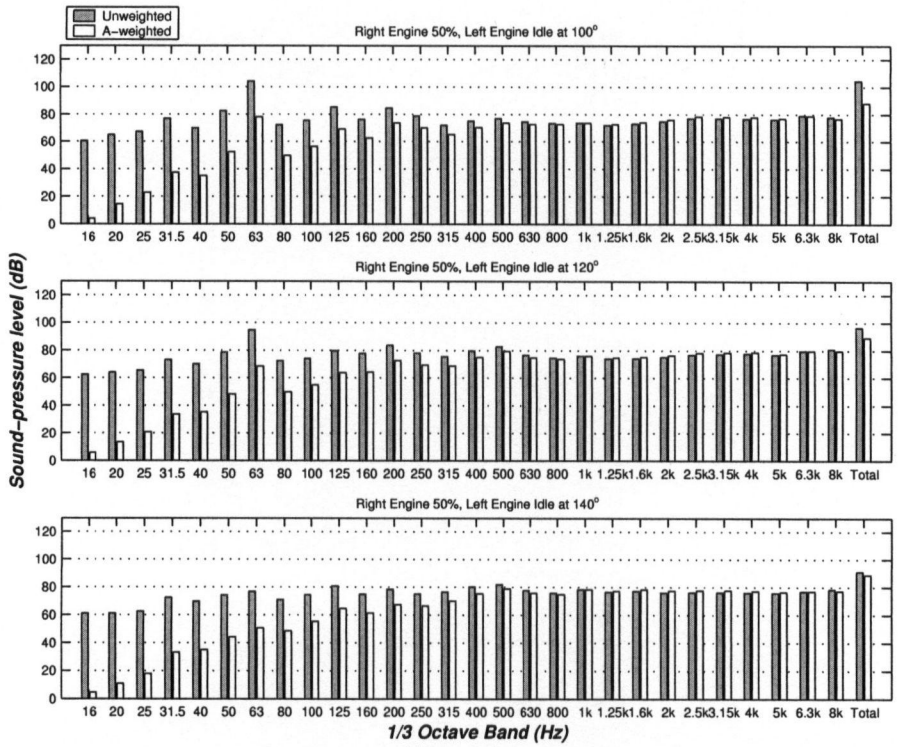

Figure C.19: 1/3 octave band spectra for the right engine at 50% and the left engine idle at positions 100^0, 120^0 *and* 140^0.

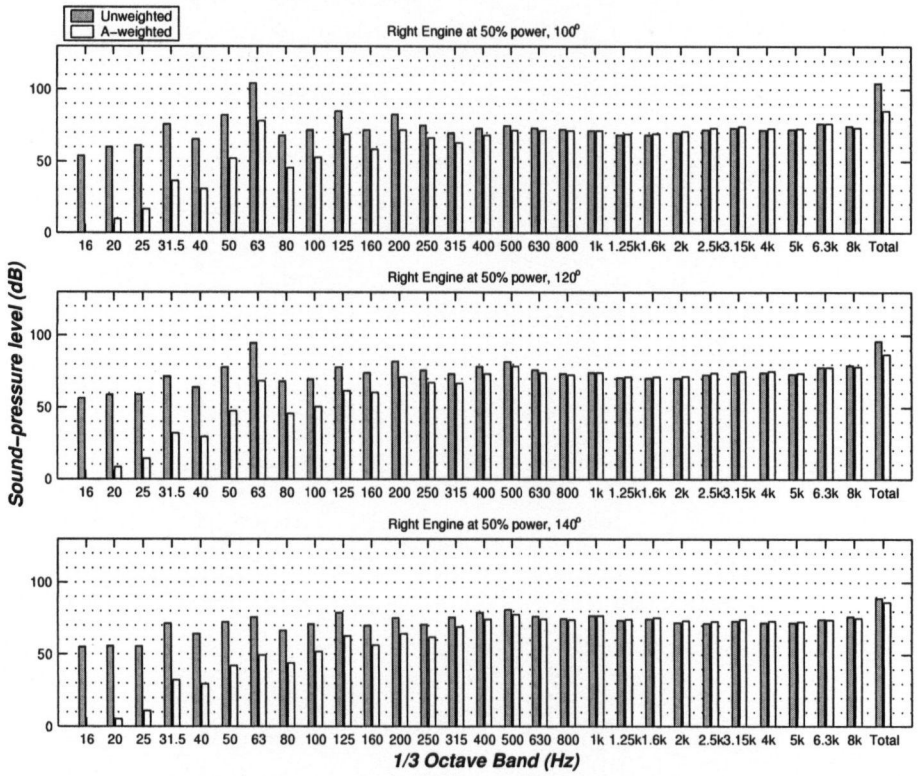

Figure C.20: 1/3 octave band spectra for the right engine at 50% power at positions 100^0, 120^0 *and* 140^0.